A REAL TIME PHASE SPACE BEAM SIZE AND DIVERGENCE MONITOR FOR SYNCHROTRON RADIATION

A Dissertation Submitted to

the College of Graduate and Postdoctoral Studies

in Partial Fulfillment of the Requirements

for the Degree of Doctor of Philosophy

in the

Department of Physics and Engineering Physics

University of Saskatchewan

By

Nazanin Samadi

Saskatoon, SK

Canada

PERMISSION TO USE

In presenting this thesis in partial fulfilment of the requirements for a Postgraduate degree from the University of Saskatchewan, I agree that the Libraries of this University may make it freely available for inspection. I further agree that permission for copying of this thesis in any manner, in whole or in part, for scholarly purposes may be granted by the professor or professors who supervised my thesis work or, in their absence, by the Head of the Department or the Dean of the College in which my thesis work was done. It is understood that any copying or publication or use of this thesis or parts thereof for financial gain shall not be allowed without my written permission. It is also understood that due recognition shall be given to me and to the University of Saskatchewan in any scholarly use which may be made of any material in my thesis.

Requests for permission to copy or to make other use of material in this thesis in whole or part should be addressed to:

Head of the Department of Physics and Engineering Physics
116 Science Place
University of Saskatchewan
Saskatoon, Saskatchewan S7N 5E2 Canada

Or

Dean
College of Graduate and Postdoctoral Studies
University of Saskatchewan
116 Thorvaldson Building, 110 Science Place
Saskatoon, Saskatchewan S7N 5C9 Canada

ABSTRACT

My prior work has shown that an electron beam position and angle monitoring system was able to measure the electron source position and angle at a single location in a beamline at a synchrotron source. This system, a phase space − Beam Position Monitor (ps-BPM), relies on a monochromator to prepare a photon beam whose energy is at that of K-edge of an absorber filter. The natural divergence of the photon beam from the source gives an energy range that will encompass the K-edge of the filter. A measurement of the center of the monochromatic beam and the K-edge location through the absorber filter gives the position and angle of the electron source with sensitivity comparable to any beam position measurement system.

Further, this thesis shows that this system is capable of measuring the source size and divergence at the same time by measuring the photon beam spatial distribution and the K-edge filtered beam distribution also with a sensitivity comparable to other existing methods for the source size; no other single measurement method is capable of divergence measurements. This was validated by measurements and simulations as the beam size in the storage ring was changed. The position measurements can be done in near real time and the size measurements can be done near 1 Hz.

The system was extensively modeled for its application at the CLS as well as possible implementations at other higher brightness sources such as the Advanced Photon Source Upgrade (APS-U). The modeled performance of the ps-BPM system was compared against other methods for measuring the electron source properties for high brightness sources. These methods included pinhole imaging and double-slit interferometry.

This system is being considered as a candidate system for the APS-U.

ACKNOWLEDGEMENTS

First and most of all, I would like to express my deepest gratitude to my supervisor, Prof. Dean Chapman for his continuous support during my studies and the writing this thesis. He inspired me with his knowledge, passion and smile and gave me freedom in my research. He made me fall in love with physics, and nature.   He not only guided me throughout my research, but also he taught me a better way to see the world and try to be a better person. I could not wish for a better and friendlier supervisor. Also, I want to thank Dean, Liz and their family for filling the absence of my own family here in Canada.

I would like to extent my deepest gratitude to Dr. Xianbo Shi for his invaluable knowledge, help and friendship working with him and learning from him was one of the greatest opportunities that I had.

I also would like to thank Dr. Les Dallin who never wavered in his support and was instrumental in my understanding of accelerator physics.

Special thanks to my advisory committee, Dr. Les Dallin, Dr. David Cooper, Dr. Rainer Dick and Dr. John Tse for their great ideas, knowledge and input into this work. It was a great pleasure to have them as my advisors and be able to use their guidance throughout my program.

Many thanks to Dr. George Belev for his valuable and unstoppable help and advice. I also like to thank Denise Miller and Adam Webb of the BMIT staff at the Canadian Light Source for their great guidance and help during my experiments and research.

Thanks should also go to Dr. Rob Lamb who always extended a great amount of assistance and advice.

Thanks go to my colleagues and friends in the x-ray imaging group. I would like to acknowledge the assistance of the accelerator division at the Canadian Light Source, specially Ward Wurtz and Bud Fogal.

I would like to extend my sincere thanks to the Advanced Photon Source accelerator division (Louis Emery and Vadim Sajaev) and optics group (Lahsen Assoufid and Al Macrander) for making my experiments at the Advanced Photon Source possible.

I also wish to acknowledge the financial support of Natural Sciences and Engineering Research Council of Canada (NSERC) Discovery Grant, Saskatchewan Innovation and Opportunities Scholarships, the government of Saskatchewan, the University of Saskatchewan, Department of Physics and Engineering physics at University of Saskatchewan, and Canada Research Chair Program. Research described in this thesis was performed at the Canadian Light Source, which is funded by the Canada Foundation for Innovation, NSERC, the National Research Council Canada, CIHR, the Government of Saskatchewan, Western Economic Diversification Canada, and the University of Saskatchewan.

I cannot begin to express my thanks to Arash for always being there and supporting me in every stage of my studies.

I finish with my amazing family, my parents and my sisters, for their unconditional support and motivation. I want to thank them for being patient with me. I’m grateful to have them.

To my beloved mom, dad and sisters

Ladan, Ahmad, Negin, Nasim and Naghmeh

And

To the bright memory of my loving grandparents

Azar joon and Baba jooni

TABLE OF CONTENTS

LIST OF TABLES

LIST OF FIGURES

ABBREVIATION

APS	Advanced Photon Source
APS-U	Advanced Photon Source Upgrade
BM	Bend Magnet
BMIT	Biomedical Imaging and Therapy
CCD	Charge Coupled Device
CIHR	Canadian Institutes of Health Research
CLS	Canadian Light Source
CRL	Compound Refractive Lens
DCM	Double Crystal Monochromator
eBPM	electron Beam Position Monitor
FBSF	Filament Beam Spread Function
FWHM	Full Width at Half Maximum
FZP	Fresnel Zone Plates
IDL	Interactive Data Language
IRF	Instrument Resolution Function
KB	Kirkpatrick-Baez
KEK	Kō Enerugī Kasokuki (The High Energy Accelerator Research Organization in Japan)
KES	K-Edge Subtraction
M.Sc.	Master of Science
MBA	Multi Bend Achromat

NSERC	National Sciences and Engineering Research Council of Canada
OASYS	ORange SYnchrotron Suite
OSR	Optical Synchrotron Radiation
PBPM	Photon Beam-Position Monitor
POE	Primary Optical Enclosure
ps-BPM	phase space – Beam Position Monitor
PSD	Power Spectral Density
PSF	Point Spread Function
RMS	Root Mean Square
SCM	Single Crystal Monochromator
sCMOS	scientific Complementary Metal–Oxide–Semiconductor
ShadowOui	Shadow3 Oasys User Interface
SNR	Signal-to-Noise Ratio
SRW	Synchrotron Radiation Workshop
UV	Ultraviolet
Vis	Visible
XOP	X-ray Oriented Programs
XSR	X-ray Synchrotron Radiation

CHAPTER 1

INTRODUCTION

1.1 INTRODUCTION

Sources of light have been used since the beginning of man to investigate and understand nature. Light sources have evolved dramatically and have become very tailored to their application. For research purposes a source that puts light into a specific direction with small divergence and with small source size will be able to put more photons onto a sample or provide extremely high spatial resolution at a given wavelenght.

In this thesis a new approach is presented to measure light source properties, specifically from a synchrotron source. These properties are source size, source divergence along with the source position and angle. Previous work by the author captured in an M.Sc. thesis and paper described a method to measure the electron beam position and angle [1]. This thesis and papers describe an extension of that method to measure the size and divergence of the source.

1.2 EMITTANCE

1.1.1 Photon source emittance

The property of divergence and size of the source is captured by the emittance [2]. Based on Liouville's Theorem the phase space of the source (product of the source rays' position and their momentum or trajectories) cannot be altered by an optical system that conserves the energy of the light [3, 4]. For example, an optical system that focuses the light from a source to a small spatial region will generate a large range of angles or trajectories at the focus. Conversely, an optical system creating a beam of light that is very parallel will result in a beam with relatively large spatial area. For a light source observed along a direction the longitudinal component of the momentum can be ignored and it is the transverse component (horizontal and vertical) that is of interest. This transverse component can be reduced to a measurement of the angles of the rays in the two transverse dimensions. Therefore, the emittance is defined by the product of the two transverse dimensions and divergences. At any point along the propagation of light in free space or through an optical system such as lenses or mirrors, the emittance will remain constant if no photons are lost or gained, or the energy of the photons remains changed.

From a classical viewpoint, light is generated by acceleration of charged particles. Electrons, being the least massive charged particles available, are pervasively responsible for almost all light. Sources of light involving acceleration of electrons are everywhere such as the sun, stars, lightning and fire. For research purposes sources that have small emittance are extremely useful as the light generated can be effectively manipulated to investigate samples. One of the most universally useful sources of light is that coming from a synchrotron source. It is the transverse (perpendicular to the direction of motion) acceleration of highly relativistic electrons that generates light that is also collimated by relativistic effects (small divergence). The size of the source is set by the size of the electron beam as it is being transversely accelerated. The angular divergence of the electron bunches also contributes to the divergence of the photon beam. As with light, the electrons themselves occupy a phase space as they longitudinally circulate through the magnetic structures that transversely bend and contain the electron beam. Thus, the photon emittance in a synchrotron is intimately coupled to the electron beam emittance.

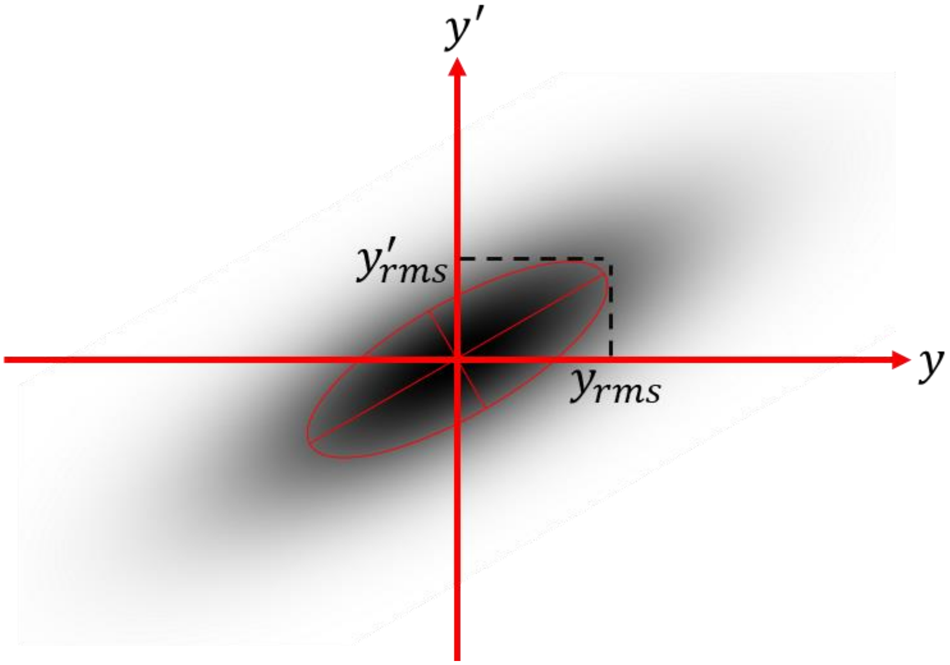

Figure 1- 1 Phase space ellipse of a Gaussian shape particle distribution. The density of particles is represented by the gray scale, black indicates increased particle density. y represents the particle location and y' represents the particle angle. The red ellipse shows the Gaussian width of the distribution ($e^{-1/2}$ points relative to the maximum). The area is π times ¼ the product of the major and minor axes of the ellipse shown in red. This area is conserved as the system evolves in time.

1.1.2 Electron beam emittance

The electron beam emittance can be described as the area/π of the phase space ellipse of particles in each transverse direction (if the motion is uncoupled) [2, 5]. Figure 1- 1 shows the particle density in gray scale (white is nothing; black is maximum particle density). The red ellipse in Figure 1- 1 identifies the one Gaussian widths points of the distribution (one σ). This ellipse (for a single particle) can be defined by four parameters ε, γ, β and α as shown by [5]

$$\varepsilon = \gamma y^2 + 2\alpha y y' + \beta y'^2, \tag{1. 1}$$

where ε is the emittance, y and y' are the position and angle of the particle and γ, β and α are the Twiss parameters. These parameters are not independent and are related by

$$\gamma = \frac{1+\alpha^2}{\beta}. \tag{1. 2}$$

The emittance in each of the transverse directions to the line between the source and observer has dimension of length×angle.

Since the physical dimensions of the beam (size and divergence) are varying by the location in the storage ring, emittance is widely used to describe the beam dimension as it doesn't change around the ring and its relationship to the source size and divergence is shown by,

$$\varepsilon_y = \frac{\sigma_y^2}{\beta_y} \text{ and} \tag{1. 3}$$

$$\varepsilon_y = \frac{\sigma'^2_y}{1+\alpha_y^2}\beta_y \ . \tag{1. 4}$$

where σ_y and σ_y' are source size and divergence.

The ability to measure the emittance of a synchrotron source is becoming increasingly important as there are world-wide efforts to make these sources brighter by reducing the emittance. One of the ways to reduce the emittance in a synchrotron storage ring is by implementing a multi-bend achromat (MBA) [6] lattice structure creating what is commonly called 4th generation synchrotron sources. The goal is to reduce the emittance to be as small as possible while preserving the stability of the beam to achieve high brightness.

A common way to indirectly measure the synchrotron source emittance is by measuring the source size at that location along with knowledge of the Twiss parameters for that location [7].

While there are projects under way at facilities to implement MBA lattices [8-10], there is a significant effort by diagnostic groups for measuring and monitoring the source size and stability.

1.3 DIFFERENT WAYS TO MEASURE THE SOURCE SIZE

Ability to measure the electron source size and divergence at synchrotron facilities is an important task as it defines the transverse emittance of the machine. Most, if not all, measurements of the electron source size and divergence are made by measurement of the emitted light from the source. Both insertion devices and bend magnet sources of light can be used for diagnostic beamlines, but, because of cost and limited number of insertion devices, most synchrotron facilities utilize bend magnet radiation for monitoring source properties.

The source size measurement methods can be categorized in two different groups: direct imaging methods and diffraction-based techniques. The typical required sensitivity for these measuring systems is about 5% of the source size. For the 4th generation sources the electron source size is in the range of 2-10 microns. Thus the sensitivity would need to be as low as 100 nanometer scale.

The direct imaging methods include pinhole imaging [11, 12] and systems using focusing optics like Compound Refractive Lenses (CRLs) [13], Fresnel Zone Plates (FZP) [14, 15] and Kirkpatrick-Baez (KB) mirrors [16].

The diffraction-based methods include double-slit [17-19], grating [20, 21] and multi-lens x-ray interferometry [22, 23] along with π polarization measurements with a diffraction obstacle [24, 25]. The diffraction-based methods rely on the transverse coherence of the source. These methods also require a higher intensity compared to direct imaging systems.

Pinhole imaging provides information in source size in both transverse directions and is the most common and simple way of measuring the source size at 3rd generation storage rings. This system is mostly used in white beam and doesn't require any complicated x-ray optics. However, because of diffraction and physical limitations, the ultimate resolution of the pinhole system is about 10 μm.

Measuring the source size with double-slit interferometry relies on the spatial coherence of the source which was first developed by Dr. Toshi Mitsuhashi at KEK in Japan. This system has high resolution and has been used to measure source sizes down to around 4 μm.

This system is mostly used in the visible light region. The quality of the optical components and their stability used in the visible light for this method is one of the limiting factors for the resolution of the system. Therefore, there are multiple proposals to implement the system in the x-ray regime to increase its sensitivity for ultra-low emittance machines [26].

1.4 THESIS SCOPE AND OVERVIEW

This thesis describes a method and system to simultaneously measure the electron source size and divergence along with its position and angle in the vertical plane at a single location from the source– a Phase Space – Beam Position Monitor (ps-BPM) for a synchrotron source. This system was developed at the Biomedical Imaging and Therapy Beamline (BMIT) [27, 28] at the Canadian Light Source (CLS). It uses the energy dispersive properties of x-ray diffraction from crystals and absorption K-edge of an element to pick a specific energy (angle) of the photon beam.

The following chapters include background information and papers that are published, accepted or submitted on specifications, application and characterization of the ps-BPM system.

Chapter 2 contains background information about synchrotron radiation, x-ray diffraction and absorption K-edge of elements. This information is needed to better understand the ps-BPM system.

Chapter 3 [29] describes in detail, a theory to extract absolute and relative electron source size and divergence from the data recorded by ps-BPM. The performance of the system and data was compared with the source size measured with a pinhole camera at the CLS X-ray Synchrotron Radiation (XSR) [30] diagnostic beamline. Simulations were done using ShadowOui [31] raytracing in the OASYS environment [32] to validate the performance of the system and the experimental results.

Chapter 4 has an overview of the ps-BPM as a source position, angle, size and divergence monitor. An application of the system during normal operations of the CLS storage ring is presented. Data in the time and frequency domain were used to characterize effects of machine and beamline optics and isolate them from each other. The effects of an insertion device magnetic field change on the electron source parameters was measured.

Chapter 5 includes an in-depth study to optimize the ps-BPM system using simulation tools. Each component and their effects on the resolution of the system was investigated. A feasibility study was performed to evaluate the performance of the system for the APS-U source size measurements.

Chapter 6 is a comparison between three possible ways to measure the source size for new generation storage rings with ultra-small emittance. The design consideration for pinhole imaging, double slit interferometry and ps-BPM are discussed along with their sensitivity and limitations for comparison.

Chapter 7 makes an overall conclusion about the body of work and describes possible future directions of research and development.

Appendix A is a copy of the paper that was published as part of earlier work for the author’s M.Sc. included here for reference [1]. This paper describes in detail how the ps-BPM was developed to measure the electron source position and angle at a single location.

Appendix B follows on the previous work done to measure the source position and angle with ps-BPM [33]. A noise with a fixed frequency was introduced in the ring and the beam position and angles were monitored with ps-BPM. The data was compared with theoretical values calculated for the noise. The source size was changed to demonstrate that the changes can be detected by ps-BPM system.

1.5 OBJECTIVES

The objective of this project was to determine the feasibility of a ps-BPM for measuring the source properties by:

1. Developing a complete theory of operation and modelling of system operation,
2. Determining the limits of the ability to extract the emittance information by measurements and modeling tools,
3. Applying it during normal operations of the CLS and observing changes in beam properties as an insertion device field was being altered,
4. Developing a modeled optimized implementation that could be used at APS-U,
5. Comparing the system with the other beam size monitoring systems.

1.6 REFRENCES

1. N. Samadi, B. Bassey, M. Martinson, G. Belev, L. Dallin, M. de Jong, et al., "A phase-space beam position monitor for synchrotron radiation," J Synchrotron Radiat, vol. 22, pp. 946-55, Jul 2015.
2. J. Buon, "Beam phase space and emittance," CAS - CERN Accelerator School : 5th General Accelerator Physics Course, France1992.
3. R. C. Tolman, The principles of statistical mechanics: Courier Corporation, 1979.
4. D. D. Nolte, "The tangled tale of phase space," Physics today, vol. 63, pp. 33-38, 2010.
5. K. Floettmann, "Some basic features of the beam emittance," Physical Review Special Topics-Accelerators and Beams, vol. 6, p. 034202, 2003.
6. D. Einfeld, M. Plesko, and J. Schaper, "First multi-bend achromat lattice consideration," Journal of Synchrotron Radiation, vol. 21, pp. 856-861, 2014.
7. G. Kube, "Review of synchrotron radiation based diagnostics for transverse profile measurements," in Proc. of DIPAC, 2007.

8. M. Eriksson, J. F. van der Veen, and C. Quitmann, "Diffraction-limited storage rings - a window to the science of tomorrow," Journal of Synchrotron Radiation, vol. 21, pp. 837-842, 2014.

9. P. F. Tavares, S. C. Leemann, M. Sjostrom, and A. Andersson, "The MAX IV storage ring project," Journal of Synchrotron Radiation, vol. 21, pp. 862-877, 2014.

10. M. Borland, M. Abliz, N. Arnold, T. Berenc, A. Blednykh, J. Byrd, et al., "The upgrade of the advanced photon source," in 9th Int. Particle Accelerator Conf.(IPAC'18), Vancouver, BC, Canada, April 29-May 4, 2018, 2018, pp. 2872-2877.

11. P. Elleaume, C. Fortgang, C. Penel, and E. Tarazona, "Measuring Beam Sizes and Ultra-Small Electron Emittances Using an X-ray Pinhole Camera," Journal of synchrotron radiation, vol. 2, pp. 209-214, 1995.

12. C. Thomas, G. Rehm, I. Martin, and R. Bartolini, "X-ray pinhole camera resolution and emittance measurement," Physical Review Special Topics - Accelerators and Beams, vol. 13, p. 022805, 02/24/ 2010.

13. T. Weitkamp, O. Chubar, M. Drakopoulos, I. Snigireva, A. Snigirev, C. Schroer, et al., "Electron Beam Size and Profile Measurements With Refractive X-Ray Lenses," in Proceedings of EPAC 2000, 2000, pp. 1824-1826.

14. K. Iida, N. Nakamura, H. Sakai, K. Shinoe, H. Takaki, M. Fujisawa, et al., "Measurement of an electron-beam size with a beam profile monitor using Fresnel zone plates," Nuclear Instruments and Methods in Physics Research Section A: Accelerators, Spectrometers, Detectors and Associated Equipment, vol. 506, pp. 41-49, 2003/06/21/ 2003.

15. S. Takano, M. Masaki, and H. Ohkuma, "X-ray imaging of a small electron beam in a low-emittance synchrotron light source," Nuclear Instruments and Methods in Physics Research Section A: Accelerators, Spectrometers, Detectors and Associated Equipment, vol. 556, pp. 357-370, 2006/01/01/ 2006.

16. T. Renner, H. Padmore, and R. Keller, "Design and performance of the ALS diagnostic beamline," Review of Scientific Instruments, vol. 67, pp. 3368-3368, 1996.

17. T. Naito and T. Mitsuhashi, "Very small beam-size measurement by a reflective synchrotron radiation interferometer," Physical Review Special Topics-Accelerators and Beams, vol. 9, p. 122802, 2006.

18. T. Mitsuhashi, Beam Measurement: Proceedings of the Joint US-CERN-Japan-Russia School on Particle Accelerators, Montreux, and CERN, Switzerland: World Scientific Publishing Company, 1999.

19. J. Corbett, X. Huang, C. Li, T. Mitsuhashi, J. Wu, Y. Xu, et al., "Transverse Beam Profiling and Vertical Emittance Control with a Double-Slit Stellar Interferometer," in 5th Int. Beam Instrumentation Conf.(IBIC'16), Barcelona, Spain, Sept. 13-18, 2016, 2017, pp. 237-240.

20. J. P. Guigay, S. Zabler, P. Cloetens, C. David, R. Mokso, and M. Schlenker, "The partial Talbot effect and its use in measuring the coherence of synchrotron X-rays," Journal of synchrotron radiation, vol. 11, pp. 476-482, 2004.

21. X. Shi, S. Marathe, M. J. Wojcik, N. G. Kujala, A. T. Macrander, and L. Assoufid, "Circular grating interferometer for mapping transverse coherence area of X-ray beams," Applied Physics Letters, vol. 105, p. 041116, 2014.

22. M. Lyubomirskiy, I. Snigireva, V. Kohn, S. Kuznetsov, V. Yunkin, G. Vaughan, et al., "30-Lens interferometer for high-energy X-rays," Journal of synchrotron radiation, vol. 23, pp. 1104-1109, 2016.

23. V. Kohn, I. Snigireva, and A. Snigirev, "Direct measurement of transverse coherence length of hard x rays from interference fringes," Physical review letters, vol. 85, p. 2745, 2000.

24. Å. Andersson, M. Böge, A. Lüdeke, V. Schlott, and A. Streun, "Determination of a small vertical electron beam profile and emittance at the Swiss Light Source," Nuclear Instruments and Methods in Physics Research Section A: Accelerators, Spectrometers, Detectors and Associated Equipment, vol. 591, pp. 437-446, 2008/07/01/ 2008.

25. J. Breunlin, Å. Andersson, N. Milas, Á. S. Hernández, and V. Schlott, "Methods for measuring sub-pm rad vertical emittance at the Swiss Light Source," Nuclear Instruments and Methods in Physics Research Section A: Accelerators, Spectrometers, Detectors and Associated Equipment, vol. 803, pp. 55-64, 2015.

26. T. Mitsuhashi and M. J. Boland, "Title," unpublished|.

27. T. W. Wysokinski, D. Chapman, G. Adams, M. Renier, P. Suortti, and W. Thomlinson, "Beamlines of the biomedical imaging and therapy facility at the Canadian Light Source-Part 2," in Journal of Physics: Conference Series, 2013, p. 072013.

28. T. W. Wysokinski, D. Chapman, G. Adams, M. Renier, P. Suortti, and W. Thomlinson, "Beamlines of the biomedical imaging and therapy facility at the Canadian light source—Part 1," Nuclear Instruments and Methods in Physics Research Section A: Accelerators, Spectrometers, Detectors and Associated Equipment, vol. 582, pp. 73-76, 11/11/ 2007.

29. N. Samadi, X. Shi, L. Dallin, and D. Chapman, "A real-time phase-space beam emittance monitoring system," J Synchrotron Radiat, vol. 26, pp. 1213-1219, Jul 1 2019.

30. J. C. Bergstrom and J. M. Vogt, "The X-ray diagnostic beamline at the Canadian Light Source," Nuclear Instruments and Methods in Physics Research Section A: Accelerators, Spectrometers, Detectors and Associated Equipment, vol. 587, pp. 441-457, 2008.

31. L. Rebuffi and M. Sanchez del Rio, "ShadowOui: a new visual environment for X-ray optics and synchrotron beamline simulations," Journal of Synchrotron Radiation, vol. 23, pp. 1357-1367, 2016.

32. L. Rebuffi and M. S. d. Rio, "OASYS (OrAnge SYnchrotron Suite): an open-source graphical environment for x-ray virtual experiments," in SPIE Optical Engineering + Applications, 2017, p. 9.

33. N. Samadi, D. Chapman, and L. Dallin, "A Vertical Phase Space Beam Position and Emittance Monitor for Synchrotron Radiation," in 7\textsuperscript {th} Int. Beam Instrumentation Conf.(IBIC'18), Shanghai, China, 09-13 September 2018, 2019, pp. 186-189.

CHAPTER 2

BACKGROUND

2.1 SYNCHROTRON RADIATION

When an electron is traveling close to the speed of light (relativistic electrons) and is transversely accelerated relative to its velocity it will create what is called synchrotron radiation. Synchrotron radiation is typically created in a laboratory however there are extraterrestrial sources like the Crab nebula were synchrotron radiation is created by relativistic electrons in a strong magnetic field from a pulsar [1]. Early research uses of synchrotron radiation were parasitic to high-energy physics electron beam facilities [2]. The electron energy loss due to the radiation was a nuisance for high energy physics however the intensity and directional aspects of the light proved to be powerful for photon-based research, so much so, that facilities were designed and built specifically to create synchrotron radiation.

At synchrotron radiation facilities a nearly circular path of highly relativistic electrons is created by magnetic fields as shown in Figure 2- 1. This magnetic field is produced by dipole bending magnets in a magnetic structure called the lattice.

The photons are produced as a result of changes in the direction of the velocity vector of the electron in the transverse direction in the circular motion. The direction that the velocity vector is pointing is the direction that the light is being emitted into a cone with an approximate $1/\gamma$ radian opening angle where γ is the ratio of the electron beam's energy (E_R) to its rest mass energy ($\gamma = \frac{E_R}{m_e c^2}$) [3]. The electron energy in storage ring sources are typically in GeV or multi GeV

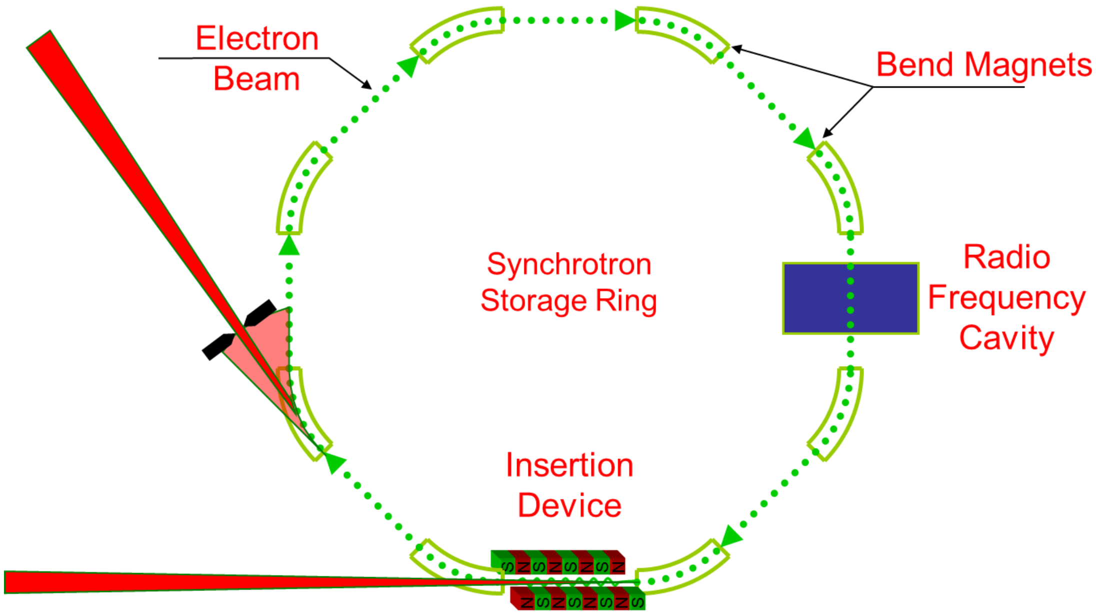

Figure 2- 1 Schematic of a synchrotron storage ring with an example bend magnet and insertion device beamline.

range, resulting in γ ranging from a few hundred to several thousands. For example, at the CLS storage ring γ is approximately 5700.

The creation of light depends on a transverse magnetic field and typically in a storage ring there is light from the bend magnets that creates the semi-circular trajectory and other devices that repeatedly transversely accelerate the electrons with a periodic magnetic field - wigglers and undulators. Though these devices provide very intense variable spectrum photon sources, further discussion about them is not provided here as it is available in great detail from other sources [4].

The spectrum from a bend magnet source is similar to an impact source such as an x-ray tube in that it generates a broad spectrum of light. The spectrum will extend from the far-infrared to the x-ray region depending on the electron energy and the strength of the magnetic field. A characteristic of the spectrum is the critical energy. There are different definitions of this photon energy, frequency, or wavelength, but the definition used here will be the point that marks the one-half radiated power point of the spectrum (i.e. one-half of the radiated power is below of this energy and one-half above). In practical units, it can be represented in *keV* energy units as,

$$E_c[keV] = 0.665\, E_R^2[GeV] B_0[T], \tag{2. 1}$$

where B_0 is the magnetic field in *T* (Tesla) of the dipole and E_R is the electron energy in *GeV* [3]. For a CLS bend magnet the critical energy is 7.57 keV (2.9 GeV ring energy, 1.354 T magnetic field).

The spectrum and angular distribution of synchrotron light from a bend magnet can be described as a function of photon energy (E_0), photon energy bandwidth ($\frac{\Delta E}{E}$), vertical opening angle (ψ) and horizontal angle (θ) by

$$\frac{d^2\dot{N}_0(E_0,\theta,\psi)}{d\theta d\psi}\left[\frac{ph}{s\ mr^2\ 0.1\%\frac{\Delta E}{E}}\right] = 1.327x10^{13} E_R^2[GeV] I_R[A] H\left(X,y\right), \tag{2. 2}$$

where E_R is the ring energy in GeV, I_R is the ring current in amperes,

$$H\left(X,y\right) = y^2\left(1+X^2\right)\left[K_{\frac{2}{3}}^2\left(\tfrac{1}{2}y\left(1+X^2\right)^{\frac{3}{2}}\right) + \frac{X^2}{1+X^2}K_{\frac{1}{3}}^2\left(\tfrac{1}{2}y\left(1+X^2\right)^{\frac{3}{2}}\right)\right], \tag{2. 3}$$

$X = \gamma\psi$ and $y = \dfrac{E_0}{E_c}$.

The $K_{\frac{1}{3}}$ and $K_{\frac{2}{3}}$ functions in Equation (2. 3) are modified Bessel functions of the 2nd kind of fractional order [3]. A plot showing the behavior of the Equation (2. 3) at $X=0$ as a function of

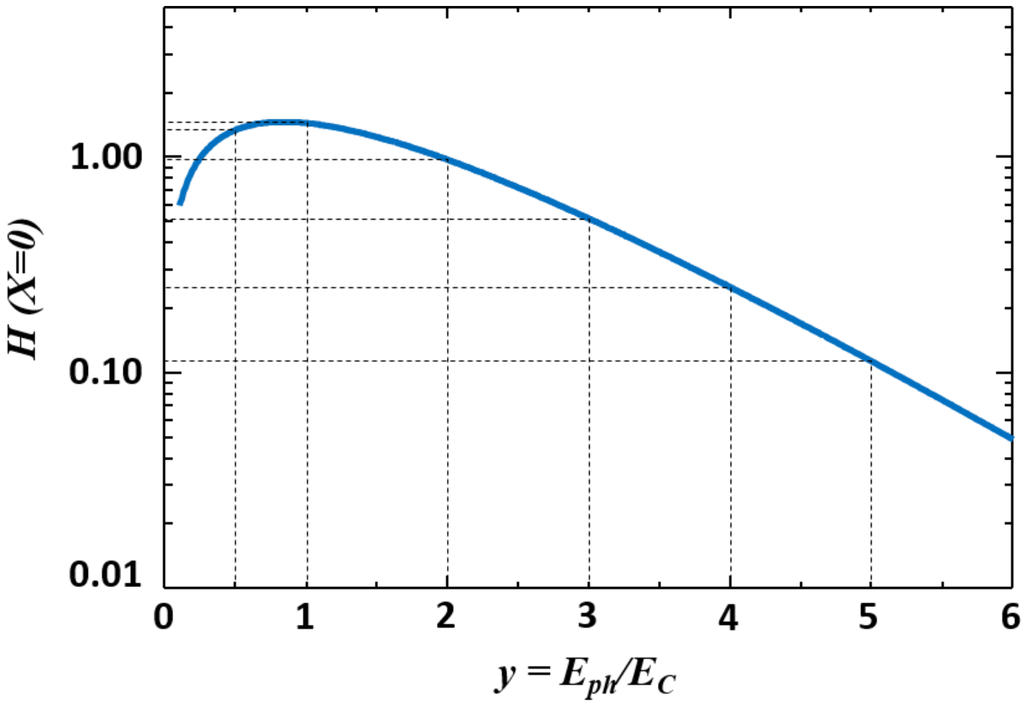

Figure 2- 2 Universal spectrum from a synchrotron bend magnet source. The plot represents the on axis ($\psi=X=0$) value of Equation (2. 3). The horizontal axis, y, is the photon energy normalized by the bend magnet critical energy. Plot was made using IDL.

y is shown in Figure 2- 2. This universal plot describes the energy spectrum from a bend magnet in terms of critical energy units.

At energies well above the critical energy of the source the synchrotron radiation can be well described by a Gaussian distribution. Figure 2- 3(b – g) shows the vertical distribution and the photon flux at various energies measured in critical energy units (y = 0.5, 1, 2, 3, 4, and 5) calculated using Equation (2. 3). The calculated profiles are shown in purple and Gaussian fits to those profiles are shown as red dashed lines. As can be seen that the fits are better for larger values of y. The percent standard error from the fitting routine written in IDL (Interactive Data Language, Harris Geospatial Solutions, Inc, Broomfield, Colorado, United States) is shown in Figure 2- 3a. As seen by looking at the profiles and the standard error profiles the Gaussian fit is near or below

1% when the photon energy is above the critical energy ($y \geq 2$). This ability to fit the shape of the synchrotron beam with a Gaussian profile is important for this project.

Synchrotron light from a bend magnet has primarily horizontal polarization (σ) due to the direction the electron is accelerated in by a bend magnet. Equation (2. 3) has two terms, the first term containing $K_{\frac{2}{3}}$ represents the fraction of the beam that is horizontally polarized (σ); the second term with $K_{\frac{1}{3}}$ the vertical (π) polarization. The horizontal polarization is complete when observed in the orbital plane ($X=\psi=0$). However, when observed above or below the vertical plane, the light picks up an elliptical polarization or vertical component (π).

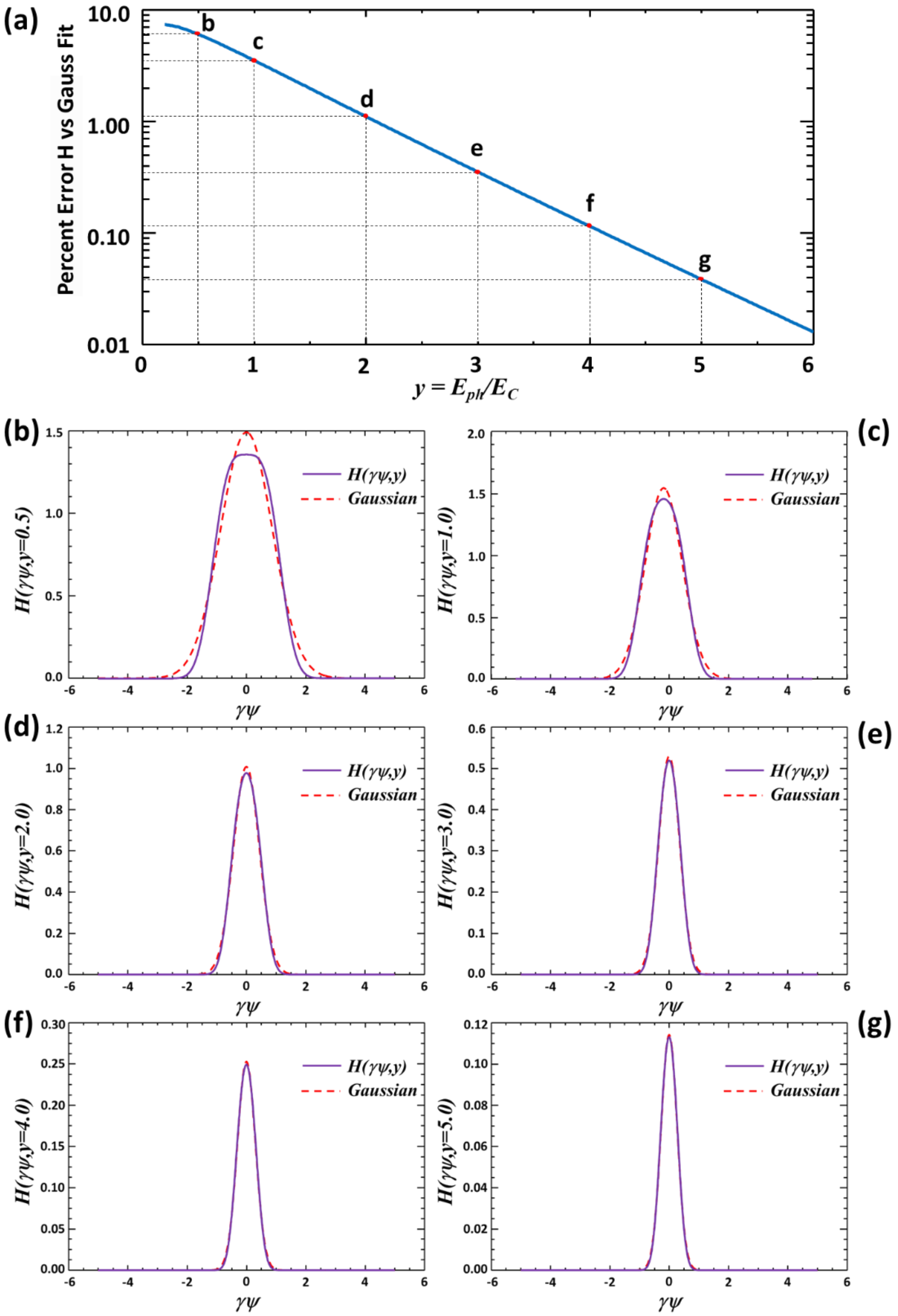

Figure 2- 3 Vertical beam profiles shown in purple calculated using Equation (2. 3) for values of y= 0.5 (Figure b), 1 (c), 2 (d), 3 (e), 4 (f) and 5 (g) over a ±5 γψ range. Gaussian fits to those profiles are shown in red dashed lines. The percent standard errors of those fits are shown in Figure a. (calculations and fits done in IDL).

2.2 X-RAY DIFFRACTION BY SINGLE CRYSTALS

2.2.1 Bragg’s law of diffraction

The synchrotron radiation beam is polychromatic, therefore, for many applications the selection of a specific energy (wavelength) is desired. In the x-ray range diffraction from crystals is commonly used to prepare these single energy or monochromatic beams. Single crystal silicon is the most common x-ray monochromator crystal use to select an energy.

The constructive interference between reflections from individual lattice planes in a crystal creates x-ray diffraction. The relationship between the wavelength of the incident beam, λ, the spacing between the lattice planes in the crystal, d_{hkl} and the angle between the lattice planes and incident beam, θ_B, can be described by Bragg’s law,

$$\lambda = 2d_{hkl} \sin\theta_B, \tag{2. 4}$$

where h, k and l are the Miller indices of the used reflection [5]. The derivative of Equation (2.4) gives

$$\frac{dE}{E} = \frac{d\lambda}{\lambda} = \frac{d\theta}{\tan\theta_B}. \tag{2. 5}$$

Most solids will have a poly-crystalline nature in which the material is composed of many small crystals that are mostly randomly oriented. Materials that are single crystals may also be composed of small crystallites that are mostly oriented. The angular distribution of those crystallites forms what is called the mosaic spread of the crystal. Diffraction properties of these types of crystals can be described by a single scattering theory (i.e. the x-ray will only diffract from a single crystallite). This single scattering type theory is called the kinematic theory of x-ray diffraction [5]. These types of poly-crystalline materials are not suitable for uses for high brightness sources as they destroy much of the coherence and collimation of a synchrotron beam. High quality single crystals such as silicon are available as a consequence of the semiconductor industries drive for better devices. These crystals are highly perfect, dislocation free and available in large sizes (greater than 30 cm diameter boules).

2.2.2 Perfect crystal diffraction

For crystals that are highly perfect a single scattering type theory is no longer appropriate and a wave theory that fully accounts for multiple interactions between the x-rays and the crystal lattice is needed. This type of fully interacting diffraction theory is called a dynamical theory [6, 7]. These perfect crystals used as a monochromator will preserve the phase, divergence and the wavefront properties of the source of light.

The reflectivity of the crystal is defined as the ratio between the intensity of the diffracted x-ray beam and that of a single energy incident plane wave beam.

Based on the dynamical theory, total reflection (reflectivity equals one) occurs within the Darwin width for a non-absorbing crystal with infinite layers of atomic planes. The angular Darwin width ω_D is given by [7],

$$\omega_D = \frac{4d_{hkl}^2 r_e |F|}{\pi V_c} \tan\theta_B, \tag{2. 6}$$

where r_e is the classic electron radius. F and V_C are the structure factor and volume of the crystal unit cell, respectively. This Darwin width can be transformed to energy bandwidth through Equation (2.5) and is

$$\frac{\Delta E}{E} = \frac{\omega_D}{tan\theta_B} = \frac{4d_{hkl}^2 r_e |F|}{\pi V_c}. \tag{2. 7}$$

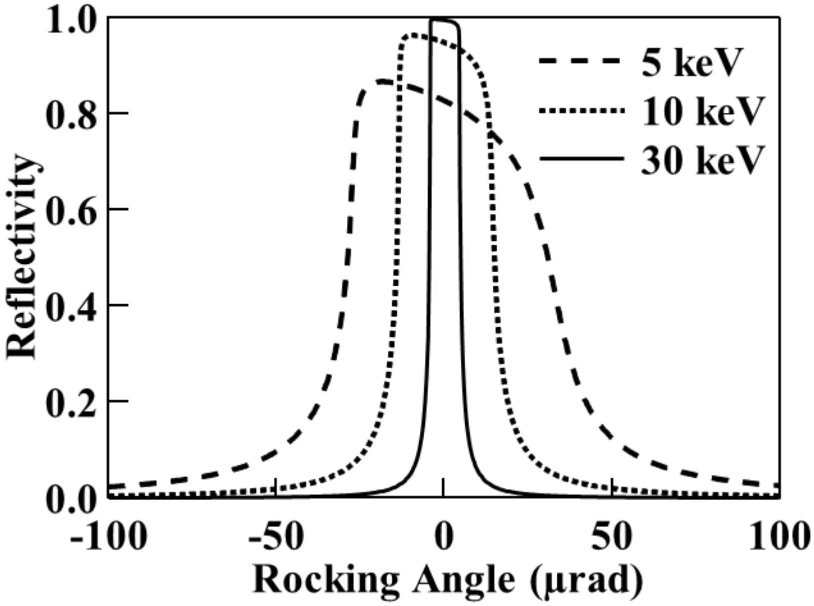

Figure 2- 4 Diffraction profiles of a Bragg Si (111) crystal at different energies calculated using the XCRYSTAL module in XOP.

An interesting aspect of this equation is that (ignoring minor absorption effects) the bandwidth from a perfect crystal is energy independent. For proper calculation of the reflectivity, the absorption effect needs to be included in the calculation of diffraction profiles as well. Figure 2- 4 shows examples of reflectivity curves of a Si (111) crystal tuned to different photon energies calculated using the XCRYSTAL [8] module in XOP [9].

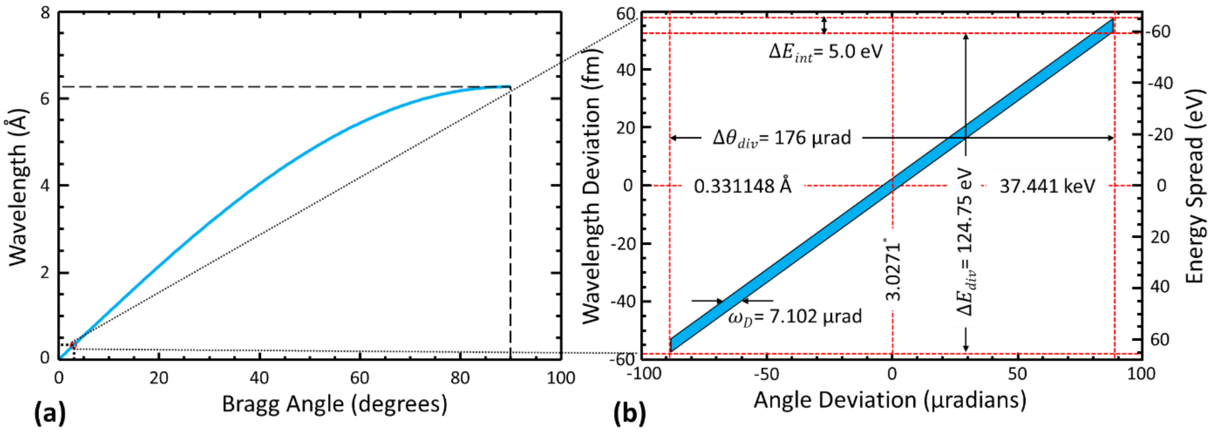

Figure 2- 5 DuMond diagram for the Si(1,1,1) reflection over the entire diffraction angle range (figure a) and Figure b shows an expanded view of the reflection at the Ba K-edge (37.441 keV) over an angular range that matches the vertical divergence f a bend magnet at the Canadian Light Source. Relevant parameters are given in Figure b. (calculations and plots are done using IDL)

2.2.3 Energy dispersion due to diffraction

When the incident beam is polychromatic and non-parallel, the crystal diffracts x-rays with different photon energies at different incident angles following Bragg's law (Equation (2.4)). A DuMond diagram [10] is normally used to describe the transfer function between the incident beam angle and the wavelength band. Figure 2- 5 shows an example DuMond diagram of a Si (1,1,1) crystal in the vicinity of the barium K-edge energy (37.441 keV) over the vertical opening angle of BM radiation.

The DuMond diagram shows the center, range, and width of beam divergence angle and the corresponding wavelength/energy, and their relationship through Equations (2. 4 - 2. 6). In the particular case in Figure 2- 5, the Si (1,1,1) crystal disperses the divergence range (176 µrad) of the vertical BM radiation fan into an energy spread of 125 eV. At each angular direction (a vertical cut in the DuMond diagram), the intrinsic energy bandwidth of the crystal is 5.00 eV.

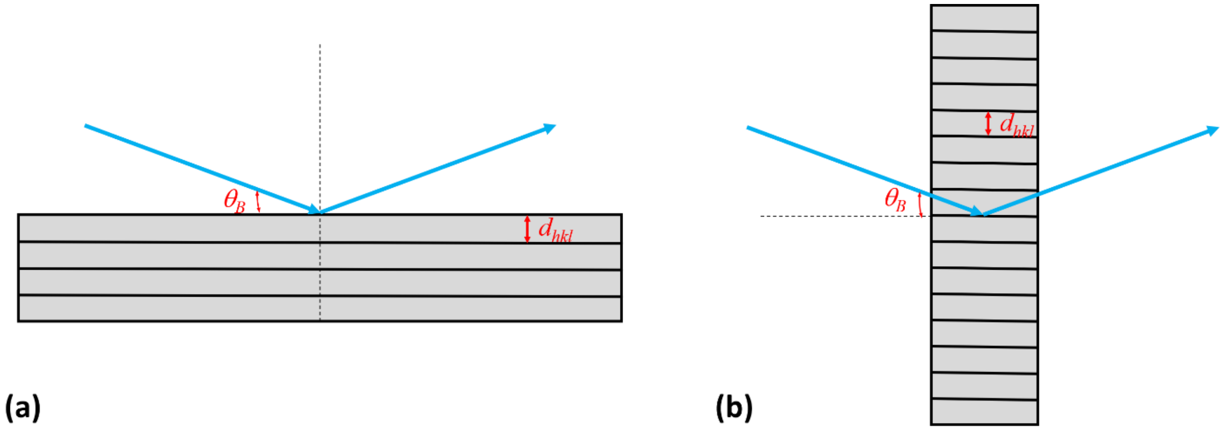

Figure 2- 6 Schematic of single crystal diffraction in the Bragg or reflection geometry (a) and the Laue or transmission geometry (b).

2.2.4 Crystal diffraction geometries

X-ray diffraction occurs from the interference of the x-rays with the lattice planes in a crystal. The relationship between the lattice planes and the crystal surface(s) defines the diffraction geometry which is divided into the reflection or Bragg geometry and transmission or Laue geometry. The Bragg geometry applies to the case when the incident x-ray beam and the diffracted beam from the planes enter and exit the same surface. The Laue geometry applies when the incident x-ray beam enters one surface and the diffracted beam exits a different surface. For monochromator applications the crystals are machined as plates and the lattice planes are usually parallel to the surface in Bragg case (symmetric Bragg) and perpendicular to the surface in the Laue case (symmetric Laue). Examples of each are shown in Figure 2- 6.

The energy of the monochromatized beam can be changed by changing the Bragg angle. This will move the diffracted beam in an angle. A double crystal geometry can be used to keep the beam at a fixed position where the first crystal is to monochromatize the beam and the second one to diffract that beam parallel to the incident polychromatic beam [11].

2.3 ABSORPTION K-EDGE OF AN ELEMENT

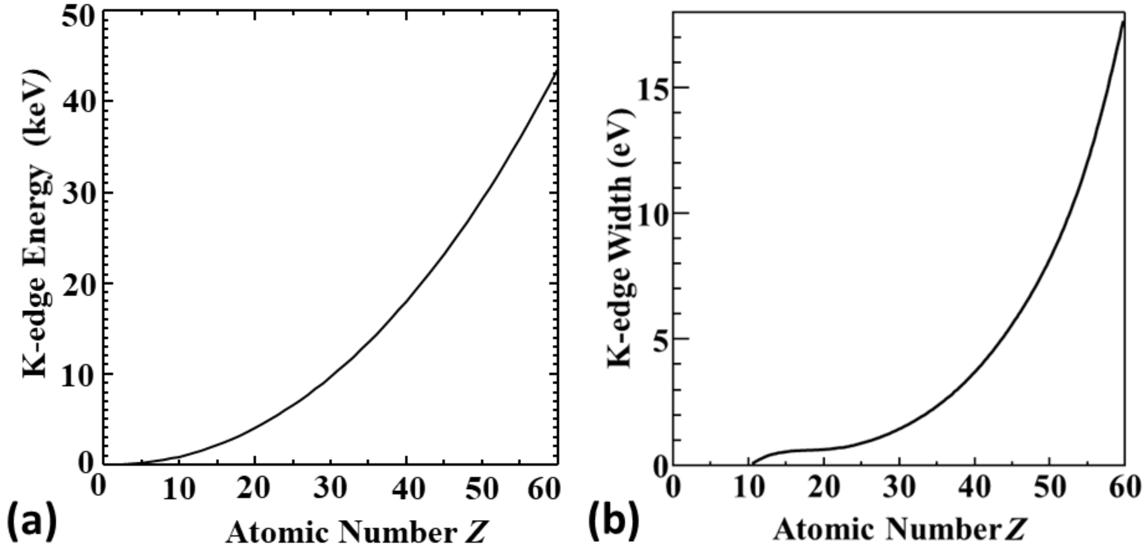

Figure 2- 7 K-edge energy (a) and K-edge width (b) for different elements as a function of their atomic number, *Z*.

X-rays interact with matter in a number of different ways much in the same way as visible light and matter interact. For example, x-rays experience refraction at interfaces between materials but is much reduced and is not relevant for the present discussion. Of interest here is the attenuation of x-rays as they traverse materials. In the energy range of from a few keV to a few hundred keV photon energy the primary interactions that attenuate x-rays are photoelectric absorption, Compton scattering and elastic scattering. All of these interactions play some role (good and bad) in the ps-BPM system. The photoelectric absorption is required for the operation of the ps-BPM, Compton scattering provides a background noise that interferes with the system and elastic scattering is the effect necessary for the operation of the monochromator.

The photoelectric absorption, of interest here, occurs when an x-ray photon interacts with an electron bound to an atom. When the photon energy exceeds the binding energy of the electron, the interaction results in the disappearance of the photon and the ejection of the electron from the atom with an energy that is the difference between the photon energy and the binding energy. This effect results in a contribution to the mass attenuation coefficient, μ/ρ, depending on the atomic number, Z, of the element and photon energy, E, having an approximate Z^3/E^3 relationship.

As the x-ray energies increase the x-ray photon can eject more and more bound electrons from the atom. When the x-rays have just enough energy to remove an electron from one of the shell levels of the atom the absorption will increase significantly. These jumps in absorption increase as deeper levels within the atom are accessed. In between these jumps in absorption the approximate $1/E^3$ relationship applies as a function of energy. When the photon energy is sufficient to eject the inner-most, tightly bound, electrons (1s or K-shell level) of an atom the absorption changes dramatically and is referred to as the K-edge of that element. The energies at which the K-edge occurs as a function of Z is shown in Figure 2- 7 (a).

The x-ray transmission through a material can be calculated using the Beer-Lambert law,

$$T = e^{-\frac{\mu}{\rho}\rho t}, \tag{2. 8}$$

where ρ is the density and t is the thickness of the material.

It is possible to tune the monochromator to the K-edge energy of an element. Due to the dispersion properties of the crystal and the range of angles from the source, some of the beam can be below the K-edge and some above the K-edge.

The K-edge of an element has a fixed energy width that depends on the lifetime of the electron hole created in the K-shell. Based on Heisenberg's uncertainty principle energy, ΔE, and time, Δt, are related by,

$$\Delta E \Delta t \gtrsim \hbar, \tag{2. 9}$$

where in the case of an excited stated, Δt is the lifetime, the time that it takes for that excited state to decay, ΔE is the minimum energy width and $\hbar$ is the Plank's constant [12].

Like the K-edge energy, this lifetime broadening also increases with Z of the element. Figure 2- 7(b) show K-edge width energy as a function of Z [13]. During this decay the transition of an upper shell electrons into the lower shell a photon may be emitted (fluorescence) whose energy matched the energy difference between the levels of the two shells, or less bound electrons may be ejected by a nonradiative process (Auger effect) or both can occur [14].

2.4 REFERENCES

1. W. contributors. (16 August 2019 20:07 UTC). Synchrotron radiation. Available: https://en.wikipedia.org/w/index.php?title=Synchrotron_radiation&oldid=911134449
2. A. L. Robinson, "History of synchrotron radiation," Synchrotron Radiation News, vol. 28, pp. 4-9, 2015.
3. K. J. Kim, "Characteristics of synchrotron radiation," AIP Conference Proceedings, vol. 184, pp. 565-632, 1989.
4. H. Onuki and P. Elleaume, Undulators, wigglers and their applications: CRC Press, 2003.
5. B. E. Warren, X-ray Diffraction: Courier Corporation, 1990.
6. W. H. Zachariasen, "A General Theory of X-Ray Diffraction in Crystals," Acta Crystallographica, vol. 23, pp. 558-+, 1967.
7. J. Als-Nielsen and D. McMorrow, Elements of Modern X-ray Physics: Wiley, 2011.
8. M. Sanchez del Rio, N. Perez-Bocanegra, X. Shi, V. Honkimäki, and L. Zhang, "Simulation of X-ray diffraction profiles for bent anisotropic crystals," Journal of Applied Crystallography, vol. 48, pp. 477-491, 2015.
9. M. S. del Río and R. J. Dejus, "XOP v2. 4: Recent developments of the x-ray optics software toolkit," in Advances in Computational Methods for X-Ray Optics II, 2011, p. 814115.
10. J. W. M. DuMond, "Theory of the Use of More Than Two Successive X-Ray Crystal Reflections to Obtain Increased Resolving Power," Physical Review, vol. 52, pp. 872-883, 10/15/ 1937.
11. J. A. Golovchenko, R. A. Levesque, and P. L. Cowan, "X-ray monochromator system for use with synchrotron radiation sources," Review of Scientific Instruments, vol. 52, pp. 509-16, 04/ 1981.
12. W. contributors. (17 August 2019 17:21 UTC). Spectral line shape. Available: https://en.wikipedia.org/w/index.php?title=Spectral_line_shape&oldid=909274648

13. Y. A. Babanov, A. V. Ryazhkin, A. F. Sidorenko, and L. A. Blaginina, "Correcting an experimental absorption spectrum for the core level width," Journal of Structural Chemistry, vol. 39, pp. 833-838, November 01 1998.

14. M. O. Krause and J. Oliver, "Natural widths of atomic K and L levels, K α X-ray lines and several KLL Auger lines," Journal of Physical and Chemical Reference Data, vol. 8, pp. 329-338, 1979.

CHAPTER 3

This paper was accepted in April 2019 and published July 2019 in the Journal of Synchrotron Radiation (Samadi, N., et al., A real time phase-space beam emittance monitoring system, J. Synch. Rad. (2019). 26, 1213-1219, https://doi.org/10.1107/S1600577519005423).

The author took all of the data and did all of the data analysis. The author arranged for the beamtime and coordinated data acquisition with the beam size studies. Others were involved in data analysis and simulations (Shi), storage ring properties (Dallin) and algorithm development (Chapman). The author, Dr. Shi and Prof. Chapman prepared the manuscript draft which was reviewed by Dr Dallin.

A REAL TIME PHASE-SPACE BEAM EMITTANCE MONITORING SYSTEM

Nazanin Samadi[a]*, Xianbo Shi[b], Les Dallin[c], Dean Chapman[c]
[a]Physics and Engineering physics, University of Saskatchewan, 116 Science Place, Saskatoon, SK, S7N 5E2 Canada
[b]Advanced Photon Source, Argonne National Laboratory, 9700 S. Cass Ave., Lemont, Illinois, 60439, USA
[c]Canadian Light Source, 44 Innovation Boulevard, Saskatoon, SK, S7N 2V3, Canada
Correspondence email: nazanin.samadi@usask.ca

Keywords: beam emittance monitor; x-ray diffraction; phase space; diagnostics and feedback

Synopsis An electron beam position and angle monitoring system, ps-BPM, has been shown to be able to measure the electron source position and angle at a single location in a beamline at a synchrotron source. This system is now shown to be capable of measuring the source size and divergence simultaneously

3.1 ABSTRACT

An electron beam position and angle monitoring system, ps-BPM, has been shown to be able to measure the electron source position and angle at a single location in a beamline at a synchrotron source. This system uses a monochromator to prepare a photon beam whose energy is at that of K-edge of an absorber filter. The divergence of the beam from the source gives an energy range that will encompass the K-edge of the filter. A measurement of the center of the monochromatic beam and the K-edge location through the absorber filter gives the position and angle of the electron source. This paper shows that this system is also capable of measuring the source size and divergence at the same time. This capability is validated by measurement as the beam size in the storage ring was changed and by ray-tracing simulations. The system operates by measuring the photon beam spatial distribution as well as a K-edge filtered beam distribution. These additional measurements result in the ability to also determine the electron source size and divergence.

3.2 INTRODUCTION

The emittance of the electron beam is a fundamental property of synchrotron sources as it describes the area of the transverse phase space of the electron source (product of the size and divergence) [1]. Measuring the electron source size and divergence is important and becoming ever more critical as the next generation light sources are being planned and built [2, 3], such as implementing a multi-bend achromat (MBA) lattice [4]. These new machines are focusing on achieving the smallest possible emittance ideally below the emittance of the photon radiation to deliver a diffraction-limited beam. For example, at the Advanced Photon Source (APS) the upgrade source emittance will be reduced from 3.1 nm·rad to 42 pm·rad [5]. The source size and divergence of these new machines are typically in the range of a few microns and microradians. The increased stability requirement for these new sources demands real-time monitoring of the source position, angle, size, and divergence to characterize and correct the source. There are different ways of measuring source size, which can be categorized as direct imaging and diffraction-based techniques.

Direct imaging systems include pinhole measurements [6, 7] and techniques using focusing optics like Compound Refractive Lenses (CRLs) [8], Fresnel Zone Plates (FZP) [9, 10], Kirkpatrick-Baez (KB) mirrors [11].

The traditional pinhole measurement is the most common technique used at the existing 3rd generation synchrotron facilities to give real-time information of the electron beam size in both transverse directions. The pinhole technique is simple and requires no focusing optics. However, it has a limited resolution (~10 μm), which makes it impractical for new high-brightness sources.

The diffraction-based methods utilize the spatial coherence of the source. To be able to analyze the contrast of the interferogram for these measurements requires high intensity compared to direct imaging systems. Available methods primarily rely on interferometry such as, double-slit [12-14], grating [15, 16] and multi-lens x-ray interferometry [17, 18]. Another recent interferometry method is based on π polarization measurements [19].

Most of the existing ways of measuring the emittance are only capable of measuring the size of the electron source with no information about the divergence except for a pinhole array system [20] which is limited in resolution.

The ps-BPM system was introduced previously [21], where the electron beam angle and position were measured simultaneously at a single location in a synchrotron beamline. In this paper, we will describe how that system can also be used to extract information about the electron beam source size and divergence and thus, the potential for a powerful real-time diagnostic tool.

3.3 PS-BPM SYSTEM

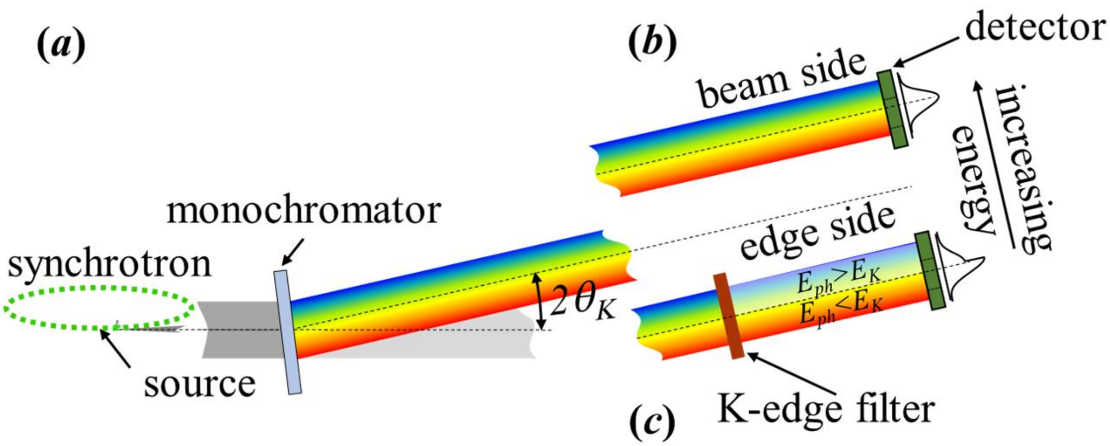

Figure 3- 1 Schematic of the ps-BPM system. (a) Side view of the source and monochromator (single Laue). Horizontally separated (b) unfiltered beam side and (c) filtered edge side of the photon beam on the same detector. Example intensity profiles on the right side of the figure in (b) shows the unfiltered photon distribution, and in (c) shows the intensity change in the vertical plane after the filter with the K-edge energy in the middle of the beam.

A schematic view of the ps-BPM system is shown in Figure 3- 1. Figure 3- 1a shows the source and monochromator. The monochromator shown is a single crystal transmission type or Laue monochromator. The work shown here is primarily from a double crystal reflection or Bragg type monochromator (DCM) [22]. It has been shown that both types of monochromators can be used, however the Laue type monochromator is more tolerant to heat loading from the source though typically limited to higher x-ray energies (~>20 keV).

Figures 3- 1b and 3- 1c show two horizontally separated portions of the beam from the monochromator. Figure 3- 1b shows the unfiltered beam (beam side) plus the detector and 3- 1c shows the K-edge filter (edge side) on the same, but horizontally displaced part of the detector. The system records the photon beam profile produced by a bend magnet (BM) source monochromatized by a crystal. The photon energy is tuned to the absorption K-edge of a selected filter, which partially covers the horizontal BM fan. The filtered and unfiltered beam profiles are recorded by an area detector and are fitted to appropriate functions. The vertical electron beam position and angle information are extracted from the parameters of these fits [21].

In addition, the vertical electron beam source size and divergence (emittance) information is carried in the measured widths of the unfiltered and filtered beam. These measured widths include other contributions that will now be discussed.

3.3.1 Contributions to the unfiltered beam width

The measured spatial photon beam width on the unfiltered beam side, σ_{beam}, on the detector at a distance *D* from the source includes a convolution of the vertical electron source size, $\sigma_{y_{eSource}}$, the divergence of the electron source, $\sigma_{y'_{eSource}}$, and the opening angle of the photon beam [23] , $\sigma_{y'_{Ph}}$. Here $\sigma_{y'_{Ph}}$ is modelled as a Gaussian distribution which is a good approximation when the photon energy is well above the critical energy of the source. This relation is shown in Equation (3. 1) where the contributions to the beam width are all assumed to be Gaussian distributions, so they add in quadrature.

$$\sigma_{beam}^2 = \sigma_{y_{eSource}}^2 + (D\sigma_{y'_{eSource}})^2 + (D\sigma_{y'_{Ph}})^2. \tag{3. 1}$$

The divergence of the electron beam at the source can be calculated as

$$\sigma_{y'_{eSource}} = \frac{1}{D}\sqrt{\sigma_{beam}^2 - \sigma_{y_{eSource}}^2 - (D\sigma_{y'_{Ph}})^2}. \tag{3. 2}$$

From Equation (3. 2), measurements of σ_{beam}, $\sigma_{y_{eSource}}$ and $\sigma_{y'_{Ph}}$ are required in addition to *D* to determine $\sigma_{y'_{eSource}}$.

Equation (3. 1) has no contributions from the monochromator which can be understood by considering the DuMond diagram [24] for a monochromator with a synchrotron source. This is

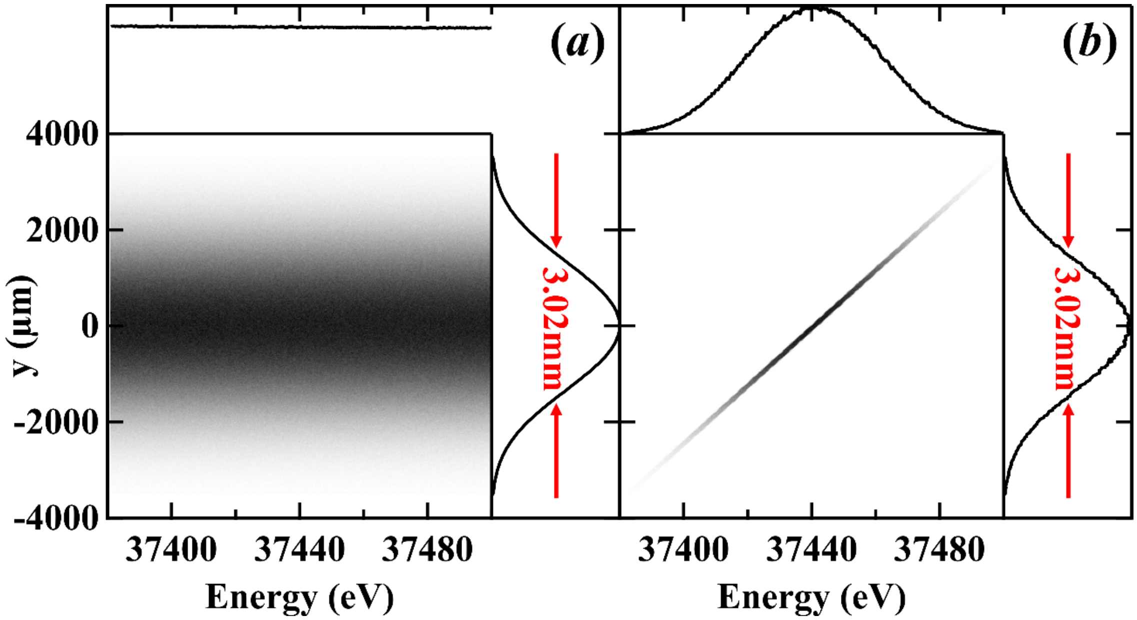

Figure 3- 2 Simulated vertical beam profile on the detector at 26 m from the source as a function of photon energy (a) without and (b) with the monochromator. The FWHM size of the two profiles shows that the presence of the monochromator has no effect on the detected beam size

demonstrated in Figure 3- 2 which was modelled with a ray-tracing simulation around the K-edge of barium at 37.441 keV using ShadowOui [25] in the OASYS environment [26].

The determination of $\sigma_{y_{eSource}}$ arises from the K-edge measurement and is described next.

3.3.2 Contributions to the measured K-edge width of the filtered beam

The filtered beam profile measured on the detector has an energy distribution because of the vertical divergence of the beam which allows the effects of the K-edge to be observed spatially. For this discussion the focus will be on the vertical distribution of this measured edge.

The K-edge in the measurements appears as a smoothed step function and is modelled as an error function (an integral of a Gaussian). A derivative of the data results in a Gaussian-type peak.

The measured K-edge width of this peak, σ_{edge}, includes the vertical electron source size, $\sigma_{y_{eSource}}$, the natural angular width of the K-edge, $\sigma_{y'_{K-edge}}$, and the intrinsic angular width of the monochromator [27, 28], $\sigma_{y'_{mono}}$ taken in quadrature; this is shown in Equation (3. 3).

$$\sigma_{edge}^2 = \sigma_{y_{eSource}}^2 + (D\sigma_{y'_{K-edge}})^2 + (D\sigma_{y'_{mono}})^2. \tag{3. 3}$$

From equation (3. 3),

$$\sigma_{y_{eSource}} = \sqrt{\sigma_{edge}^2 - (D\sigma_{y'_{K-edge}})^2 - (D\sigma_{y'_{mono}})^2}. \tag{3. 4}$$

3.3.2.1 Natural angular width of the K-edge and the monochromator

The K-edge is a characteristic absorption feature of an element where the absorption changes for photon energies at and above the binding energy, E_K, of inner shell electrons. The absorption around this edge is broadened by the core-hole lifetime. The core level broadening can be assumed as a Gaussian function with a width of $\sigma_{E_{K-edge}}$ in energy [29]. Because of the energy dispersion effect of the monochromator crystal, the energy edge width can be converted to an angular width given by

$$\sigma_{y'_{K-edge}} = \frac{\tan\theta_K}{E_K}\sigma_{E_{K-edge}}, \tag{3. 5}$$

where θ_K is the Bragg angle of the crystal at E_K. Figure 3- 3 shows the calculated photon beam profile with a barium filter whose K-edge is 37.441 keV with a Si (2,2,0) DCM. The ray-tracing calculations were done at a distance D from the source with a filter having (Figure 3- 3a) both a sharp width ($\sigma_{E_{K-edge}}$= 0 eV) K-edge and (Figure 3- 3b) a finite width ($\sigma_{E_{K-edge}}$= 5.6 eV). The K-edge broadening of the energy scale is projected onto the spatial scale, $D\sigma_{y'_{K-edge}}$, on the detector based on Equation (3. 5). One should note that for the filter with a sharp K-edge (Figure 3- 3a),

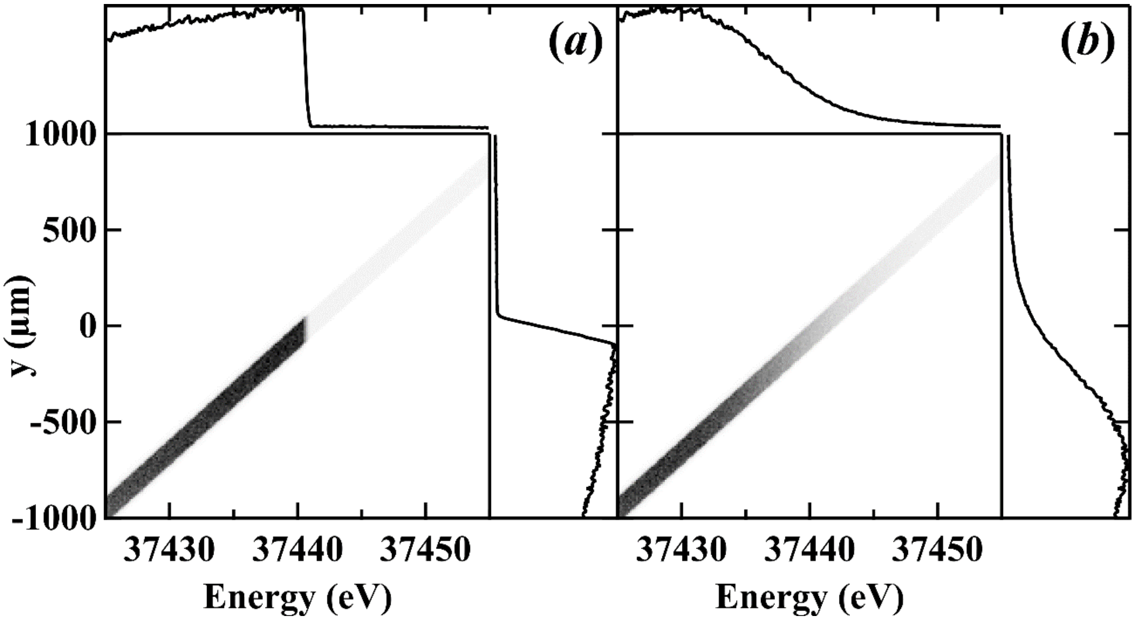

Figure 3- 3 Simulated vertical beam profile as a function of photon energy after (a) a filter with sharp absorption edge at 37.441 keV and (b) a barium filter with a 13.2 eV K-edge width. The edge size in (a) shows the effect of the monochromator broadening, and in (b) shows the broadening effect of both the monochromator and the filter K-edge.

the spatial edge width on the detector is non-zero due to the contribution of the monochromator crystal, $D\sigma_{y'_{mono}}$.

3.3.2.2 Electron source size effects

As was shown in the 2015 publication where the beam position and angle were determined by the ps-BPM system, the edge location identifies with the position of the electron source [21]. For this reason, the spatial broadening of the K-edge is a direct measurement of the source size. Figure 3- 4 illustrates this effect for the case where $\sigma_{y_{eSource}}$= 0 (Figure 3- 4a) and $\sigma_{y_{eSource}}$ =500 μm (Figure 3- 4b). Note the broadening of the K-edge as projected on the y-axis.

The results of section 2 show that by having the measurements of the K-edge filtered side and unfiltered beam side available at the same time one can compute the vertical size and

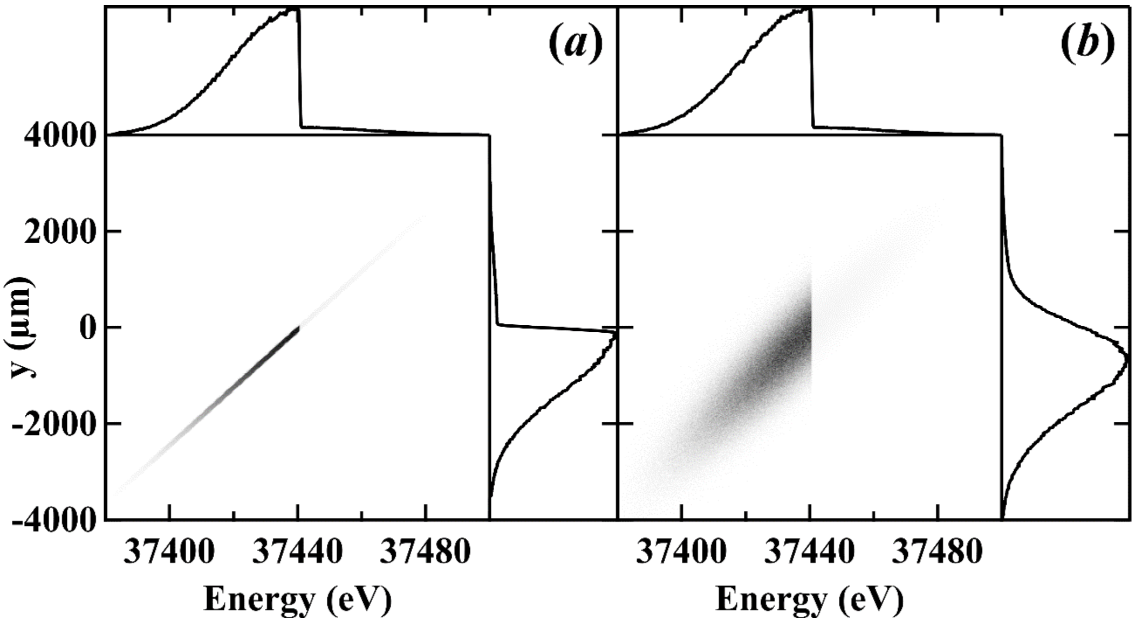

Figure 3- 4 Simulated vertical beam profile as a function of photon energy to show the effect of the electron source size on the filtered edge side of the beam. (a) A electron source with zero emittance and (b) a Gaussian electron source with 510 μm vertical size

divergence of the electron beam if the contributions from the terms $\sigma_{y'_{Ph}}$, $\sigma_{y'_{K-edge}}$ and $\sigma_{y'_{mono}}$ along with the source-to-detector distance, *D*, are known.

3.4 MEASUREMENTS AND RESULTS

3.4.1 Experimental Setup

Experiments were done at the Biomedical Imaging and Therapy bend magnet (BMIT-BM) beamline [30, 31] at the Canadian Light Source (CLS) with photon beam energy at the barium (37.441 keV) K-edge selected using a silicon (2,2,0) DCM. A combination of 0.1 mm aluminum and 0.25 mm copper filters were used to reduce the heat load on the monochromator to less than 2 W over the full width of the beam and normal storage ring operating conditions.

Part of the horizontal width of the beam was filtered with a 60 mg cm^{-2} barium solution absorber. Both filtered and unfiltered parts of the beam were intercepted by a flat panel Hamamatsu (Hamamatsu Photonics, Hamamatsu City, Shizuoka Pref., Japan) detector with a pixel size of 100 μm × 100 μm and 33 Hz frame rate to record the images. For this application the detector was at 26 m from the source.

3.4.2 Data Analysis

The unfiltered beam side and filtered edge side of the beam were recorded simultaneously and analyzed using programs written in IDL (Interactive Data Language; ITT Visual Information Solutions, Boulder, CO, USA). The detector dark response (image of the detector with no beam) was subtracted from both the unfiltered and K-edge filtered sides of the data. The data was then averaged over a select horizontal region to generate one-dimensional vertical beam profiles (unfiltered and K-edge filtered). The quantity σ_{beam} in Equation (3. 2) was obtained by fitting the profile from the unfiltered beam side to a Gaussian.

The K-edge filtered profile was then normalized by the unfiltered profile. The derivative of the negative logarithm of this normalized profile was also fit to a Gaussian. The width of the fit (RMS value) is the factor σ_{edge} in Equation (3. 3). The contributions of the natural angular width of the K-edge and the monochromator were determined through a numerical error minimization procedure as described in the results section. This total contribution was then subtracted in quadrature from σ_{edge} based on Equation (3. 4) to solve for the vertical electron beam size at the source, $\sigma_{y_{eSource}}$.

The divergence of the photon beam was calculated and fit to a Gaussian to solve for $\sigma_{y'_{Ph}}$. Referring to Equation (3. 2), the divergence of the electron beam at the source, $\sigma_{y'_{eSource}}$, was then calculated by subtracting in quadrature $\sigma_{y_{eSource}}$, which was obtained from the K-edge filtered side and the calculated $\sigma_{y'_{Ph}}$.

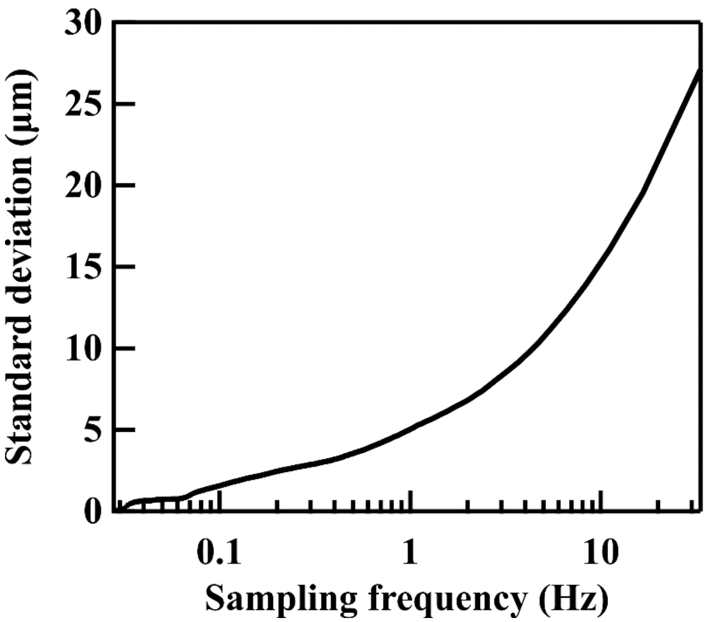

Figure 3- 5 RMS error of the extracted electron source size as a function of sampling frequency

The RMS fitting error was found by averaging the data over various time scales to simulate different sampling frequencies. The RMS error values are plotted as a function of sampling frequency in Figure 3- 5. To achieve higher accuracy, longer integration time (lower sampling frequency) is needed. A sampling frequency of 0.33 Hz was chosen which gave an RMS value of less than 5% of the electron beam size across all measurements. Note that this sampling frequency was limited by the achievable intensity across the small photon beam width that was taken.

3.4.3 Results

Measurements were performed during special operation shifts at the CLS while the size of the electron beam was changed by altering the vertical - horizontal coupling using different currents in skew quads. This method of changing the source size and divergence was chosen since it does not change the machine beta-functions in the storage ring.

The data was compared with measurements recorded with a 30µm pinhole camera at a diagnostic BM beamline, X-ray Synchrotron Radiation (XSR) [32]. The pinhole measurements

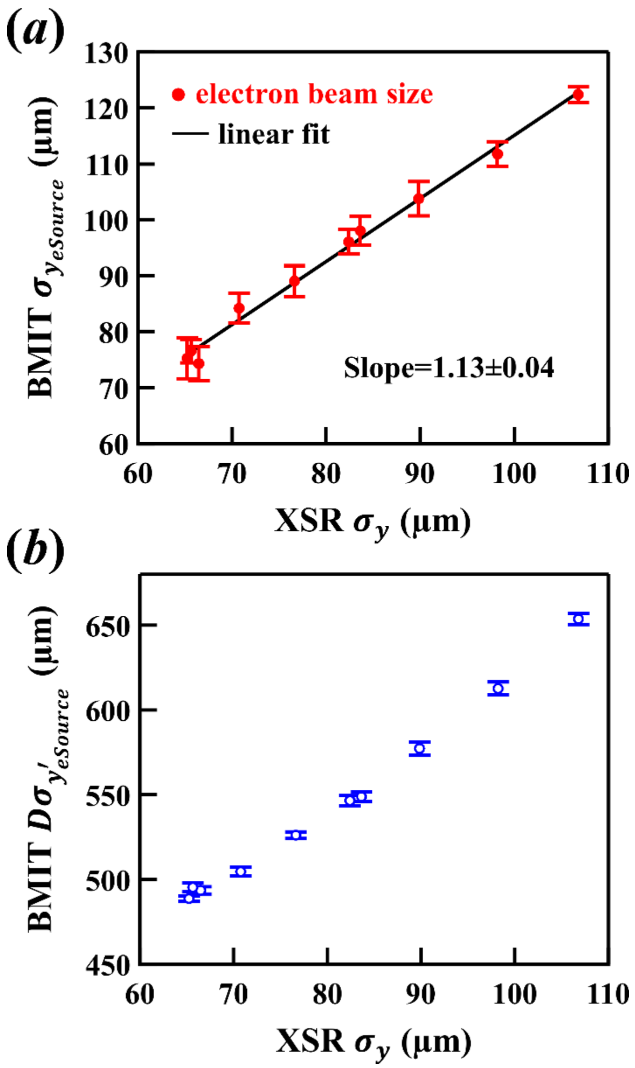

Figure 3- 6 Measured (a) electron source size and (b) electron source divergence using the ps-BPM system at the BMIT beamline. The horizontal axis is the size measured using a pinhole setup at the XSR diagnostic beamline

were made at the same time as the ps-BPM measurements. The measured electron source size with the ps-BPM system at the barium K-edge is shown in Figure 3- 6a compared against the source size measured by the pinhole. Since the pinhole cannot measure the divergence of the source, the measured divergence with the ps-BPM system is also plotted against the size values from the pinhole measurement (see Figure 3- 6b). Each data point was obtained with a sampling rate of 0.33 Hz over a total of 40 second period.

The size contribution by the natural angular width of the K-edge, $D\sigma_{y'_{K-edge}}$, and the monochromator, $D\sigma_{y'_{mono}}$, corresponds to a vertical width of 386.6 µm on the detector when added in quadrature. This vertical width was determined by a numerical minimization procedure involving a fit to measured ps-BPM data as a function of XSR values to achieve the best linear zero-intercept result while varying the vertical width parameter.

Table 3- 1 Measured electron source size ($\sigma_{y_{XSR}}$) by a pinhole at the XSR beamline made as the vertical source size was changed using skew quadruples. Included are measurements by the ps-BPM system at BMIT beamline of the electron source size ($\sigma_{y_{eSource}}$), average source position ($\bar{y}_{eSource}$), divergence ($\sigma_{y'_{eSource}}$), average angular position ($\overline{y'}_{eSource}$), and the average beam position ($\bar{y}_{eSource}$+$D\overline{y'}_{eSource}$).

$\sigma_{y_{XSR}}$ (µm)	**$\sigma_{y_{eSource}}$ (µm)**	**$\bar{y}_{eSource}$ (µm)**	**$\sigma_{y'_{eSource}}$ (µrad)**	**$\overline{y'}_{eSource}$ (µrad)**	**$\bar{y}_{eSource}$+$D\overline{y'}_{eSource}$ (µm)**
83.6	98.0±2.6	271±8	21.11±0.11	0.90±0.61	294±15
76.6	89.1±2.8	277±8	20.24±0.08	0.53±0.62	290±16
70.7	84.2±2.6	277±8	19.41±0.10	0.66±0.63	294±16
66.5	74.3±3.1	283±8	18.99±0.08	0.33±0.71	291±18
65.2	75.3±3.7	278±8	18.80±0.06	0.70±0.65	297±16
65.6	76.5±2.1	276±8	19.05±0.10	0.73±0.68	295±17
82.4	96.1±2.2	269±8	21.02±0.11	0.62±0.62	285±16
89.8	103.8±3.1	266±8	22.20±0.15	0.80±0.65	286±16
98.2	111.8±2.2	263±8	23.56±0.15	0.89±0.62	286±15
106.8	122.4±1.4	261±8	25.14±0.12	0.76±0.62	281±15

The monochromator contribution, $D\sigma_{y'_{mono}}$, can be calculated using the intrinsic angular width for the monochromator crystals [27, 28] which equals to 59.4 µm on the detector (2.3 eV in

FWHM). This implies that the contribution for the natural angular width of the barium K-edge, $D\sigma_{y'_{K-edge}}$, is about 382 μm (15.0 eV in FWHM).

The 386.6 μm contribution is then subtracted in quadrature from each data point using Equation (3. 4) and the result $\sigma_{y_{eSource}}$ was plotted against XSR values (Figure 3- 6a).

The divergence of the electron source, $\sigma_{y'_{eSource}}$, shown in Figure 3- 6b is obtained from Equation (3. 2) using a calculated value of $\sigma_{y'_{Ph}}$= 48.1 μrad and the experimentally determined $\sigma_{y_{eSource}}$ values.

It should be noted that the ps-BPM system not only measures the size and divergence, but also, the position and angle of the electron source at a single location with a single set of measurements. The results of all four values are summarized in the Table 3- 1 where $\bar{y}_{eSource}$ and $\overline{y'}_{eSource}$ are the position and angle of the electron source, respectively.

3.4.4 Simulation to study ps-BPM sensitivity

To assess the sensitivity of the system for measuring beam properties that determine the emittance as well as assessing other optical arrangements, ray-tracing simulations were performed.

The bending magnet source was simulated with the built-in widget in ShadowOui. The nominal electron beam size input is $\sigma_{y_{eSource}}$= 51.3 μm with divergence of $\sigma_{y'_{eSource}}$= 9.83 μrad. An energy bandwidth of 100 eV around the barium K-edge (37.441 keV) was used in the simulation to ensure coverage of the full phase and energy space of the system. To minimize statistical error, a total of 5×10^7 rays were used in each calculation. The simulation error is defined as the RMS deviation of ten calculations.

The monochromator was simulated with the DCM widget in ShadowOui with the dispersion effect of the plane crystals taken into account. The K-edge filter absorption was

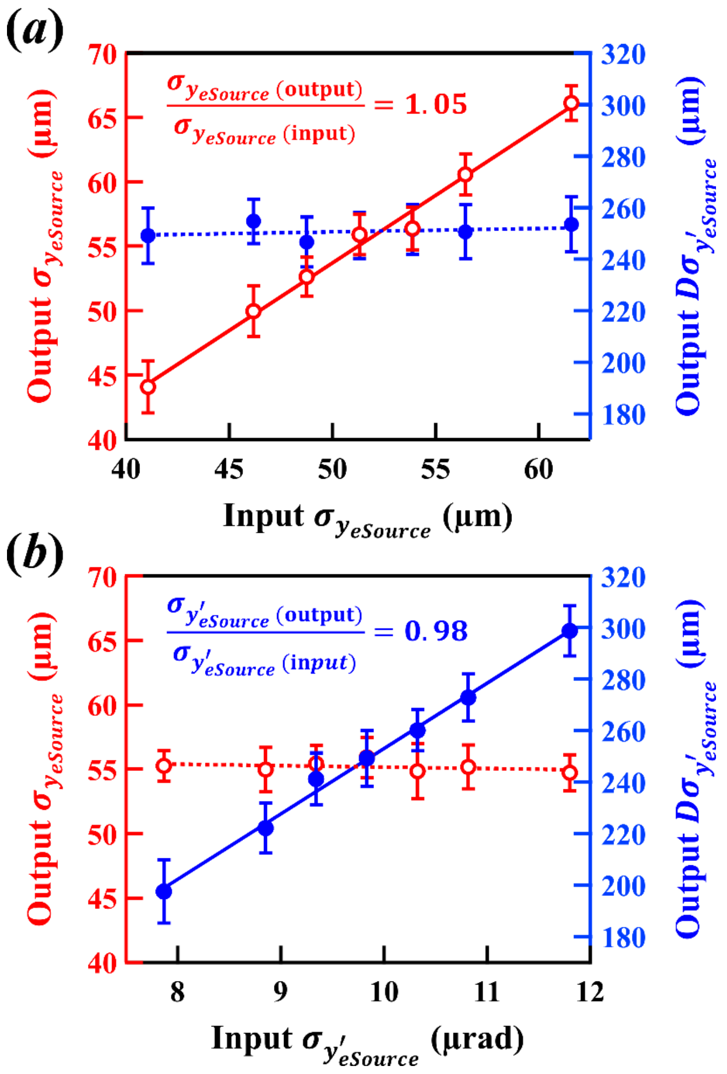

Figure 3- 7 Simulation studies of the sensitivity of the ps-BPM system. Extracted electron source size (open markers) and divergence (closed markers) from different input values of (a) the electron source size and (b) the divergence

calculated with a Python script that appropriately attenuates the rays after the monochromator. The transmitted rays through the filter were collected into a histogram at the detector plane, where the bin size represents the detector pixel size.

The simulated beam profiles (the histogram) with and without the K-edge absorption filter were then analyzed using the same data analysis process as the experimental results. The output of each calculation gives the unfiltered beam and K-edge filtered beam widths.

Calculations were done with zero electron beam source size and divergence (zero emittance) to determine the photon, monochromator and K-edge contributions that are needed in Equation (3. 2) and (3. 4).

Results obtained from ten bend magnet and ten zero emittance source simulations show expected measured values of $\sigma_{y_{eSource}}$ = 55.9 ± 1.6 μm (input value = 51.3 μm) and $\sigma_{y'_{eSource}}$= 9.59 ± 0.35 μrad (input value = 9.83 μrad).

For sensitivity studies, simulations were done by varying the electron beam source size and divergence. The inputs $\sigma_{y_{eSource}}$ and $\sigma_{y'_{eSource}}$ were scanned about their nominal values. The results were processed the same as described above and plotted in Figure 3- 7.

The results indicate that the system can easily detect 5% changes in the source size and angle.

3.4 DISCUSSION AND CONCLUSIONS

The determination of the emittance properties from electron storage rings is becoming more important as sources are becoming brighter. This paper described a new method of measuring the source size and divergence of a storage ring. The emittance of the source can then be determined if the beta function of the machine is known [33].

The ps-BPM system is capable of measuring the vertical electron beam source position, angular position, the vertical beam size and divergence at the same time. A model of the ps-BPM system has been developed for understanding how these parameters are extracted from measured beam and K-edge filtered widths. This understanding has been validated with commonly used modeling programs.

Specifically, the purpose of the simulation study was to a) validate the data analysis, b) validate the physical understanding of the system, c) study the sensitivity of the system and d) determine the contribution of the monochromator to the K-edge filtered width measurements.

Comparing the measurements of the pinhole based beamline with the ps-BPM system clearly show that changing the beam size using the skew quads can be detected by both systems. The fact that the measured values are not the same is a consequence of the electron sources being located at different beta-functions.

It should be noted that this system measures the electron source properties in one direction (vertical) and requires a bend magnet source.

The ps-BPM system measures the electron beam position and angle in real time [21]. The measurement of the source size and divergence does require longer integration time (a few seconds in the current setup). The speed can be improved by using a wider horizontal BM fan and an optimized geometry (e.g., shorter source-to-detector distance).

Further studies are planned to calibrate the system by measuring the source size with different methods at the same beamline as the ps-BPM system.

3.5 ACKNOWLEDGEMENT

The authors acknowledge the financial support of Natural Sciences and Engineering Research Council of Canada (NSERC) Discovery Grant, Canadian Institutes of Health Research (CIHR) Team Grant – Synchrotron Medical Imaging, CIHR Training Grant - Training in Health Research Using Synchrotron Techniques, Canada Research Chair Program, Saskatchewan Health Research Foundation Team Grant and the University of Saskatchewan. The research described in this paper was performed at the Canadian Light Source, which is funded by the Canada Foundation for Innovation, NSERC, the National Research Council Canada, CIHR, the Government of Saskatchewan, Western Economic Diversification Canada, and the University of Saskatchewan. This work was also supported by the U.S. Department of Energy, Office of Basic Energy Sciences, under Contract No. DE-AC02-06CH11357. The authors would like to thank Dr Luca Rebuffi (Argonne National Laboratory) for the OASYS support.

3.6 REFERENCES

1. J. Buon, "Beam phase space and emittance," CAS - CERN Accelerator School : 5th General Accelerator Physics Course, France1992.
2. M. Eriksson, J. F. van der Veen, and C. Quitmann, "Diffraction-limited storage rings - a window to the science of tomorrow," Journal of Synchrotron Radiation, vol. 21, pp. 837-842, 2014.
3. P. F. Tavares, S. C. Leemann, M. Sjostrom, and A. Andersson, "The MAX IV storage ring project," Journal of Synchrotron Radiation, vol. 21, pp. 862-877, 2014.
4. D. Einfeld, M. Plesko, and J. Schaper, "First multi-bend achromat lattice consideration," Journal of Synchrotron Radiation, vol. 21, pp. 856-861, 2014.
5. M. Borland, M. Abliz, N. Arnold, T. Berenc, A. Blednykh, J. Byrd, et al., "The upgrade of the advanced photon source," in 9th Int. Particle Accelerator Conf.(IPAC'18), Vancouver, BC, Canada, April 29-May 4, 2018, 2018, pp. 2872-2877.
6. P. Elleaume, C. Fortgang, C. Penel, and E. Tarazona, "Measuring Beam Sizes and Ultra-Small Electron Emittances Using an X-ray Pinhole Camera," Journal of synchrotron radiation, vol. 2, pp. 209-214, 1995.
7. C. Thomas, G. Rehm, I. Martin, and R. Bartolini, "X-ray pinhole camera resolution and emittance measurement," Physical Review Special Topics-Accelerators and Beams, vol. 13, p. 022805, 2010.
8. T. Weitkamp, O. Chubar, M. Drakopoulos, I. Snigireva, A. Snigirev, C. Schroer, et al., "Electron Beam Size and Profile Measurements With Refractive X-Ray Lenses," in Proceedings of EPAC 2000, 2000, pp. 1824-1826.
9. K. Iida, N. Nakamura, H. Sakai, K. Shinoe, H. Takaki, M. Fujisawa, et al., "Measurement of an electron-beam size with a beam profile monitor using Fresnel zone plates," Nuclear Instruments and Methods in Physics Research Section A: Accelerators, Spectrometers, Detectors and Associated Equipment, vol. 506, pp. 41-49, 2003/06/21/ 2003.
10. S. Takano, M. Masaki, and H. Ohkuma, "X-ray imaging of a small electron beam in a low-emittance synchrotron light source," Nuclear Instruments and Methods in Physics Research Section A: Accelerators, Spectrometers, Detectors and Associated Equipment, vol. 556, pp. 357-370, 2006/01/01/ 2006.
11. T. Renner, H. Padmore, and R. Keller, "Design and performance of the ALS diagnostic beamline," Review of Scientific Instruments, vol. 67, pp. 3368-3368, 1996.
12. T. Mitsuhashi, Beam Measurement: Proceedings of the Joint US-CERN-Japan-Russia School on Particle Accelerators, Montreux, and CERN, Switzerland: World Scientific Publishing Company, 1999.
13. T. Naito and T. Mitsuhashi, "Very small beam-size measurement by a reflective synchrotron radiation interferometer," Physical Review Special Topics-Accelerators and Beams, vol. 9, p. 122802, 2006.

14. J. Corbett, X. Huang, C. Li, T. Mitsuhashi, J. Wu, Y. Xu, et al., "Transverse Beam Profiling and Vertical Emittance Control with a Double-Slit Stellar Interferometer," in 5th Int. Beam Instrumentation Conf.(IBIC'16), Barcelona, Spain, Sept. 13-18, 2016, 2017, pp. 237-240.

15. J. P. Guigay, S. Zabler, P. Cloetens, C. David, R. Mokso, and M. Schlenker, "The partial Talbot effect and its use in measuring the coherence of synchrotron X-rays," Journal of synchrotron radiation, vol. 11, pp. 476-482, 2004.

16. X. Shi, S. Marathe, M. J. Wojcik, N. G. Kujala, A. T. Macrander, and L. Assoufid, "Circular grating interferometer for mapping transverse coherence area of X-ray beams," Applied Physics Letters, vol. 105, p. 041116, 2014.

17. M. Lyubomirskiy, I. Snigireva, V. Kohn, S. Kuznetsov, V. Yunkin, G. Vaughan, et al., "30-Lens interferometer for high-energy X-rays," Journal of synchrotron radiation, vol. 23, pp. 1104-1109, 2016.

18. V. Kohn, I. Snigireva, and A. Snigirev, "Direct measurement of transverse coherence length of hard x rays from interference fringes," Physical review letters, vol. 85, p. 2745, 2000.

19. Å. Andersson, M. Böge, A. Lüdeke, V. Schlott, and A. Streun, "Determination of a small vertical electron beam profile and emittance at the Swiss Light Source," Nuclear Instruments and Methods in Physics Research Section A: Accelerators, Spectrometers, Detectors and Associated Equipment, vol. 591, pp. 437-446, 2008.

20. W. B. Peatman and K. Holldack, "Diagnostic front end for BESSY II," Journal of Synchrotron Radiation, vol. 5, pp. 639-641, 1998.

21. N. Samadi, B. Bassey, M. Martinson, G. Belev, L. Dallin, M. de Jong, et al., "A phase-space beam position monitor for synchrotron radiation," J Synchrotron Radiat, vol. 22, pp. 946-55, Jul 2015.

22. J. A. Golovchenko, R. A. Levesque, and P. L. Cowan, "X-ray monochromator system for use with synchrotron radiation sources," Review of Scientific Instruments, vol. 52, pp. 509-16, 04/ 1981.

23. J. Schwinger, "On the classical radiation of accelerated electrons," Physical review, vol. 75, p. 1912, 1949.

24. J. W. M. DuMond, "Successive x-ray crystal reflections to obtain increased resolving power," Physical Review, vol. 52, pp. 872-883, 10/15 1937.

25. L. Rebuffi and M. Sanchez del Rio, "ShadowOui: a new visual environment for X-ray optics and synchrotron beamline simulations," Journal of Synchrotron Radiation, vol. 23, pp. 1357-1367, 2016.

26. L. Rebuffi and M. S. d. Rio, "OASYS (OrAnge SYnchrotron Suite): an open-source graphical environment for x-ray virtual experiments," in SPIE Optical Engineering + Applications, 2017, p. 9.

27. B. E. Warren, X-ray Diffraction: Courier Corporation, 1990.

28. W. H. Zachariasen, Theory of X-ray Diffraction in Crystals. New York: John Wiley, 1945.

29. Y. A. Babanov, A. V. Ryazhkin, A. F. Sidorenko, and L. A. Blaginina, "Correcting an experimental absorption spectrum for the core level width," Journal of Structural Chemistry, vol. 39, pp. 833-838, November 01 1998.

30. T. W. Wysokinski, D. Chapman, G. Adams, M. Renier, P. Suortti, and W. Thomlinson, "Beamlines of the biomedical imaging and therapy facility at the Canadian light source—Part 1," Nuclear Instruments and Methods in Physics Research Section A: Accelerators, Spectrometers, Detectors and Associated Equipment, vol. 582, pp. 73-76, 2007.

31. T. W. Wysokinski, D. Chapman, G. Adams, M. Renier, P. Suortti, and W. Thomlinson, "Beamlines of the biomedical imaging and therapy facility at the Canadian Light Source-Part 2," in Journal of Physics: Conference Series, 2013, p. 072013.

32. J. C. Bergstrom and J. M. Vogt, "The X-ray diagnostic beamline at the Canadian Light Source," Nuclear Instruments and Methods in Physics Research Section A: Accelerators, Spectrometers, Detectors and Associated Equipment, vol. 587, pp. 441-457, 2008.

33. K. Floettmann, "Some basic features of the beam emittance," Physical Review Special Topics-Accelerators and Beams, vol. 6, p. 034202, 2003.

CHAPTER 4

This paper was submitted to the Physical Review Accelerators and Beam in June 2019 and is under review.

The author took all of the data and did all of the data analysis. The author arranged for the beamtime and coordinated data acquisition with the beam size studies. Others were involved in data analysis and simulations (Shi), storage ring properties (Dallin) and algorithm development (Chapman). The author, Dr. Shi and Prof. Chapman prepared the manuscript draft which was reviewed by Dr Dallin.

APPLICATION OF A PHASE SPACE BEAM POSITION AND SIZE MONITOR FOR SYNCHROTRON RADIATION SOURCE CHARACTERIZATION

Nazanin Samadi[a]*, Xianbo Shi[b], Les Dallin[c], Dean Chapman[c&d]

[a]Physics and Engineering physics, University of Saskatchewan, 116 Science Place, Saskatoon, SK, S7N 5E2 Canada
[b]Advanced Photon Source, Argonne National Laboratory, 9700 S. Cass Ave., Lemont, Illinois, 60439, USA
[c]Canadian Light Source, 44 Innovation Boulevard, Saskatoon, SK, S7N 2V3, Canada
[d]Anatomy, Physiology and Pharmacology, University of Saskatchewan, 107 Wiggins Road, Saskatoon, SK, S7N5E5, Canada
Correspondence email: nazanin.samadi@usask.ca

Keywords: beam emittance monitor; x-ray diffraction; phase space; diagnostics and feedback

Synopsis An electron beam position and angle monitoring system, ps-BPM, has been shown to be able to measure the electron source position and angle at a single location in a beamline at a synchrotron source. This system is now shown to be capable of measuring the source size and divergence simultaneously

4.1 ABSTRACT

A phase space beam position and size monitor (ps-BPM) system was introduced previously to measure the electron source vertical position and angular motion along with the vertical source size and angular size at a single location in a synchrotron bend magnet beamline. The system uses a combination of a monochromator and a filter with a K-edge to which the monochromator was tuned in energy. The vertical distribution of the photon beam with and without the filter was simultaneously visualized with an imaging detector. The small range of angles from the source onto the monochromator crystals creates an energy range that allows part of the photon beam to be below the K-edge and the other part above. Measurement of the vertical beam location without the absorber and vertical edge location with the absorber allows measurement of the source position and angle. The photon beam width and edge width give information about the vertical electron source size and divergence. In this work, we show a typical measurement with the ps-BPM monitor and results that can be obtained from a single measurement. By combining the analysis in the time and frequency domain, information on beam motion and size can be extracted and identified from both the source and the beamline optics. Applications of the ps-BPM system at the Canadian Light Source are demonstrated by studying beam vibrations and machine insertion device field changes.

4.2 INTRODUCTION

Accurate measurements of the electron source size and divergence are becoming increasingly important at synchrotron facilities as the next generation light sources are being built with the goal on achieving the smallest possible emittance [1, 2].

Currently available ways of measuring the source size are relying on direct imaging or interference-based techniques. Direct imaging methods include pinhole imaging [3, 4], imaging with Kirkpatrick-Baez (KB) mirrors [5], Compound Refractive Lenses (CRLs) [6] and Fresnel

Zone Plates (FZP) [7, 8]. The interferometry based systems include double-slit diffraction [9-11], grating interferometry [12, 13], and π-polarization [14].

In addition to the importance of measuring the source size at these next generation light sources, beam stability is also of great concern. Real-time measurements of the position and angular position of the electron beam at a single location will be a powerful tool as a monitor, a diagnostic element, and in a feedback system.

A phase space beam position and size monitor (ps-BPM) system was introduced previously [15, 16], that measures, in real time, all four quantities (size, divergence, position, and angular position) of the electron source in the vertical plane from a single measurement. In this work, applications of the ps-BPM system in studying the beam performance are demonstrated with experimental results at the Canadian Light Source (CLS).

4.3 PS-BPM SYSTEM

4.3.1 System overview

The ps-BPM system uses the nearly monochromatic photon beam provided by a crystal monochromator around an absorption K-edge of a selected filter element (see Figure 4- 1). The monochromator can be of a reflection type (Bragg geometry) or transmission type (Laue geometry). Half of the horizontal size of the photon beam is covered by the K-edge filter (Figure 4- 1 c Edge Side) and the other half has no filter in the way (Figure 4- 1 b Beam Side). Both halves of the beam are then imaged with an area detector.

The unfiltered beam side of the image data is summed over a horizontal width, and the beam profile is shown just next to the detector symbol in Figure 4- 1 b and in Figure 4-1 a. This

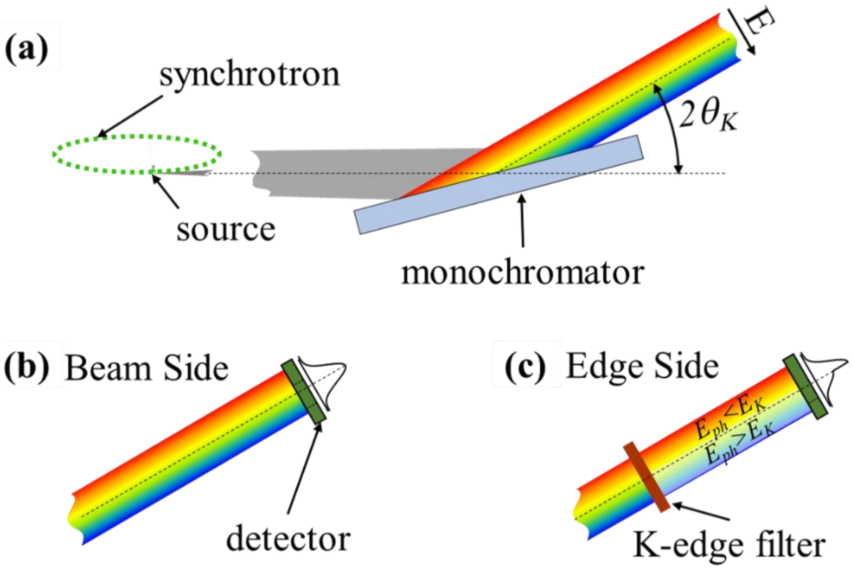

Figure 4- 1 Schematic of the ps-BPM system containing (a) the crystal monochromator, the K-edge filter, and the detector. A single crystal Bragg geometry is shown. Figures (b) and (c) show the unfiltered beam size and the filtered edge side of the beam, respectively.

profile is fit with a Gaussian function from which the center location of the photon beam, y_{beam}, and the Gaussian distribution width, σ_{beam}, is obtained.

For the filtered beam side, the image data is also summed over a horizontal width as shown in Figure 4- 1 c and Figure 4- 2 b. This profile is then normalized by the unfiltered beam. The negative logarithm of this normalized filtered beam profile is taken to convert the filtered data to an absorption profile which then resembles the step function associated with the K-edge of the element as shown in Figure 4- 2 c. A spatial derivative is taken of this step-like function forming a peak that is then fit by a Gaussian function from which we have an edge location, y_{edge}, and width, σ_{edge}, as shown in Figure 4- 2 d.

4.3.2 Source position and angle measurements

Referring to Figure 4- 1, when the electron source moves, the detected photon beam on the beam and edge sides may behave differently. For example, if the electron source has a fixed

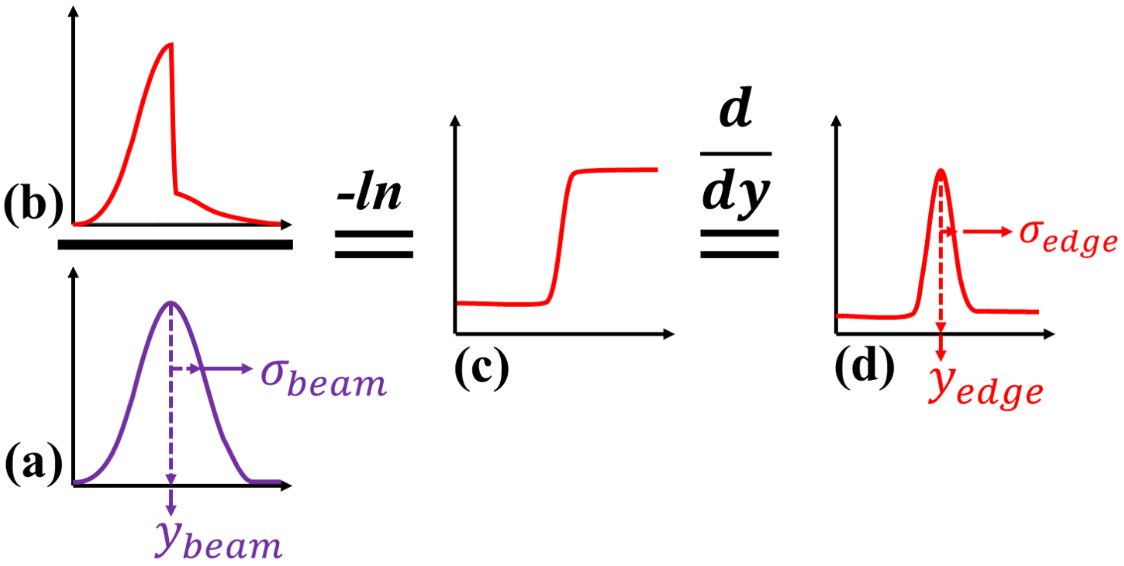

Figure 4- 2 Beam and edge analysis. (a) Beam profile along with Gaussian fit parameters. (b) Edge profile which is then normalized by (a). The negative logarithm of this normalized profile is shown in (c). The spatial derivative of the profile in (c) results in a peak shown in (d) along with its Gaussian fit parameters

position but a changing angle, the detected photon beam on the beam side will move vertically according to the angle and the distance the detector is from the source point. However, on the edge side, the edge location will not move as the monochromator will select out the same energy from the angular distribution of the source. This is because the angle of the photon beam to the monochromator crystal is directly related to the energies diffracted by the monochromator by Bragg’s law.

Now if the electron beam is fixed in angle but moves vertically in position, the photon beam on the beam side will also move vertically as will the edge location on the edge side. Thus, there is a simple relationship between the vertical angle and position of the electron beam to the measured photon beam and edge locations. This then can be used to determine, independently, the vertical position and angle of the electron source [15].

4.3.2.1 Filtered K-edge side

As has been previously discussed, the location of the K-edge on the filtered K-edge side of the data is only sensitive to the electron beam position and not to the angular position of the electron beam. As shown graphically in Figure 4- 2 d, the center of the Gaussian fit to the filtered K-edge side (y_{edge}) is a direct measure of the electron source position y as

$$y = y_{edge}. \tag{3. 4}$$

4.3.2.2 Unfiltered side

The unfiltered beam side of the data includes the position y and angular position y' of the electron source according to

$$y_{beam} = y + Dy', \tag{4. 1}$$

where D is the source-to-detector distance.

By having the two measurements at the same time with the ps-BPM system, we can solve for the angular position of the electron source, y', based on Equation (4. 1) and (4. 2) as

$$y' = \left(y_{beam} - y_{edge}\right)/D. \tag{4. 2}$$

4.3.3 Source size and divergence measurements

The previous discussion shows that the measurement of the center of the photon beam and edge distribution identifies the position and angle of the electron source. It then follows that an extension of the source size in either position and angle will result in a widening of the photon beam and/or edge distributions.

For the following discussion we will assume that the source size and divergence will be Gaussian distributions along with other factors that may contribute to the measured widths arising from the optics, the filter material and the natural opening angle of the photon beam from the source. Thus, the measured photon beam and edge widths are the sum, in quadrature, of the appropriate contributions.

4.3.3.1 Filtered K-edge side

The spatial width σ_{edge} of the Gaussian fit from the filtered K-edge side of the photon beam includes contributions from the natural width of the K-edge filter element $\sigma_{y'_{K-edge}}$, the angular acceptance of the monochromator $\sigma_{y'_{mono}}$, and the vertical size of the electron source σ_y, all added in quadrature as

$$\sigma_{edge}^2 = \sigma_y^2 + (D\sigma_{y'_{K-edge}})^2 + (D\sigma_{y'_{mono}})^2. \tag{4. 3}$$

The electron source size σ_y is then,

$$\sigma_y = \sqrt{\sigma_{edge}^2 - \left(D\sigma_{y'_{K-edge}}\right)^2 - \left(D\sigma_{y'_{mono}}\right)^2}. \tag{4. 4}$$

4.3.3.2 Unfiltered side

The measured spatial width σ_{beam} of the unfiltered side is the combination of the electron source size σ_y, divergence $\sigma_{y'}$, and the opening angle of the photon beam $\sigma_{y'_{Ph}}$, added in quadrature as

$$\sigma_{beam}^2 = \sigma_y^2 + (D\sigma_{y'})^2 + (D\sigma_{y'_{Ph}})^2. \tag{4. 5}$$

By having the opening angle of the photon beam, modelled as a Gaussian[1], and the measured σ_y from the edge side, we can solve for the divergence of the electron source as

$$\sigma_{y'} = \frac{1}{D}\sqrt{\sigma_{beam}^2 - \sigma_y^2 - (D\sigma_{y'_{Ph}})^2}. \tag{4. 5}$$

---

[1] The Gaussian distribution assumption applies when the photon energy of the selected beam is above the critical energy of the bend magnet.

This shows by having measurements of the unfiltered beam side and the filtered K-edge side we can measure the vertical position, angle, size, and divergence of the electron source at the same time. However, to arrive at these values the contributions from $\sigma_{y'_{K-edge}}$, $\sigma_{y'_{mono}}$ and $\sigma_{y'_{Ph}}$ need to be determined [16]. The $\sigma_{y'_{K-edge}}$ derives from the tabulated energy width of the K-edge filter element [17]. The $\sigma_{y'_{mono}}$ can be calculated based on the crystal material, reflection and photon energy [18]. The photon angular distribution can be calculated and then fit with a Gaussian to arrive at $\sigma_{y'_{Ph}}$[19].

4.4 RESULTS

The application of the ps-BPM system is demonstrated below to illustrate the ability to provide useful information regarding the source and even beamline properties.

4.4.1 Normal operations

Measurements using the ps-BPM system are shown to demonstrate the full characterization of the electron beam in the vertical direction during normal operations of the CLS facility. The measurements were performed at the Biomedical Imaging and Therapy (BMIT) bend magnet (BM) beamline [20-22] at the CLS. The photon energy was tuned to the barium K-edge at 37.441 keV by the Si (220) Double Crystal Monochromator (DCM). The projected concentration of the barium filter is 35 mg·cm^{-2}. The images of the filtered and unfiltered photon beam were recorded by a flat panel Hamamatsu detector (Hamamatsu Photonics, Hamamatsu City, Shizuoka Pref., Japan) at D = 20 m from the BM source. The detector pixel size were square with a linear dimension on each side of 100 μm. A total of 3000 images were taken with an acquisition time of 0.03 s for each image.

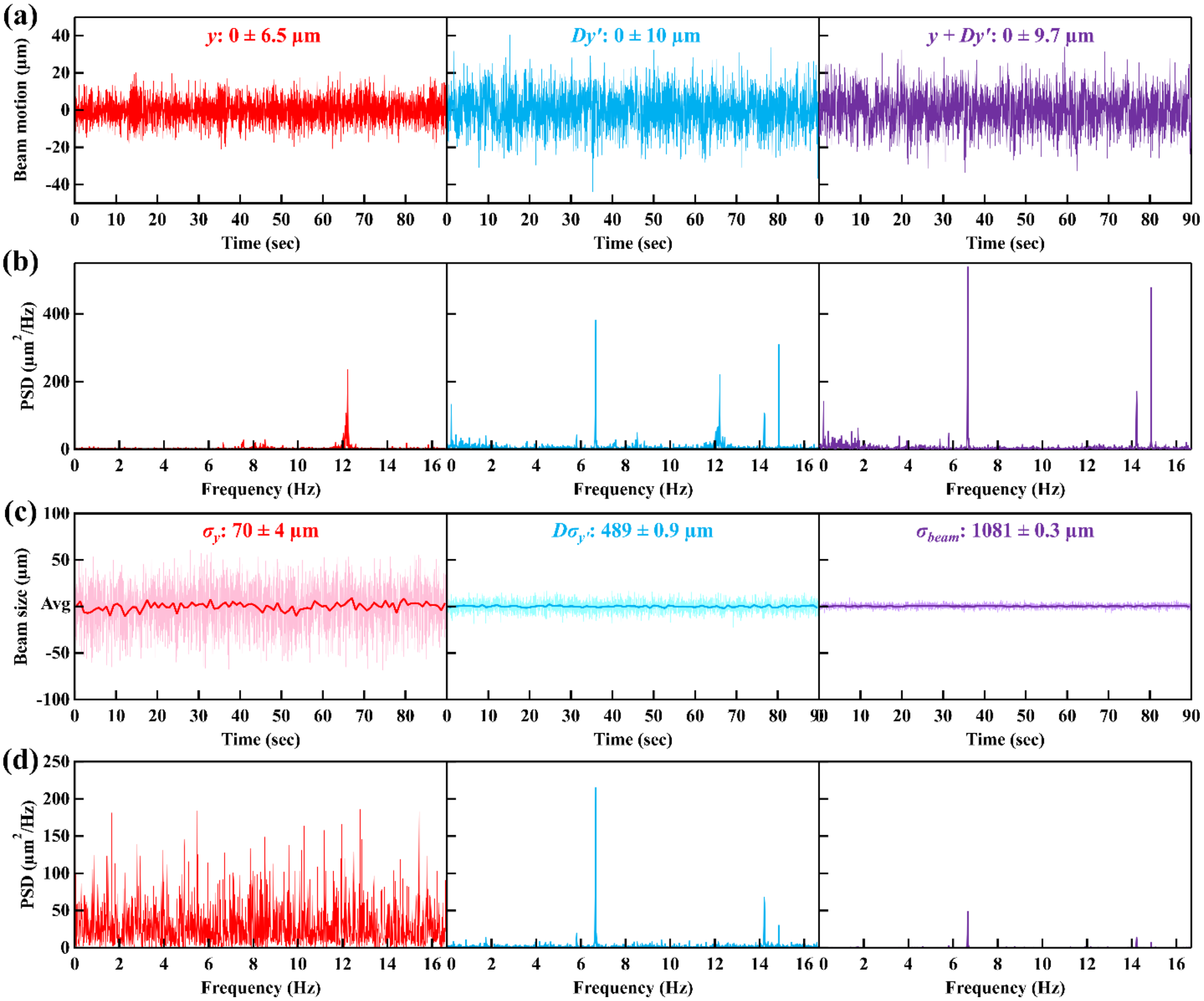

Figure 4- 3 (a) Beam motions including y (left), Dy' (middle), and $y + Dy'$ (right) as a function of time. (b) PSD functions of the three curves in (a). (c) Time evolution of σ_y (left), $D\sigma_{y'}$ (middle), and σ_{beam} (right). The light colored and dark colored curves are for sampling time of 0.03 s and 0.9 s, respectively. (d) PSD functions of the light colored curves in (c).

The measurement results are shown in Figure 4- 3. The beam positions including the source position, y, angular position projected at the detector location, Dy', and their combined position, $y_{beam} = y + Dy'$, are shown as a function of time in Figure 4- 3 a. The numbers at the tops of Figure 4- 3 a and c are the standard deviation of the three positions over the entire measurement period of 90 s. The standard deviation values are the direct evaluation of the amplitude of beam motion. At the detector location, the angular motion of the source has a larger effect than the source position motion.

The power spectral density (PSD) function, obtained from the Fourier transform of the time-dependent signal, allows characterizing the measured beam position in the frequency domain. The PSD functions of the three curves in Figure 4- 3 a are shown in Figure 4- 3 b, respectively. With the sampling rate of 33 Hz, positional variations or vibrations up to 16.7 Hz can be detected. The total beam motion, $y + Dy'$, at the detector location in the right panel of Figure 4- 3 b shows three characteristic peaks at 6.7, 14.2 and 14.9 Hz, which are clearly from the angular motion as seen in the middle panel of Figure 4- 3 b. The small frequency band around the 12.2 Hz peak, however, shows up in both the source position and angular position, but not in the combined beam position on the detector. This is an unusual case and will not be easily detected by other methods. The cause of this frequency band is the vibration of the DCM in the overall pitch angle, where both crystals rotate together (see Section III. B. for details). Because of the fixed axis geometry of DCM, the beam position at the detector will not change with the DCM vibration. However, the Bragg angle change alters the photon energy center, which is interpreted by the ps-BPM system as the source position move. On one hand, it means that the monochromator used in the ps-BPM monitor needs to be stable. More importantly, it shows the possibility of using the system to identify the optics vibration along the beamline.

The beam sizes including the source size, σ_y, angular distribution projected on the detector, $D\sigma_{y'}$, and the total beam size, σ_{beam}, are shown as a function of time in Figure 4- 3 c. All curves are offset to their own average values, which are indicated in the figure. The light colored curves are plotted in the original time scale (0.03 s steps). Since the beam size measurements are photon hungry, a longer acquisition time is needed to improve sensitivity [16]. In Figure 4- 3 c, the over

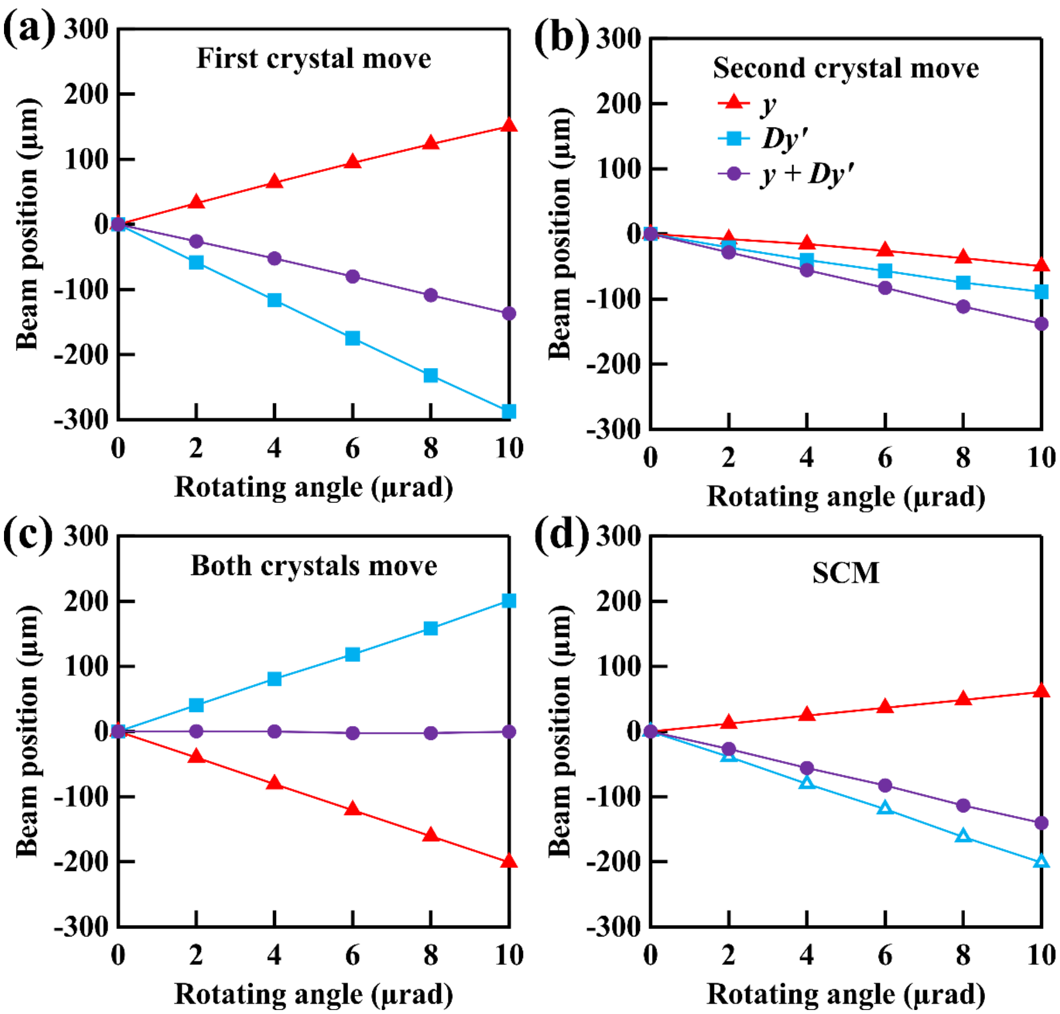

Figure 4- 4 Simulated beam position response as a function of rotation angle of (a) the first crystal, (b) the second crystal, (c) both crystals of the DCM, and (d) the SCM crystal. The markers represent the extracted source position y (triangles), projected source angle Dy' (squares), and the total beam position $y + Dy'$. The curves provide a visual aid.

plotted curves with dark colors were obtained by averaging every 30 points (0.9 s). The standard deviation values shown in the figure are also for the averaged curves which show the sensitivity of the system for each of the three parameters. An integration of 0.9 s is adequate to reach the sensitivity of 4 µm for source size measurement.

The corresponding PSD functions of the fast measurement data (light colored curves in Figure 4- 3 c) are shown in Figure 4- 3 d. The PSD function for σ_y shows only random noise indicating that the present system is not fast enough to monitor source size changes on the millisecond scale. But, the PSD functions for $D\sigma_{y'}$ and σ_{beam} show clear frequency peaks that are consistent with the ones observed in the position plots (see Figure 4- 3 b) which is an indication of adequate sensitivity.

4.4.2 Beam vibration analysis

To further understand the monochromator vibration, ray-tracing simulations were performed using ShadowOui [23] in the OASYS environment [24]. Simulation details can be found in Samadi, *et al*. [16]. Figure 4- 4 shows the beam position as a consequence of the input angular motion of the DCM crystals (Figures 4- 4 a-c) and single-crystal monochromator, SCM (Figure 4- 4 d). Among all four cases, only Figure 4- 4 c shows a zero total beam motion, $y + Dy'$ (solid circles). The source position, y, (solid triangles) and angular position, Dy', (solid squares) have the same amplitude but opposite sign. This is consistent with the experimental observation shown in Figure 4- 3 a. In all other three cases (Figures 4- 4 a, b and d), the total beam motion has the same amplitude while y and Dy' varies in amplitude and sign. Thanks to the simultaneous measurement of y and Dy' by the ps-BPM system, the vibration source of the monochromator crystals can be identified by analysing both position contributions. This is another unique feature of the ps-BPM system.

To distinguish between election source vibration and that of monochromators, additional tests and analysis will be necessary, such as to evaluate the spectral frequencies of the system. To identify the origin of the beam motion shown in Figure 4- 3, measurements were carried out with two different monochromators; a Si (220) Bragg DCM at barium K-edge and a Si (311) single Laue crystal monochromator (SCM) at iodine K-edge.

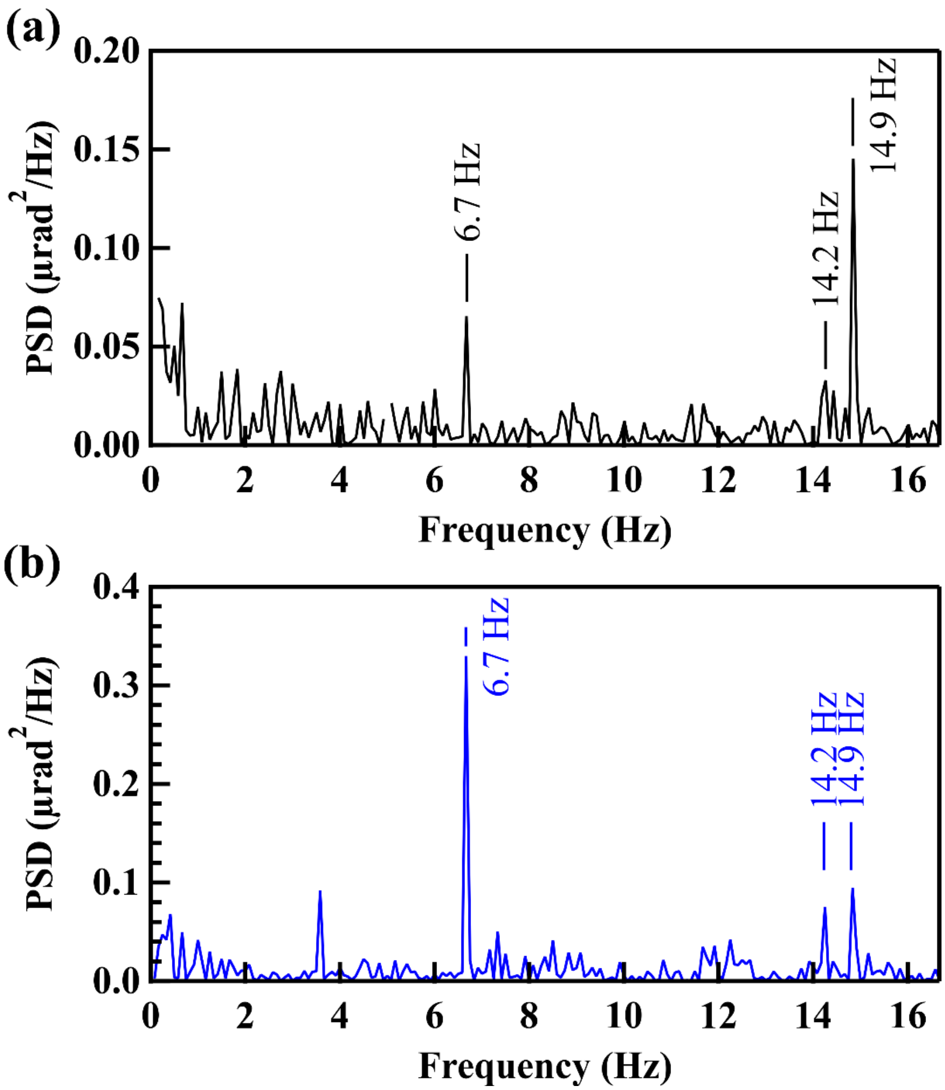

Figure 4- 5 PSD functions of the beam angle y' measured with (a) a Si (220) Laue single-crystal monochromator and (b) a Si (220) Bragg double-crystal monochromator at the barium K-edge

Figure 4- 5 shows the PSD functions of y' obtained from the two separate experiments. Both results were extracted from 400 images with a sampling rate of 0.03 s. Both PSD functions contain the 6.7 Hz, 14.2 Hz, and 14.9 Hz peaks, which is a clear indication that they are characteristic motions of the electron beam.

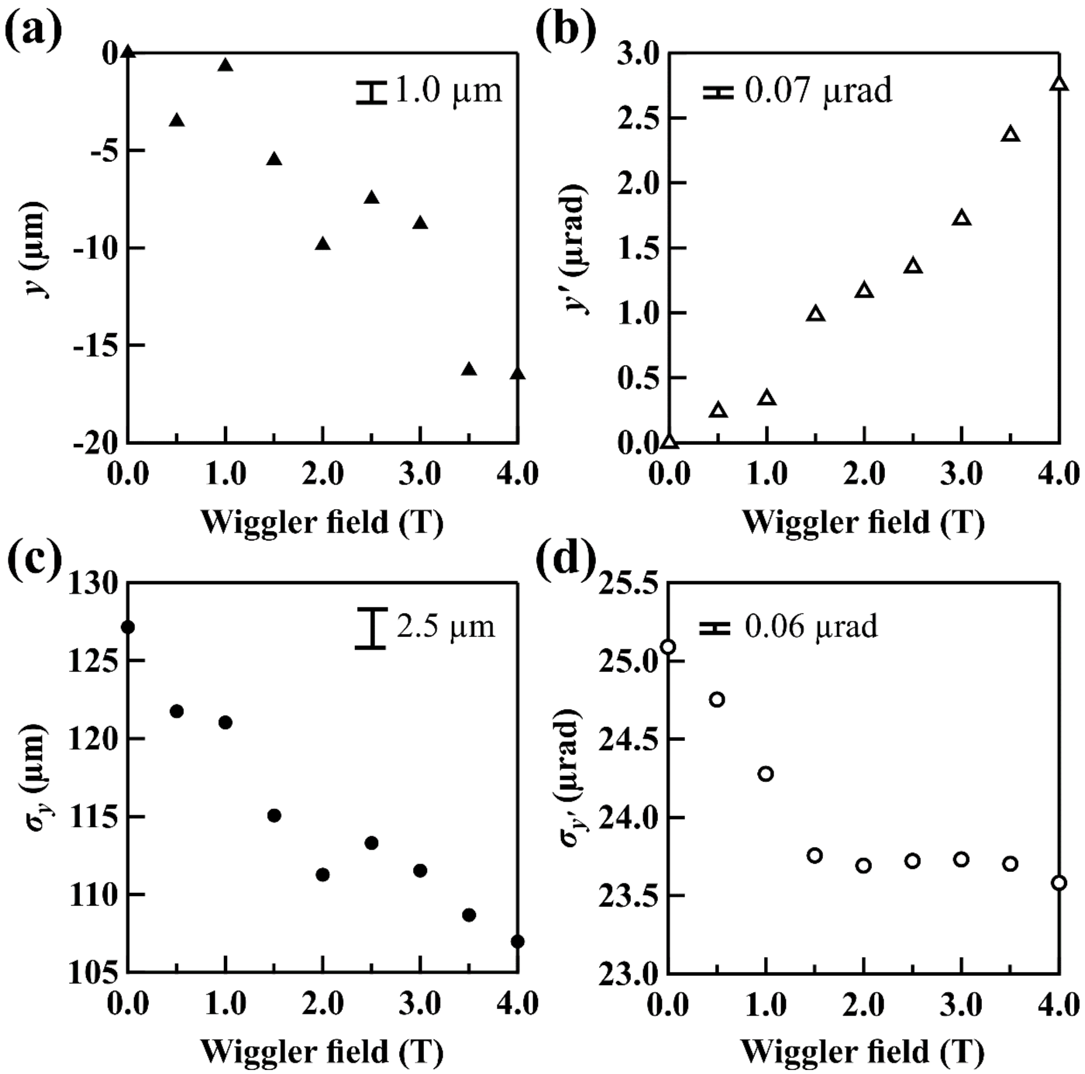

Figure 4- 6 Extracted (a) y, (b) y', (c) σ_y, and (d) σ_y' at the BMIT bending magnet as a function of the magnetic field of the BMIT wiggler. The error bars are the standard deviation of 8 measurements of 3 s data

4.4.3 Effects due to changes in a wiggler field

The ps-BPM system can provide direct measurements of source parameters, which is a promising tool for machine studies. The next example looks at the effects of the BMIT wiggler on the BM source as the superconducting wiggler field was changed. The experiment was performed at the Iodine K-edge (33.169 keV) by the Si (220) DCM at the beamline. The iodine filter projected concentration was 60 mg·cm^{-2}. BM source parameters were measured at different magnetic fields of the BMIT wiggler.

The extracted electron source position, angular position, size, and divergence are shown in Figure 4- 6 as a function of the wiggler field. All results are an average of 24 s. Varying the magnetic field of the wiggler alters the tune of the electron beam lattice which changes source parameters at the BM location. The electron beam position and angle shift slightly as the wiggler field changes as shown in Figure 4- 6 a and b, respectively. Figure 4- 6 c shows a continuous reduction in the BM source size as the wiggler field increases. On the other hand, the source divergence decreases at the beginning and reaches its minimum after the wiggler field raises above 2T as shown in Figure 4- 6 d. Note that the results here are to show the sensitivity of the ps-BPM system, which are demonstrated by the clear detection of relative changes in all four quantities as shown in Figure 4- 6. The absolute electron source sizes in this study are different from the ones in Figure 4- 3 because they were measured at different time with different electron beam lattice parameters.

4.5 CONLUSION

We have shown how to use the ps-BPM system to characterize source properties. The capability of monitoring source position, angular position, size, and divergence simultaneously is the unique feature of the ps-BPM monitor. Combining the time and frequency domain studies, the monitor can provide more systematic information about the source and the beamline.

The system was used during (1) normal operations where beam motions and size variations were monitored, (2) changing the monochromator type to investigate sources of motions, and (3) while an insertion device field was changed to assess the impact on electron beam motion and source size. In all instances, the system demonstrated its ability to provide useful information which is not possible by other means.

4.6 ACKNOWLEDGEMENTS

The authors acknowledge the financial support of Natural Sciences and Engineering Research Council of Canada (NSERC) Discovery Grant, Canadian Institutes of Health Research (CIHR) Team Grant – Synchrotron Medical Imaging, CIHR Training Grant - Training in Health Research Using Synchrotron Techniques, Canada Research Chair Program, Saskatchewan Health Research Foundation Team Grant and the University of Saskatchewan. The research described in this paper was performed at the Canadian Light Source, which is funded by the Canada Foundation for Innovation, NSERC, the National Research Council Canada, CIHR, the Government of Saskatchewan, Western Economic Diversification Canada, and the University of Saskatchewan. This work was also supported by the U.S. Department of Energy, Office of Basic Energy Sciences, under Contract No. DE-AC02-06CH11357.

4.7 REFERENCES

1. P. F. Tavares, S. C. Leemann, M. Sjostrom, and A. Andersson, "The MAX IV storage ring project," Journal of Synchrotron Radiation, vol. 21, pp. 862-877, 2014.
2. M. Eriksson, J. F. van der Veen, and C. Quitmann, "Diffraction-limited storage rings - a window to the science of tomorrow," Journal of Synchrotron Radiation, vol. 21, pp. 837-842, 2014.
3. P. Elleaume, C. Fortgang, C. Penel, and E. Tarazona, "Measuring Beam Sizes and Ultra‐Small Electron Emittances Using an X‐ray Pinhole Camera," Journal of synchrotron radiation, vol. 2, pp. 209-214, 1995.
4. C. Thomas, G. Rehm, I. Martin, and R. Bartolini, "X-ray pinhole camera resolution and emittance measurement," Physical Review Special Topics-Accelerators and Beams, vol. 13, p. 022805, 2010.
5. T. Renner, H. Padmore, and R. Keller, "Design and performance of the ALS diagnostic beamline," Review of Scientific Instruments, vol. 67, pp. 3368-3368, 1996.

6. T. Weitkamp, O. Chubar, M. Drakopoulos, I. Snigireva, A. Snigirev, C. Schroer, et al., "Electron Beam Size and Profile Measurements With Refractive X-Ray Lenses," in Proceedings of EPAC 2000, 2000, pp. 1824-1826.

7. K. Iida, N. Nakamura, H. Sakai, K. Shinoe, H. Takaki, M. Fujisawa, et al., "Measurement of an electron-beam size with a beam profile monitor using Fresnel zone plates," Nuclear Instruments and Methods in Physics Research Section A: Accelerators, Spectrometers, Detectors and Associated Equipment, vol. 506, pp. 41-49, 2003/06/21/ 2003.

8. S. Takano, M. Masaki, and H. Ohkuma, "X-ray imaging of a small electron beam in a low-emittance synchrotron light source," Nuclear Instruments and Methods in Physics Research Section A: Accelerators, Spectrometers, Detectors and Associated Equipment, vol. 556, pp. 357-370, 2006/01/01/ 2006.

9. T. Mitsuhashi, Beam Measurement: Proceedings of the Joint US-CERN-Japan-Russia School on Particle Accelerators, Montreux, and CERN, Switzerland: World Scientific Publishing Company, 1999.

10. T. Naito and T. Mitsuhashi, "Very small beam-size measurement by a reflective synchrotron radiation interferometer," Physical Review Special Topics-Accelerators and Beams, vol. 9, p. 122802, 2006.

11. J. Corbett, X. Huang, C. Li, T. Mitsuhashi, J. Wu, Y. Xu, et al., "Transverse Beam Profiling and Vertical Emittance Control with a Double-Slit Stellar Interferometer," in 5th Int. Beam Instrumentation Conf.(IBIC'16), Barcelona, Spain, Sept. 13-18, 2016, 2017, pp. 237-240.

12. J. P. Guigay, S. Zabler, P. Cloetens, C. David, R. Mokso, and M. Schlenker, "The partial Talbot effect and its use in measuring the coherence of synchrotron X ‐ rays," Journal of synchrotron radiation, vol. 11, pp. 476-482, 2004.

13. X. Shi, S. Marathe, M. J. Wojcik, N. G. Kujala, A. T. Macrander, and L. Assoufid, "Circular grating interferometer for mapping transverse coherence area of X-ray beams," Applied Physics Letters, vol. 105, p. 041116, 2014.

14. Å. Andersson, M. Böge, A. Lüdeke, V. Schlott, and A. Streun, "Determination of a small vertical electron beam profile and emittance at the Swiss Light Source," Nuclear Instruments and Methods in Physics Research Section A: Accelerators, Spectrometers, Detectors and Associated Equipment, vol. 591, pp. 437-446, 2008.

15. N. Samadi, B. Bassey, M. Martinson, G. Belev, L. Dallin, M. de Jong, et al., "A phase-space beam position monitor for synchrotron radiation," J Synchrotron Radiat, vol. 22, pp. 946-55, Jul 2015.

16. N. Samadi, X. Shi, L. Dallin, and D. Chapman, "A Real Time Phase-Space Beam Emittance Monitoring System," Journal of Synchrotron Radiation, p. Accepted 2019.

17. Y. A. Babanov, A. V. Ryazhkin, A. F. Sidorenko, and L. A. Blaginina, "Correcting an experimental absorption spectrum for the core level width," Journal of Structural Chemistry, vol. 39, pp. 833-838, November 01 1998.

18. W. H. Zachariasen, "A General Theory of X-Ray Diffraction in Crystals," Acta Crystallographica, vol. 23, pp. 558-+, 1967.

19. J. Schwinger, "On the classical radiation of accelerated electrons," Physical review, vol. 75, p. 1912, 1949.

20. T. W. Wysokinski, D. Chapman, G. Adams, M. Renier, P. Suortti, and W. Thomlinson, "Beamlines of the Biomedical Imaging and Therapy Facility at the Canadian Light Source - Part 2," Journal of Physics: Conference Series, vol. 425 Part 7, 2013.

21. T. W. Wysokinski, D. Chapman, G. Adams, M. Renier, P. Suortti, and W. Thomlinson, "Beamlines of the biomedical imaging and therapy facility at the Canadian light source—Part 1," Nuclear Instruments and Methods in Physics Research Section A: Accelerators, Spectrometers, Detectors and Associated Equipment, vol. 582, pp. 73-76, 2007.

22. T. W. Wysokinski, D. Chapman, G. Adams, M. Renier, P. Suortti, and W. Thomlinson, "Beamlines of the biomedical imaging and therapy facility at the Canadian light source - part 3," Nuclear Instruments & Methods in Physics Research Section a-Accelerators Spectrometers Detectors and Associated Equipment, vol. 775, pp. 1-4, Mar 1 2015.

23. L. Rebuffi and M. Sanchez del Rio, "ShadowOui: a new visual environment for X-ray optics and synchrotron beamline simulations," Journal of Synchrotron Radiation, vol. 23, pp. 1357-1367, 2016.

24. L. Rebuffi and M. S. d. Rio, "OASYS (OrAnge SYnchrotron Suite): an open-source graphical environment for x-ray virtual experiments," in SPIE Optical Engineering + Applications, 2017, p. 9.

CHAPTER 5

This paper was submitted in June 2019 and accepted in July 2019 for publication in the Journal of Synchrotron Radiation.

Simulations and data analysis were done by the author, Dr. Shi and Prof. Chapman and all participated in the preparation of the manuscript.

OPTIMIZATION OF A PHASE-SPACE BEAM POSITION AND SIZE MONITOR FOR LOW-EMITTANCE LIGHT SOURCES

Nazanin Samadi[a], Xianbo Shi[b]*, Dean Chapman[c&d]

[a]Physics and Engineering physics, University of Saskatchewan, 116 Science Place, Saskatoon, SK, S7N 5E2 Canada

[b]Advanced Photon Source, Argonne National Laboratory, 9700 S. Cass Ave., Lemont, Illinois, 60439, USA

[c]Canadian Light Source, 44 Innovation Boulevard, Saskatoon, SK, S7N 2V3, Canada

[d]Anatomy, Physiology and Pharmacology, University of Saskatchewan, 107 Wiggins Road, Saskatoon, SK, S7N5E5, Canada

Correspondence email: xshi@aps.anl.gov

Keywords: beam position and size monitor; phase space; diagnostics and feedback; ray-tracing simulation; diffraction-limited storage ring

Synopsis The optimization of a phase-space beam position and size monitor is carried out by ray-tracing simulation to maximize the instrumental sensitivity and resolution for diffraction-limited light sources.

5.1 ABSTRACT

The recently developed vertical phase-space beam position and size monitor (ps-BPM) system was proven to be able to measure the electron source position, angle, size and divergence simultaneously in the vertical plane at a single location of a beamline. The optimization of the ps-

BPM system is carried out by ray-tracing simulation to maximize the instrumental sensitivity and resolution. The contribution of each element, including the monochromator, K-edge filter, detector, and the source-to-detector distance, is studied. An optimized system is proposed for diffraction-limited storage rings, such as the upgrade of the Advanced Photon Source (APS). The simulation results show that the ps-BPM system can precisely monitor the source position and angle in high speed. Precise measurements of the source size and divergence will require adequate resolution with relatively longer integration time.

5.2 INTRODUCTION

The new generation synchrotron facilities are being designed and built to achieve an ultra-small emittance utilizing Multi Bend Achromat (MBA) lattices [1].

Measurements of electron beam position and size are challenging and important for the operation of these new light sources [2, 3]. The existing and planned diagnostics for measuring the source size for the MBA sources include pinhole imaging [4, 5], π-polarization imaging [6, 7], double-slit interferometry [8 – 10], and Kirkpatrick-Baez (KB) mirrors [11, 12]. Most of these systems use dedicated bending magnet (BM) beamlines. The larger size of the BM source, resulting from larger beta function, compared to other locations in the lattice allows for more precise measurements.

The pinhole camera measurement with x-rays is the simplest system, but for source sizes of less than 10 microns, it is impractical because diffraction by the pinhole complicates extracting information about the source size from the image. The double-slit interferometry system has better resolution compared to pinhole imaging because the blurring caused by the source size reduces the contrast. In this case, the contrast is a measure of the source size, which does not rely on direct imaging. These measurements are photon-hungry, and wavefront distortions caused by optical components can result in inaccurate source size measurements.

The π-polarization technique, another interference-based method, utilizes the out of orbital plane vertical (π) polarization of the BM beam and similar to the double-slit method depends on source size to reduce the intensity “null” at the midplane.

KB mirror systems use two cylindrical mirrors, one focusing the photon beam horizontally and the other one vertically onto a CCD to measure the source size. In order to beat the diffraction limit, KB mirror system must use short wavelength synchrotron radiation.

In all of these methods, the knowledge of the point spread function of the detection system is essential for the source size deconvolution. The contribution from the detector resolution has to be minimized for small source size measurements.

The ps-BPM system [13, 14] developed at Canadian Light Source (CLS) has demonstrated the ability to measure the source size and divergence as well as source position and angle in the vertical plane, at a single location and time. In this paper, we will report on the process of optimizing the ps-BPM system for ultra-small electron source size measurements and provide an example for the Advanced Photon Source Upgrade (APS-U) project [15].

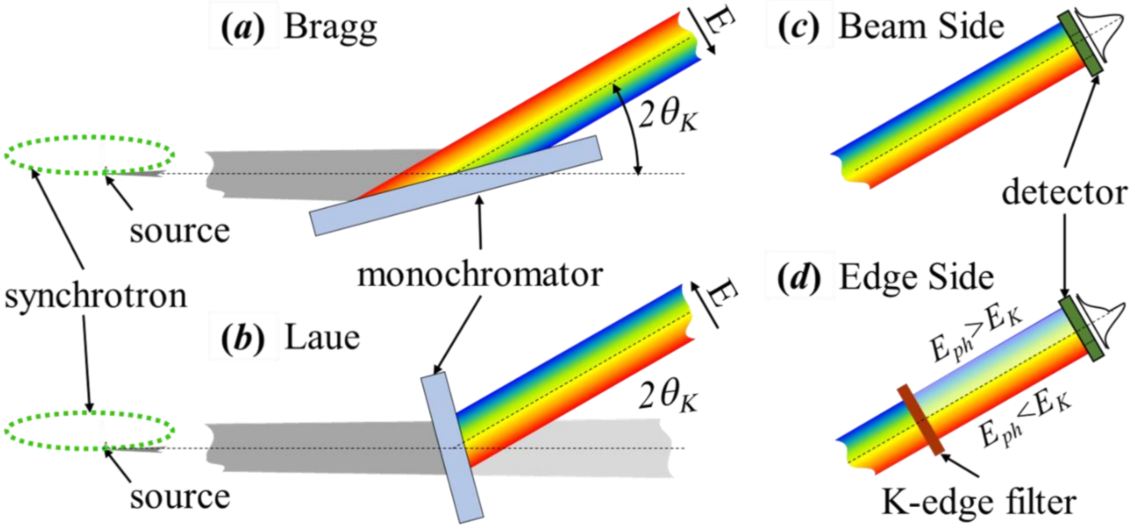

Figure 5- 1 Schematic of the ps-BPM system including a Bragg (a) or Laue (b) crystal monochromator, a K-edge filter in (d), and a detector which records both unfiltered beam side (c) and filtered edge side (d) of the beam.

5.2.1 ps-BPM system

A ps-BPM system, as shown in Figure 5- 1, contains a crystal-based monochromator, a K-edge filter, and an area detector. The monochromator is tuned to the photon energy of the K-edge of the filter element. The system utilizes the large horizontal photon fan of the BM beamline to measure simultaneously the direct beam (unfiltered beam) and the part going through the K-edge filter (filtered beam). These beams include both σ and π polarizations and polarization effect is negligible in the analysis.

The natural vertical opening angle of the photon beam [16] provides a Gaussian-type profile for the unfiltered side of the beam at photon energies well above the critical energy of the BM source. It is the central location and width of this unfiltered beam that is used in the data analysis. The photon beam opening angle also provides a range of incident angles onto the monochromator crystal. This range of angles can give an energy range about the central K-edge energy. The K-edge will introduce a step-type function through this energy range. The location and width of the K-edge are used in the analysis of the filtered data.

The vertical profiles of the filtered and unfiltered beams contain the information of the electron source position, angle, size, and divergence [13]. The position of the K-edge location in the filtered beam, y_{edge}, is a direct measure of the electron source position, $y_{eSource}$, or

$$y_{eSource} = y_{edge}. \tag{5. 1}$$

The electron source size, $\sigma_{y_{eSource}}$, can be extracted from the spatial width of the measured K-edge on the detector, σ_{edge}, by [14]

$$\sigma_{y_{eSource}} = \sqrt{\sigma_{edge}^2 - (D\sigma_{y'_{K-edge}})^2 - (D\sigma_{y'_{mono}})^2}, \tag{5. 2}$$

where D is the source-to-detector distance, $\sigma_{y'_{K-edge}}$ is the natural width of the K-edge of the filter element translated from an energy width to angular width (see section 2), and $\sigma_{y'_{mono}}$ is the angular acceptance of the monochromator [17, 18]. The electron source emission angle, $y'_{eSource}$, and divergence, $\sigma_{y'_{eSource}}$, can be obtained from the simultaneously measured unfiltered beam position, y_{beam}, and width, σ_{beam}, by

$$y'_{eSource} = \frac{1}{D}\left(y_{beam} - y_{edge}\right), \tag{5. 3}$$

and

$$\sigma_{y'_{eSource}} = \frac{1}{D}\sqrt{\sigma_{beam}^2 - \sigma_{y_{eSource}}^2 - (D\sigma_{y'_{Ph}})^2}, \tag{5. 4}$$

respectively, where $\sigma_{y'_{ph}}$ is the natural opening angle of the photon beam [16]. In the following sections, each term in Equations (5. 1) - (5. 4) will be analyzed quantitatively with numerical simulation.

5.2.2 Simulation tools and method

The system measures the beam along the direction perpendicular to the orbital plane which is also the diffraction plane of the monochromator that is typically vertical. Taking this direction, the system can be described by the propagation of the photon beam through phase-space, which includes minimally three dimensions, the energy, E, the vertical spatial coordinate, y, and the vertical angular coordinate, y'. To describe the system in sufficient resolution, each dimension needs at least a grid size of 10^3, which gives a total matrix size of 10^9. To reduce the computation effort, Monte-Carlo based geometrical ray-tracing is used for this work.

All simulations are performed using the ShadowOui program [19] in the OASYS [20] environment. In ShadowOui, each type of source and optical element is defined as an individual "widget". The BM source is simulated using the "Bending Magnet" widget, which requires input of electron source size, electron emittance ($\propto \sigma_{y_{eSource}} \cdot \sigma_{y'_{eSource}}$), and magnetic field of the BM. A BM point source (zero emittance) (PS) can be created by setting both $\sigma_{y_{eSource}}$ and $\sigma_{y'_{eSource}}$ to zero, which is used to generate the photon beam distribution representing the single electron emission or single electron point spread function from the BM. The BM source includes both horizontal (σ) and vertical (π) polarization components, however, only about 4% of the total intensity is contained in the π polarization.

The monochromators considered in this work are single crystals in the Bragg and Laue geometry. All crystals are simulated using the "Plane Crystal" widgets in ShadowOui, where the crystal Bragg angle is set to be auto-tuned to the K-edge energy, E_K, of the selected filter element.

The K-edge filter is the next optical element downstream of the monochromator. The built-in module in ShadowOui for filter absorption does not contain lifetime broadening for the K-edge spectrum, which is the main contributor to the edge width, σ_{edge}, in real measurements. Therefore,

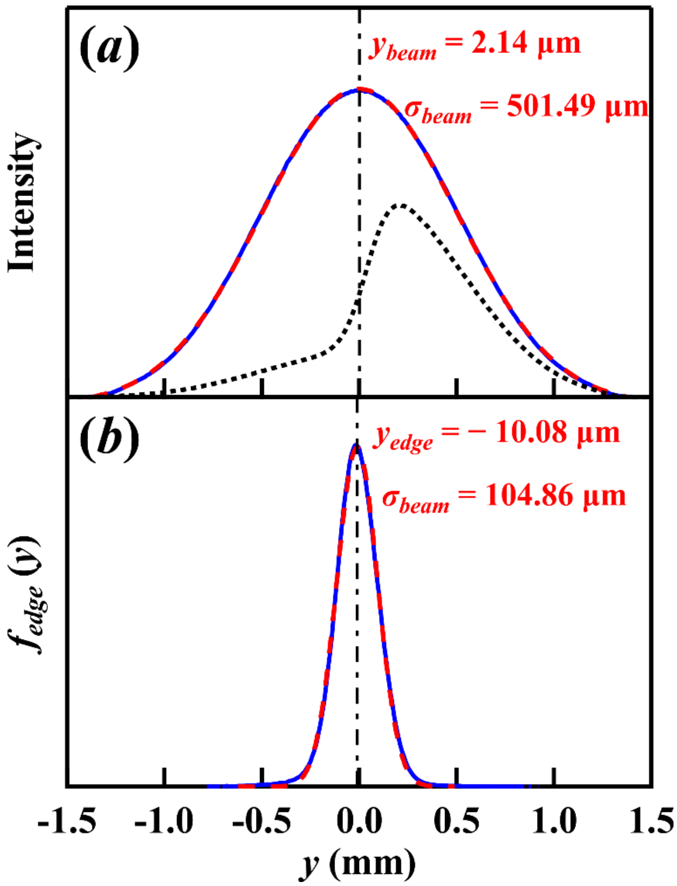

Figure 5- 2 The simulated vertical profiles of the filtered beam, $I_{filtered}(y)$, (solid curve) and the unfiltered beam, $I_0(y)$, (dotted curve), and (b) the edge profile, $f_{edge}(y)$, (solid curve) obtained from Equation (5. 6). The dashed lines in (a) and (b) are the Gaussian fitting of $I_0(y)$ and $f_{edge}(y)$ using Equations (5. 7) and (5. 8), respectively.

a dedicated Python script was made inside the OASYS environment to simulate the filter absorption by assigning to each ray an intensity scaling factor based on its photon energy and the transmission curve. The transmission through the filter is calculated by

$$T = e^{-\frac{\mu}{\rho}(E)\rho t}, \tag{5. 5}$$

where $\frac{\mu}{\rho}(E)$ is the energy dependent mass attenuation coefficient around the K-edge of the filter, ρ is the concentration and t is the effective filter thickness. The K-edge spectrum depends on the core level width, which is normally described by a Lorenz function [21]. In this work, to be consistent with the experimental results [13], a Gaussian function is used.

A typical simulation to achieve enough statistics requires 5×10^7–5×10^8 rays, which is challenging to run and store as a single simulation. Therefore, a recursive loop is implemented to accumulate results of multiple runs (typically 100-3200), each of which contains 5×10^5 rays. The vertical photon beam profiles are recorded as histograms that collect rays at the detector position. The histograms are weighted by the ray intensity which contains information on the crystal reflectivity and the filter transmission. The bin size of the histograms is a representation of the pixel size of the detector. The vertical profiles of the filtered beam, $I_{filtered}(y)$, and the unfiltered beam, $I_0(y)$, are collected and stored for post analysis (see Figure 5- 2 a).

The simulated photon beam profiles are then analyzed based on the same data analysis process developed for experimental results [14]. The edge profile, $f_{edge}(y)$, shown in Figure 5-2b, is obtained by

$$f_{edge}(y) = \frac{d\{-\ln[I_{filtered}(y)/I_0(y)]\}}{dy}. \tag{5. 6}$$

The edge profile and the unfiltered beam profile are both fitted to a Gaussian function with widths σ_{edge} and σ_{beam} and center positions, y_{edge} and y_{beam}, respectively, given by

$$I_0(y) = A_0 e^{-\frac{(y-y_{beam})^2}{2\sigma_{beam}^2}} + A_1. \tag{5. 7}$$

and

$$f_{edge}(y) = B_0 e^{-\frac{(y-y_{edge})^2}{2\sigma_{edge}^2}} + B_1. \tag{5. 8}$$

The position and angle at the electron beam source are extracted from the fitted y_{beam} and y_{edge} values using Equation 5- 1 and 5- 3, respectively. The electron beam source size is obtained by deconvolving the edge width, $\sigma_{edge,PS}$, of a zero-emittance point source from that of the BM source, $\sigma_{edge,BM}$, with a finite electron beam size, given by

$$\sigma_{y_{eSource}} = \sqrt{\sigma_{edge,BM}^2 - \sigma_{edge,PS}^2}. \tag{5. 9}$$

Comparing Equation (5. 9) with Equation (5. 2), the simulated $\sigma_{edge,PS}$ term represents the total contribution of $D\sigma_{y'_{K-edge}}$ and $D\sigma_{y'_{mono}}$. The electron beam divergence is then obtained from the photon beam widths, $\sigma_{beam,BM}$ for the BM source and $\sigma_{beam,PS}$ for the zero-emittance point source by

$$\sigma_{y'_{eSource}} = \frac{1}{D}\sqrt{\sigma_{beam,BM}^2 - \sigma_{beam,PS}^2 - \sigma_{y_{eSource}}^2}. \tag{5. 10}$$

The simulated $\sigma_{beam,PS}$ term represents $D\sigma_{y'_{ph}}$ in Equation (5. 4). The simulation error is calculated as the standard deviation of results from one hundred separate ray-tracing calculations unless otherwise specified.

5.3 OPTIMIZATION PROCESS

The optimization process involves aspects of the system that determine its ability to best measure source properties. These factors include the monochromator, K-edge filter, detector characteristics, and arrangement of these components (measurement geometry).

Two cases are considered: a bending magnet at the CLS and a bending magnet for the APS-U.

For the CLS, the simulation study is for a 1.354 T BM and an electron beam with $\sigma_{y_{eSource}}$ = 52.7 µm and $\sigma_{y'_{eSource}}$ = 6.35 µrad [22]. Unless specified, all simulations were performed with a monochromator tuned to the Barium K-edge energy (37.441 keV), a 35 mg·cm^{-2} barium K-edge filter, and a source-to-detector distance of D = 10 m.

5.3.1 Monochromator

The monochromator is one of the most critical components of a ps-BPM system. The effect of the monochromator and the choice of the K-edge filter are closely related to each other through the angle-energy dispersion from Bragg's law. The dispersion effect of the monochromator crystal projects the absorption edge energy width, $\sigma_{E_{K-edge}}$, into an angular width, $\sigma_{y'_{K-edge}}$, (measured by the spatial width on the detector at distance D) through the relationship

$$\sigma_{y'_{K-edge}} = \frac{\tan\theta_K}{E_K}\sigma_{E_{K-edge}}, \qquad (5.\ 11)$$

where θ_K is the Bragg angle of the monochromator crystal at the filter K-edge energy, E_K. In general, to achieve small $\sigma_{y'_{K-edge}}$ requires a filter with small $\sigma_{E_{K-edge}}$, a high K-edge energy, and a small Bragg angle. This section and section 2.2 below show in detail how these terms contribute to the measurement.

There are several choices for the crystal material, reflection geometry and choice of lattice planes that will now be considered.

5.3.1.1 Crystal material and geometry

Single crystal materials are considered for the monochromator. High quality semiconductor crystals are commonly available as a consequence of the semiconductor industry drive to improve device performance. Dynamical theory [18] can be used to describe the diffraction properties of such crystals. Silicon is the most common monochromator crystal used for x-ray beamlines because of its availability, degree of perfection, and ability to handle synchrotron radiation heat loading.

The diffraction geometry from crystals falls into two broad categories. The reflection or Bragg geometry has lattice planes mostly parallel to the crystal's surface; X-rays impinge upon

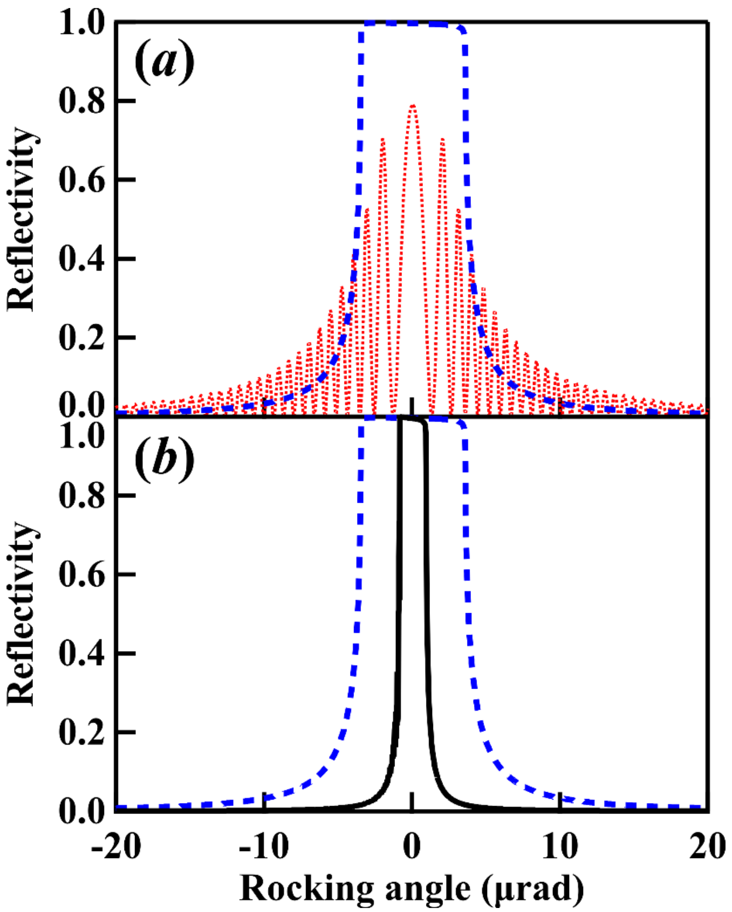

Figure 5- 3 Diffraction profiles of the Si (111) reflection in the Bragg (dashed line) and Laue (dotted line) geometry and the Si (440) Bragg reflection (solid line).

and diffract out of the same surface. In transmission or Laue geometry the lattice planes are mostly perpendicular to the crystal surface; x-rays impinge upon one surface and exit through another by diffracting through the crystal.

The Laue geometry has two practical advantages over Bragg because it allows a smaller footprint (a smaller crystal) and reduced thermal deformation from the photon beam heat load. Nevertheless, based on the diffraction profiles (see Figure 5- 3a) calculated using the XCRYSTAL module [23] in XOP [24], Bragg geometry is preferred owing to the higher reflectivity and narrower bandwidth compared to Laue geometry.

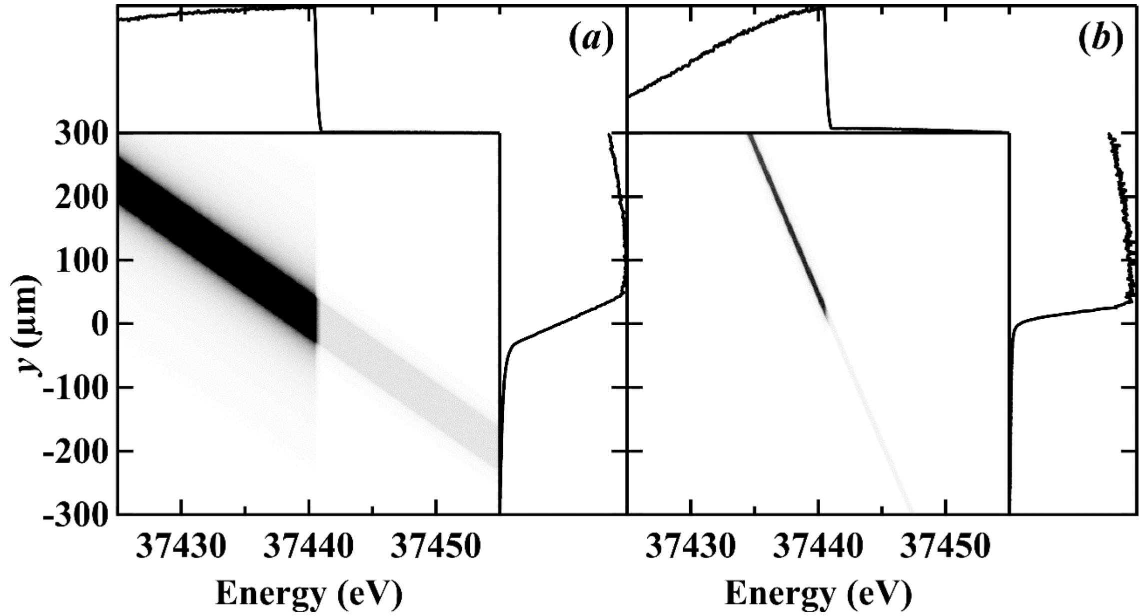

Figure 5- 4 Simulated DuMond diagrams using a zero-emittance BM source that is diffracted by (a) a Si (111) and (b) a Si (440) crystal, and filtered by a barium filter with a sharp K-edge ($\sigma_{E_{K-edge}}$ = 0).

Intensive efforts are being dedicated to the studies of crystal quality and thermal mechanical design of monochromators, which are not in the scope of this work. We limit the following discussions to single Bragg silicon crystals and focus on the optical optimization of the ps-BPM system.

5.3.1.2 Crystal lattice planes

The intrinsic angular bandwidth of a monochromator, $\sigma_{y'_{mono}}$, can be modelled using standard dynamical theory [18]. Reflection from high-indices planes [e.g., Si (440)] has smaller angular bandwidth as shown in Figure 5- 3b. This effect can be clearly seen in the DuMond diagrams [25] shown in Figure 5- 4, where a zero-emittance BM source is monochromatized by a Si (111) crystal (Figure 5- 4a) and a Si (440) crystal (Figure 5- 4b) to the barium K-edge energy. Assuming the photon beam is absorbed by a barium filter with a sharp edge ($\sigma_{E_{K-edge}}$ = 0), the intrinsic bandwidth of the crystal is spatially projected onto the detector plane (the y axis in Figure 5- 4).

The Si (440) reflection contributes to a much smaller edge width, yet gives a larger Bragg angle (steeper y vs. energy slope in Figure 5- 4b). This has the effect to limit the energy range the monochromator will cover with the photon beam divergence from the source. A limited energy range is not ideal when the filter edge width, $\sigma_{E_{K-edge}}$, is non-zero based on Equation (5. 11). Table 5- 1 shows the width of the barium K-edge in angle, $\sigma_{y'_{K-edge}}$, with different crystal reflections. For the same energy edge width ($\sigma_{E_{K-edge}}$ = 5.6 eV, or a FWHM of 13.2 eV assuming a Gaussian distribution) [21], a crystal with lower reflection indices is preferred.

Table 5- 1 Barium K-edge width, $\sigma_{E_{K-edge}}$, and the equivalent angular width, $\sigma_{y'_{K-edge}}$, calculated using Equation (5. 11)

$\boldsymbol{E_K}$ **= 37.441 keV**	**Si (111)**	**Si (220)**	**Si (311)**	**Si (440)**
$\boldsymbol{\theta_K}$ **(°)**	3.027	4.947	5.804	9.931
$\boldsymbol{\sigma_{E_{K-edge}}}$ **(eV)**	5.6	5.6	5.6	5.6
$\boldsymbol{\sigma_{y'_{K-edge}}}$ **(µrad)**	7.9	13.0	15.2	26.2

5.3.2 K-edge filter

The choice of the K-edge filter determines the energy to be selected by the monochromator. Also, the K-edge width will affect the ability to determine the source size [see Equation 5- 2)] as it needs to be accounted for in the overall edge width measurement. Since the monochromator and energy will determine the flux from the source, the ability to accurately determine the center and width of the distribution will rely on the statistical fitting of the vertical profile of the beam. The same applies to the K-edge filter where a statistical fit to the edge location and width is performed. The flux for those measurements will depend upon the K-edge filter element attenuation ($\frac{\mu}{\rho}$),

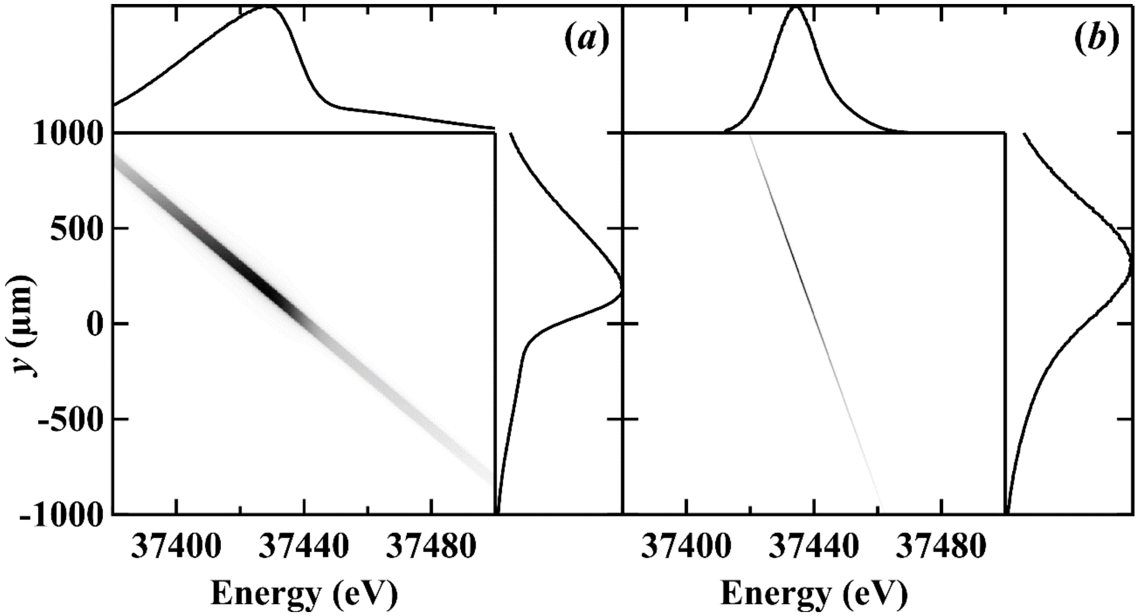

Figure 5- 5 Simulated DuMond diagrams using a zero-emittance BM source that is diffracted by (a) a Si (111) and (b) a Si (440) crystal, and filtered by a barium filter with a finite K-edge width ($\sigma_{E_{K-edge}}$ = 5.6 eV).

concentration (ρ) and thickness (t) – see Equation 5- 5. The product of concentration and thickness is commonly referred to as the projected concentration (mass per area) of the filter.

5.3.2.1 K-edge choice

The natural energy width of the K-edge of an element is dominated by the lifetime of the electron-hole in the K shell. Both the K-edge energy and the edge width increase with the atomic number [26]. As described in section 2.1, the K-edge selection must be considered along with the selection of the monochromator crystal. Figure 5- 5 shows the simulated vertical photon beam profiles indicating the edge widths that contain contributions from both the monochromator and the filter K-edge. Even though the crystal bandwidth is smaller for Si (440) crystal (Figure 5- 4), the total edge width is spatially larger in y (see. Figure 5- 5) due to the increased energy dispersion of the (440) compared to the (111) reflection.

Quantitatively, the total contribution from both the monochromator and the K-edge filter add in quadrature as

$$\sigma_{y'_{total}} = \sqrt{\sigma^2_{y'_{K-edge}} + \sigma^2_{y'_{mono}}}. \tag{5. 12}$$

The calculated $\sigma_{y'_{mono}}$, $\sigma_{y'_{K-edge}}$, and $\sigma_{y'_{total}}$ values for different filter elements and crystal reflections are summarized in Table 5- 2, where $\sigma_{y'_{mono}}$ is the fitted Gaussian width of the diffraction profile calculated using XOP [24], and $\sigma_{y'_{K-edge}}$ is calculated using Equation (5. 11) with $\sigma_{E_{K-edge}}$ extracted from Figure 5- 1 in Ref [21]. As the element atomic number goes up, the total contribution from the K-edge width and monochromator width becomes smaller, which implies a better sensitivity for detecting the electron source size based on Equation (5. 2). Since, the total contribution is mostly dominated by the K-edge width, the bandwidth of the monochromator has relatively less effect. Therefore, crystals with lower reflection indices [i.e., Si (111)] are preferred because of the smaller Bragg angle. Table 5- 2 also shows that the reduction of the total width is not that dramatic when going to a higher atomic number than iodine. Considering that most of the BM sources have critical energies much less than 30 keV, going to a higher energy leads to a rapid reduction in flux as well. One should therefore choose as high an energy as possible while maintaining sufficient flux.

Table 5- 2 The angular width of the monochromator, $\sigma_{y'_{mono}}$, the projected filter K-edge width, $\sigma_{y'_{K-edge}}$, and their total contribution, $\sigma_{y'_{total}}$, calculated using Equation (5. 12).

	E_K (keV)	θ_K (°)	$\sigma_{y'_{mono}}$ (μrad)	$\sigma_{y'_{K-edge}}$ (μrad)	$\sigma_{y'_{total}}$ (μrad)
			Si (111)		
Cu	8.979	12.72	13.4	13.3	18.9
Mo	20.000	5.674	5.8	9.2	10.8
Ag	25.514	4.445	4.5	8.6	9.7
I	33.169	3.418	3.5	8.0	8.7
Ba	37.441	3.027	3.1	7.9	8.5
			Si (220)		
Cu	8.979	21.08	10.1	22.8	24.9
Mo	20.000	9.291	4.2	15.1	15.6
Ag	25.514	7.270	3.3	14.1	14.5
I	33.169	5.586	2.5	13.0	13.3
Ba	37.441	4.947	2.2	13.0	13.1
			Si (440)		
Cu	8.979	45.99	4.8	61.2	61.4
Mo	20.000	18.84	1.5	31.4	31.5
Ag	25.514	14.66	1.2	29.0	29.0
I	33.169	11.23	0.9	26.4	26.4
Ba	37.441	9.931	0.8	26.2	26.2

5.3.2.2 Filter concentration

The choice of filter concentration and thickness (projected concentration) will affect the sensitivity and accuracy of the source size measurement. Figure 5- 6 shows the extracted (a) edge jumps, (b) edge profiles, and (c) source sizes calculated with different Ba filter concentrations. When the filter projected concentration is low (e.g., 7 mg·cm^{-2}), the absorption edge contrast is low, which gives a lower intensity edge profile and higher noise level. Therefore, the extracted source sizes have larger uncertainties, shown as the error bar in Figure 5- 6c. On the other hand, when the filter projected concentration is too high (e.g., 140 mg·cm^{-2}), the filter absorbs most of the light on the high energy side (negative y value side) of the spectrum, which tends to broaden the fitted edge width and thus gives a larger source size. The relative fitting error is also large in high filter projected concentration cases. As a result, the best filter projected concentration for Ba is around 35 mg·cm^{-2}. In practice, it is easy to optimize the filter projected concentration experimentally by analyzing the measurement error and accuracy as demonstrated by the simulation.

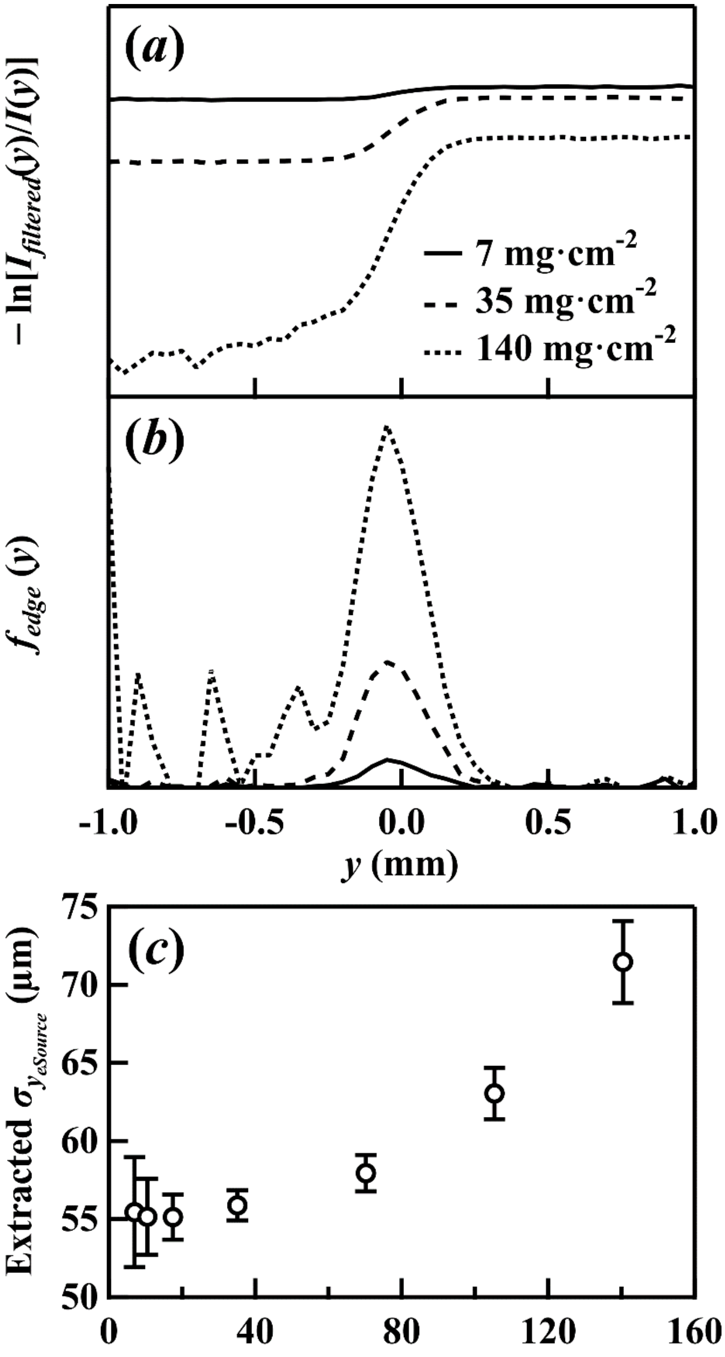

Figure 5- 6 Simulated barium K-edge steps (a) and K-edge profiles (b), and the extracted source sizes (c) with different filter projected concentrations.

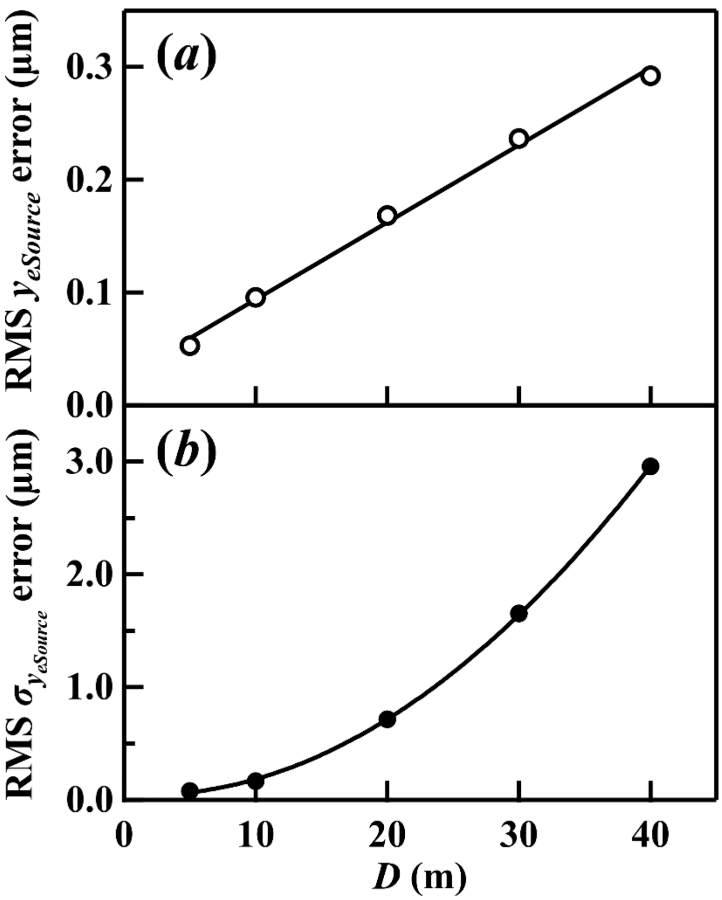

Figure 5- 7 RMS error of the simulated electron source position (a) and size (b) as a function of the source-to-detector distance, D.

5.3.3 Geometry

The basic geometry of the ps-BPM system is shown in Figure 5- 1. Other than the obvious arrangement where the system elements must intercept the incident and diffracted beams, the only relevant distance is the source-to-detector distance, D, as indicated in Equations (5. 1)-(5. 4).

The source-to-detector distance, D, must be optimized to maximize the sensitivity of the ps-BPM system. Simulation was carried out using the parameters described in section 2 with variable distances, D. The standard deviation (RMS error) of the simulated electron source size and position, which is a good measure of the sensitivity of the ps-BPM system, is plotted as a function of D in Figure 5- 7a and 5- 7b, respectively. The sensitivity for detecting the source position, y, is linearly related to the choice of D (see Figure 5- 7a). More importantly, the sensitivity for measuring the source size is inversely proportional to D^2 (see Figure 5- 7b).

It is therefore beneficial to reduce D to optimize sensitivity of the ps-BPM system. Because of the physical space limitation in a typical beamline, a distance of 10 m would be a reasonable choice for existing or planned BM beamlines that are dedicated to source diagnostics. Another concern for a short distance is that the quadratic increase of the incident power density will increase the thermal deformation on the monochromator crystals, which will degrade the accuracy of the size and angle measurements. In that case, an aggressive cooling scheme will be required.

5.3.4 Detector

The determination of the unfiltered beam location and width as well as the filtered beam K-edge location and width relies on curve fitting to the measured $I_0(y)$ and $f_{edge}(y)$ profiles using Equations (5. 7) and (5. 8), respectively. The edge width is normally in the range of a few tens of microradians as shown in Table 5- 2. There must also be enough spatial resolution across the edge width to ensure an accurate fitting. Figure 5- 8 shows the simulated source size and divergence as a function of the pixel size (bin size of the histograms) with the total flux (number of rays) kept constant. A pixel size of a few tens of microns is adequate to ensure the accuracy of the source size and divergence measurements. Previous experiments [14] show that a detector with 100 μm pixel size is sufficient to measure third-generation synchrotron source sizes. Overall, the accuracy of the curve fitting procedure is more sensitive to the integrated flux than to the pixel size of the detector.

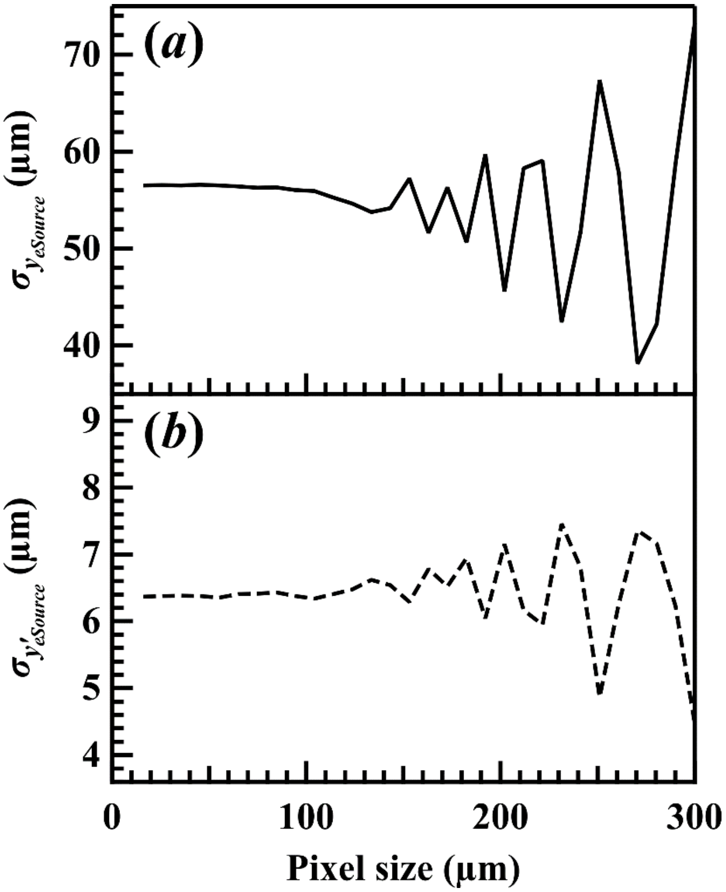

Figure 5- 8 Extracted electron source size (a) and divergence (b) as a function of detector pixel size (bin size of the simulated histograms).

The next-generation synchrotrons have the source size and divergence one order of magnitude smaller. A similar study shows that a pixel size of 10 µm is expected to be sufficient for the APS-U source assuming perfect detectors. However, the noise level (dark noise and others) on the detector will affect the curve fitting results and reduce the measurement sensitivity. The smallest measurable size of the ps-BPM system will be limited by the flux and detector resolution and noise level, which needs further study.

5.4 EXAMPLE OF A PS-BPM SYSTEM FOR APS-U

Based on all the above studies, an optimized configuration is proposed for the low-emittance APS-U project. The APS-U will have 42 pm·rad natural emittance [15]. Simulations were performed with the source parameters at the M3 bending magnet with $\sigma_{y_{eSource}}$ = 4.9 µm and $\sigma_{y'_{eSource}}$ = 2.8 µrad, a single-Bragg Si (111) monochromator tuned to the barium K-edge energy (37.441 keV), a 35 mg·cm^{-2} barium filter, a source-to-detector distance of D = 10 m, and a detector pixel size of 10 µm.

Using the simulation procedure described in section 1.2, the ability of the ps-BPM to measure the source properties was analyzed. Figure 5- 9 shows the predicted output source properties as a function of input values that varied relatively to their nominal values by as low as 5%. The source position and angular position were simulated with 5×10^{7} rays and obtained from Equations (5. 1) & (5. 8), and Equations (5. 3) & (5. 7), respectively. The source size and divergence were studied with 5×10^{8} rays and extracted using Equations (5. 9) and (5. 10), respectively.

The ps-BPM system has excellent ability to measure the source position and angular position as shown in Figure 5- 9a and 5- 9b. The measurement of source position and angular position is fast and considered real time. The source size and divergence can be extracted at the same time, which is one of the main features of the ps-BPM system. The sensitivity to the source size variation is about 10% of the nominal source size in these calculations due to the limited statistics. The source size measurement is the most photon hungry component of the system. In real measurements, increasing the acquisition time will improve the sensitivity, but with limited measurement speed.

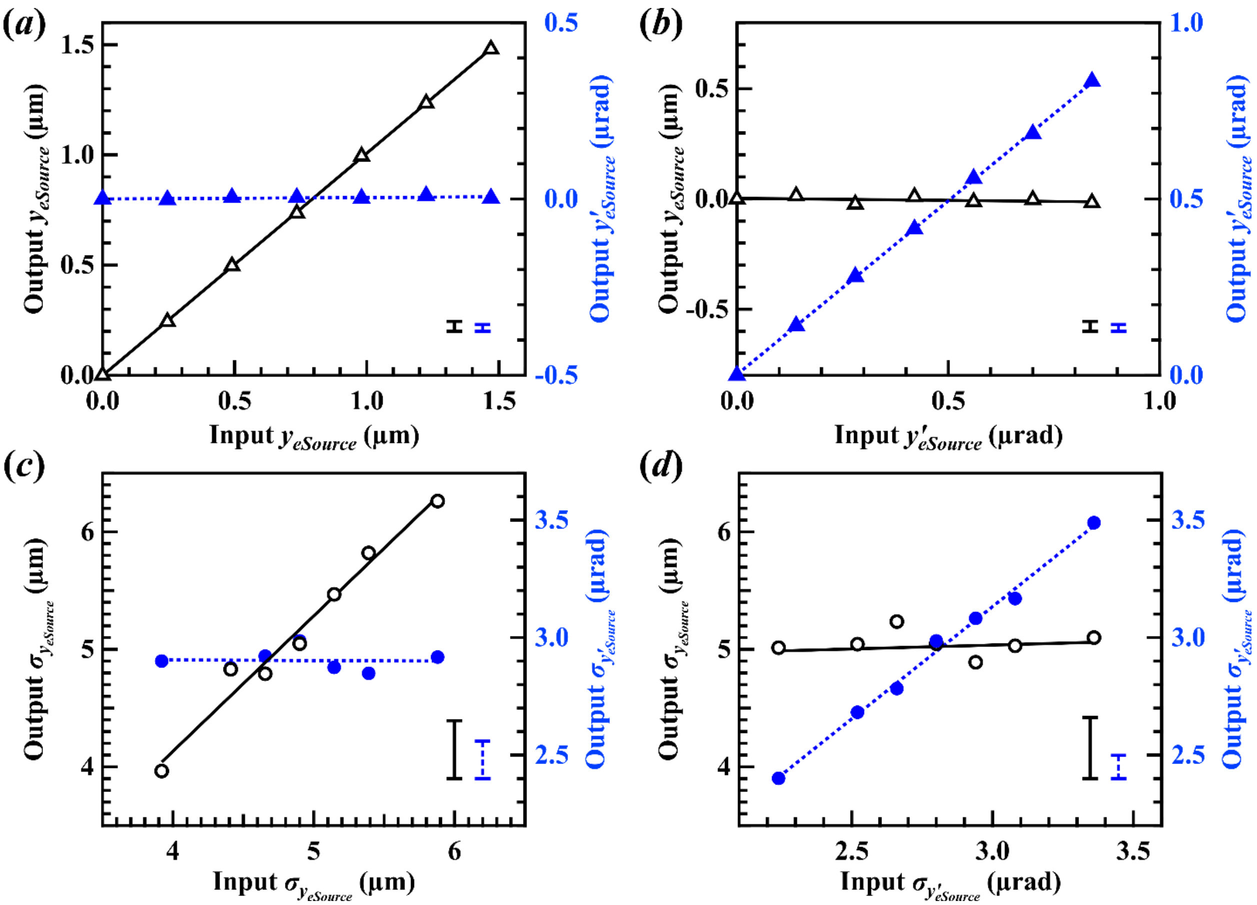

Figure 5- 9 Predicted output electron source position (open triangles) and angular position (closed triangles) from different input values of position (a) and angular position (b). Predicted output electron source size (circles) and divergence (bullets) from different input values of size (c) and divergence (d).

The sensitivity of the ps-BPM system is flux driven, but non-linearly. The required flux level can be only estimated with the comparison of experimental and simulation results. One feature of Shadow ray-tracing is that rays can have fractional intensities to account for the crystal reflectivity and filter absorption. Therefore, a single ray can represent a large number of photons. From the previous studies [14], simulation with 1×10^{7} rays gives the same sensitivity as the measurement of source size performed with a flux level of 1.2×10^{10} photons Hmrad^{-1} (H means horizontal). To achieve the sensitivity shown in Figure 5- 9c, simulation with 5×10^{8} rays indicates that a flux level of 5.9×10^{11} photons Hmrad^{-1} is needed for measuring the APS-U source size.

Considering a Si (111) Bragg crystal monochromator with no filter, this requires a minimum of 1.5 second exposure time.

5.5 CONLUSION

The ps-BPM system can precisely measure electron beam source position and angle, which are relative to the K-edge location in the filtered side of the photon beam as well as the central location of the unfiltered beam. The system can also provide accurate measurements of the electron source size and divergence from knowledge of the K-edge width and the full photon beam width. The simultaneous measurement of all four source properties in the vertical plane is the unique feature of the ps-BPM system. In principle, the system can also be used to measure the source position and size in the horizontal plane, but a separate horizontally deflecting monochromator will be required.

Factors that affect the sensitivity and resolution of the system include the choice of monochromator, K-edge filter, geometry of the system and detector. The optimized configuration contains low-index crystal reflections, a high energy K-edge filter, and a relatively small source-to-detector distance. The filter element concentration must be selected to ensure enough absorption contrast while maintaining a reasonable transmission on the high energy side of the K-edge. Compared to other systems, the ps-BPM monitor has less demanding requirements on detector resolution, which makes it capable of high-speed measurements.

It is also worth to point out that the ps-BPM system can measure a wide size range. The larger the source size, the easier (or faster) it can be measured, as long as the source size contribution ($\sigma_{y_{eSource}}/D$) is smaller than the natural opening angle of the photon beam.

A single crystal monochromator may generate Compton scatter at the detector location which reduces signal contrast. To achieve higher sensitivity the use of a two-crystal monochromator should be considered. Another concern is fluorescence from the K-edge filter some of which may also provide background in the detector. Other considerations for a practical system will include mechanical stability and thermal management of the monochromator.

Simulations validated by measurement show that the ps-BPM system is suitable for next-generation light sources. An optimized system for the APS-U source was presented as an example to demonstrate the performance. The source position and angular motion can be monitored with high precision and in high speed. While the source size measurement is photon-hungry, which creates a trade-off between measurement speed and resolution. Because of the relatively simple configuration of the ps-BPM monitor, it can coexist and operate in parallel with other systems at the same beamline.

5.6 ACKNOWLEDGEMENTS

Acknowledgements The authors would like to thank Dr. Luca Rebuffi (Argonne National Laboratory) for the OASYS support and Dr. Les Dallin (Canadian Light Source) for the invaluable discussions.

This work was supported by the U.S. Department of Energy, Office of Basic Energy Sciences, under Contract No. DE-AC02-06CH11357, Natural Sciences and Engineering Research Council of Canada (NSERC) Discovery Grant, Canadian Institutes of Health Research (CIHR) Team Grant – Synchrotron Medical Imaging, CIHR Training Grant - Training in Health Research Using Synchrotron Techniques, Canada Research Chair Program, Saskatchewan Health Research Foundation Team Grant and the University of Saskatchewan.

5.7 REFERENCES

1. D. Einfeld, M. Plesko, and J. Schaper, “First multi-bend achromat lattice consideration,” J. Synchrotron Radiat., vol. 21, no. 5, pp. 856–861, 2014.

2. M. Eriksson, J. F. Van Der Veen, and C. Quitmann, “Diffraction-limited storage rings-A window to the science of tomorrow,” J. Synchrotron Radiat., vol. 21, no. 5, pp. 837–842, 2014.

3. P. F. Tavares, S. C. Leemann, M. Sjöström, and A. Andersson, “The MAX IV storage ring project.,” J. Synchrotron Radiat., vol. 21, no. Pt 5, pp. 862–77, 2014.

4. P. Elleaume, C. Fortgang, C. Penel, and E. Tarazona, “Measuring Beam Sizes and Ultra-Small Electron Emittances Using an X-ray Pinhole Camera,” J. Synchrotron Radiat., vol. 2, no. 5, pp. 209–214, 1995.

5. C. Thomas, G. Rehm, I. Martin, and R. Bartolini, “X-ray pinhole camera resolution and emittance measurement,” Phys. Rev. Spec. Top. - Accel. Beams, vol. 13, no. 2, pp. 1–11, 2010.

6. Å. Andersson, M. Böge, A. Lüdeke, V. Schlott, and A. Streun, “Determination of a small vertical electron beam profile and emittance at the Swiss Light Source,” Nucl. Instrum. Methods Phys. Res. A, vol. 591, no. 3, pp. 437–446, 2008.

7. J. Breunlin and Å. Andersson, “Emittance diagnostics at the MAX IV 3 GeV storage ring,” Proc. 7th Int. Part. Accel. Conf., pp. 2908–2910, 2016.

8. T. Mitsuhashi, “Beam Measurement-Proceedings Of The Joint Us-cern-japan-russia School On Particle Accelerators,” in Beam measurement: Proceedings, Joint US-CERN-Japan-Russia School on Particle Accelerators, Montreux and Geneva: World Scientific Publishing Company, 1999, pp. 399–427.

9. T. Naito and T. Mitsuhashi, “Very small beam-size measurement by a reflective synchrotron radiation interferometer,” Phys. Rev. Spec. Top. - Accel. Beams, vol. 9, no. 12, pp. 1–7, 2006.

10. J. Corbett et al., “Transverse beam profiling and vertical emittance control with a double-slit stellar interferometer,” Proc. IBIC2016, pp. 236–239, 2017.

11. T. R. Renner, H. A. Padmore, and R. Keller, “Design and performance of the ALS diagnostic beamline,” Rev. Sci. Instrum., vol. 67, no. 9, p. 3368, 1996.

12. D. Zhu, J. Yue, Y. Sui, J. Cao, H. Energy, and C. Academy, “Beam size measurement and PSF evaluate of KB mirror monitor at SSRF,” Proc. 9th Int. Part. Accel. Conf., pp. 2151–2154, 2018.

13. N. Samadi et al., “A phase-space beam position monitor for synchrotron radiation,” J. Synchrotron Radiat., vol. 22, pp. 946–955, 2015.

14. N. Samadi, X. Shi, L. Dallin, and D. Chapman, “A real-time phase-space beam emittance monitoring system,” J. Synchrotron Radiat., vol. 26, no. 4, pp. 1213–1219, Jul. 2019.

15. M. Borland et al., “The upgrade of the Advanced Photon Source,” Proc. 9th Int. Part. Accel. Conf., pp. 2872–2877, 2018.

16. J. Schwinger, “On the classical radiation of accelerated electrons,” Phys. Rev., vol. 75, no. 12, pp. 1912–1925, 1949.

17. B. E. Warren, X-ray diffraction. Addison-Wesley Pub. Co., 1969.

18. W. H. W. Zachariasen, Theory of X-Ray Diffraction in Crystals. New York: John Wiley, 1945.

19. L. Rebuffi and M. Sánchez del Río, “ShadowOui : a new visual environment for X-ray optics and synchrotron beamline simulations,” J. Synchrotron Radiat., vol. 23, no. 6, pp. 1357–1367, Nov. 2016.

20 L. Rebuffi and M. Sanchez del Rio, “OASYS (OrAnge SYnchrotron Suite): an open-source graphical environment for x-ray virtual experiments,” Proc. SPIE, vol. 10388, no. August 2017, p. 103880S, 2017.

21 Y. A. Babanov, A. V. Ryazhkin, A. F. Sidorenko, and L. A. Blaginina, “Correcting an experimental absorption spectrum for the core level width,” J. Struct. Chem., vol. 39, no. 6, pp. 833–838, Nov. 1998.

22. J. C. Bergstrom and J. M. Vogt, “The X-ray diagnostic beamline at the Canadian Light Source,” Nucl. Instruments Methods Phys. Res. Sect. A Accel. Spectrometers, Detect. Assoc. Equip., vol. 587, no. 2–3, pp. 441–457, 2008.

23. M. Sanchez, N. Perez-bocanegra, X. Shi, and V. Honkimäki, “Simulation of X-ray diffraction profiles for bent anisotropic crystals,” J. Appl. Crystallogr., vol. 48, no. 2, pp. 477–491, 2015.

24. M. Sanchez del Rio and R. J. Dejus, “XOP v2.4 : Recent Developments of The X-ray Optics Software Toolkit,” Proc. SPIE, vol. 8141, p. 814115, 2011.

25. J. DuMond, “Theory of the Use of More Than Two Successive X-Ray Crystal Reflections to Obtain Increased Resolving Power,” Phys. Rev., vol. 52, no. 8, pp. 872–883, Oct. 1937.

26. O. Keski-Rahkonen and M. O. Krause, “Total and partial atomic-level widths,” At. Data Nucl. Data Tables, vol. 14, no. 2, pp. 139–146, 1974.

CHAPTER 6

This manuscript is submitted to Physical Review Accelerators and Beam.

Simulations and data analysis were done by the author, Dr. Shi and Prof. Chapman and all participated in the preparation of the manuscript.

SOURCE SIZE MEASUREMENT OPTIONS FOR LOW-EMITTANCE LIGHT SOURCES

Nazanin Samadi[a]*, Xianbo Shi[b]*, Les Dallin[c], and Dean Chapman[d]

[a]Physics and Engineering Physics, University of Saskatchewan, 116 Science Place, Saskatoon, SK, S7N5E2, Canada

[b]Advanced Photon Source, Argonne National Laboratory, 9700 S. Cass Ave., Lemont, Illinois, 60439, USA

[c]Canadian Light Source, 44 Innovation Boulevard, Saskatoon, SK, S7N2V3, Canada

[d]Anatomy, Physiology and Pharmacology, University of Saskatchewan, 107 Wiggins Road, Saskatoon, SK, S7N5E5, Canada

Correspondence email: nazanin.samadi@usask.ca, xshi@aps.anl.gov

Keywords: source size measurement; diffraction-limited storage ring; pinhole imaging; double-slit interferometry

6.1 ABSTRACT

Radiation-based techniques for measuring electron source sizes are widely used as emittance diagnostics at existing synchrotron sources. Three of these techniques, namely pinhole imaging, double-slit interferometry and a K-edge filter-based beam position and size monitor system, ps-BPM, are evaluated for measuring source sizes at low-emittance storage rings. Each technique is reviewed with a detailed system description, design optimization, and practical considerations targeted for small source sizes. Pinhole imaging has the simplest setup and gives the beam profile in both transverse dimensions but with limited resolution. Double-slit interferometry has the highest sensitivity but with limited detectable size range. The ps-BPM system shows reasonable resolution for monitoring small source sizes and divergence and can give

real-time information of source position and angle. New facilities may consider an integrated system that combines some or all of these techniques.

6.2 INTRODUCTION

Accurate measurements of electron source emittance [1] are increasingly gaining attention as new-generation synchrotron sources are being designed and built. These new machines are mostly based on Multi Bent Achromat (MBA) lattices [2] to achieve ultra-small emittance in the pm·rad level [3, 4]. As a result, improved or new diagnostic tools are desired to be able to measure and monitor such small emittances.

Electron source emittance is normally obtained indirectly from the source size and/or divergence measurements combined with the knowledge of machine parameters [5]. The most commonly used methods to measure and monitor the electron source size are pinhole imaging [6-8] and double-slit interferometry [9-11]. The pinhole imaging technique is widely used at many synchrotron facilities because of its focus-free feature. The double-slit interferometry method is based on the measurement of the transverse coherence of the photon beam. It is mostly considered for small source size measurement because of its high sensitivity. Recently, a phase-space beam position and size monitor (ps-BPM) system was developed for the full characterization of electron source position, angle, size and divergence [12, 13]. It was shown to have potential in measuring small source sizes as well [14]. In this paper, we will focus on the review of these three methods and discuss the general principles, insights on the optimization of each system, their advantages and limitations, and considerations for building practical devices.

6.3 PINHOLE IMAGING

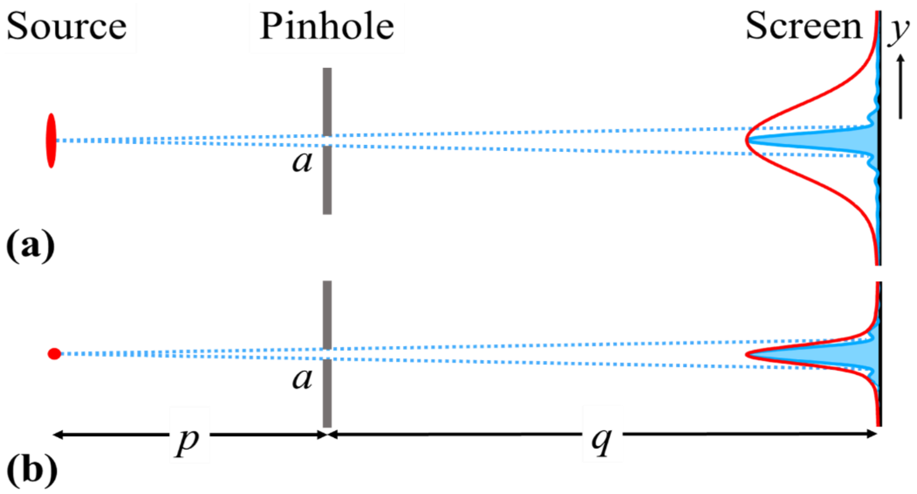

Figure 6- 1 Schematic of a pinhole imaging system. Figure a shows a relatively large source size and its profile on the detector in red the blue profile is the point spread function of the pinhole for a point source (shown in both a and b for reference). Figure b shows a small source that might be expected from an MBA type lattice. Note that the source size effects are comparable to the point spread function.

6.3.1 System description

Pinhole imaging is the most common way of measuring the transverse profile of the electron source at third generation light sources [6-8]. A schematic of an x-ray pinhole imaging system is shown in Figure 6- 1. A typical system consists of a pinhole located at a distance of p downstream of the source and a detector system at a distance q downstream of the pinhole.

The image profile recorded on the detector contains the contributions from the magnified source image, the point spread function (PSF) of the pinhole, and the PSF of the detector system [6]. Assuming all contributions are Gaussian shape functions, the Root Mean Square (RMS) size of each contribution can be added in quadrature. The measured RMS size of the image, Σ, is thus

$$\Sigma^2 = \left(M\sigma_y\right)^2 + \sigma_{pinhole}^2 + \sigma_{detector}^2, \tag{6. 1}$$

where σ_y is the electron source size, M is the magnification factor ($M = q/p$), $\sigma_{pinhole}$ is the RMS size of the pinhole PSF, and $\sigma_{detector}$ is the detector RMS resolution that can be determined experimentally [7]. Using Equation (6. 1), the electron source size σ_y can be extracted from the measured Σ, $\sigma_{detector}$ and calculated $\sigma_{pinhole}$.

The $\sigma_{pinhole}$ term can be estimated analytically as

$$\sigma_{pinhole}^2 = \sigma_{geo}^2 + \sigma_{diff}^2, \tag{6. 2}$$

where σ_{geo} and σ_{diff} are the size contribution from the geometric projection and diffraction of the pinhole, respectively.

Simplifying the discussion to one dimension, the geometric projection size of the pinhole (or 1-D slit) is given by [8]

$$\sigma_{geo} = \frac{x_g a(p+q)}{p} = \frac{a}{2\sqrt{3}}\frac{(p+q)}{p}\,, \tag{6. 3}$$

where a is the slit width, p and q are the source-to-pinhole and pinhole-to-detector distances, respectively. x_g is a constant to scale the slit width a to an equivalent RMS value. Here we choose $x_g = 1/2\sqrt{3}$ so that $x_g a$ is the RMS width of a rectangular shape with width a.

The diffraction profile of a single slit in the far-field approximation (Fraunhofer approximation) can be expressed analytically as [15]

$$I(y) = I_0 \mathrm{sinc}^2\left(\frac{\pi a}{\lambda q} y\right), \tag{6. 4}$$

where I_0 is the peak intensity, y is the vertical coordinate in the detector plane (see Figure 6- 1) and λ is the wavelength. The FWHM size of this diffraction profile is $0.886\lambda q/a$. A factor of 1/2.355 is used to convert the FWHM to the RMS value for a Gaussian function. The RMS diffraction size of a pinhole (or a slit) is then

$$\sigma_{diff} = \frac{\lambda q}{x_d a} = \frac{0.886}{2.355}\frac{\lambda q}{a}\,, \tag{6. 5}$$

where x_d is a constant and equals to 2.658.

6.3.2 Design optimization

The sensitivity of pinhole imaging is determined by the PSF of the pinhole and detector. The detector contribution needs to be as small as possible. The slit size can be optimized by minimizing the ratio of the pinhole PSF to the magnified source image size,

$$\frac{\sigma_{pinhole}}{M\sigma_y} . \tag{6. 6}$$

The optimized slit size a_0 can be obtained by setting the derivative of Equation (6. 6) to zero [6], which gives,

$$a_0 = \sqrt{\frac{\lambda q p}{x_d x_g (q+p)}} = \sqrt{\frac{0.767\lambda q p}{q+p}} . \tag{6. 7}$$

Substituting Equation (6. 7) into Equation (6. 6), the minimized ratio can be obtained as

$$\left(\frac{\sigma_{pinhole}}{M\sigma_y}\right)_{\min} = \frac{1}{\sigma_y}\sqrt{\frac{2\lambda x_g}{x_d}\left(p + \frac{p^2}{q}\right)} . \tag{6. 8}$$

Equation (6. 8) shows that the sensitivity of the system can be improved by choosing a short wavelength, small source-to-pinhole distance, and large pinhole-to-detector distance.

The above analytical formulae based on the far-field approximation give many physical insights to the system and provide general design guidelines for pinhole imaging systems. Near-field simulation is needed for obtaining accurate optimization parameters.

The PSF of the pinhole can be calculated from near-field (Fresnel) diffraction. The diffraction profile of a 1-D slit at distance q is given by [15]

$$I_s(y) = \varepsilon(y) \cdot \varepsilon^*(y)$$

$$\varepsilon(y) = \frac{1}{i\lambda q}\int_{-a/2}^{a/2} \varepsilon_0(y_0) \exp\left[\frac{i\pi}{\lambda q}(y - y_0)^2\right] dy_0 \tag{6. 9}$$

where $\varepsilon_0(y_0)$ is the wavefield in the pinhole plane. For a point source located at a distance p upstream of the pinhole, the normalized wavefield is given by

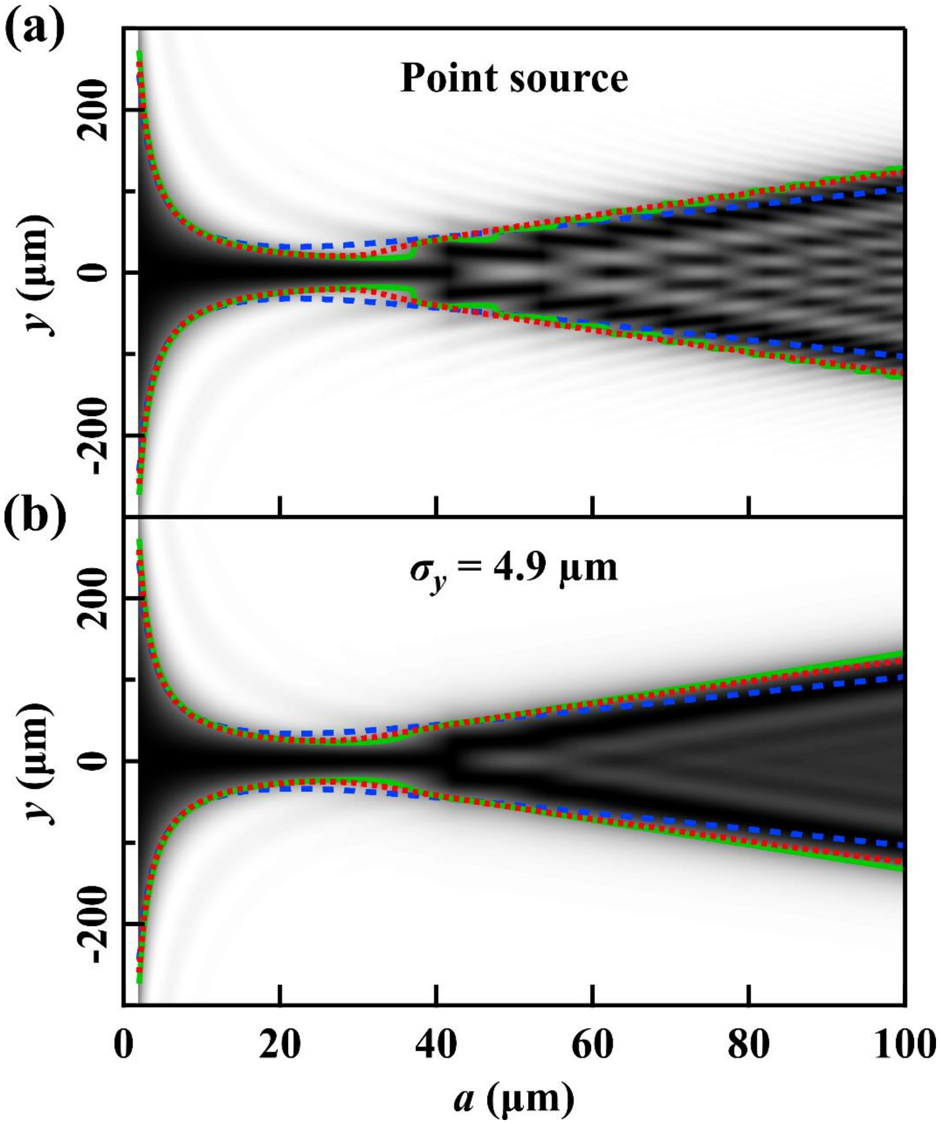

Figure 6- 2 . Normalized diffraction profiles from a 1-D slit with different a sizes simulated with Equations (6. 9)-(6. 11) for (a) a point source and (b) a Gaussian source with size σ_y = 4.9 µm (M3 bend magnet for the Advanced Photon Source upgrade source). The grayscale is linear to profile intensity and darker color indicates higher intensity. The calculation parameters are: λ = 0.827 Å (photon energy, E = 15 keV), p = 6.6 m, q = 13.4 m. The dashed curves are from the $\pm\sigma_{pinhole}$ values obtained from Equation (6. 8), the solid curves are from the FWHM/2.355 values of the diffraction profiles and the dotted curves are from the Gaussian fitted σ values.

$$\varepsilon_0(y_0) = \frac{p}{\sqrt{p^2+y_0^2}} \exp\left[\frac{i2\pi}{\lambda}\left(\sqrt{p^2+y_0^2}-p\right)\right]. \tag{6. 10}$$

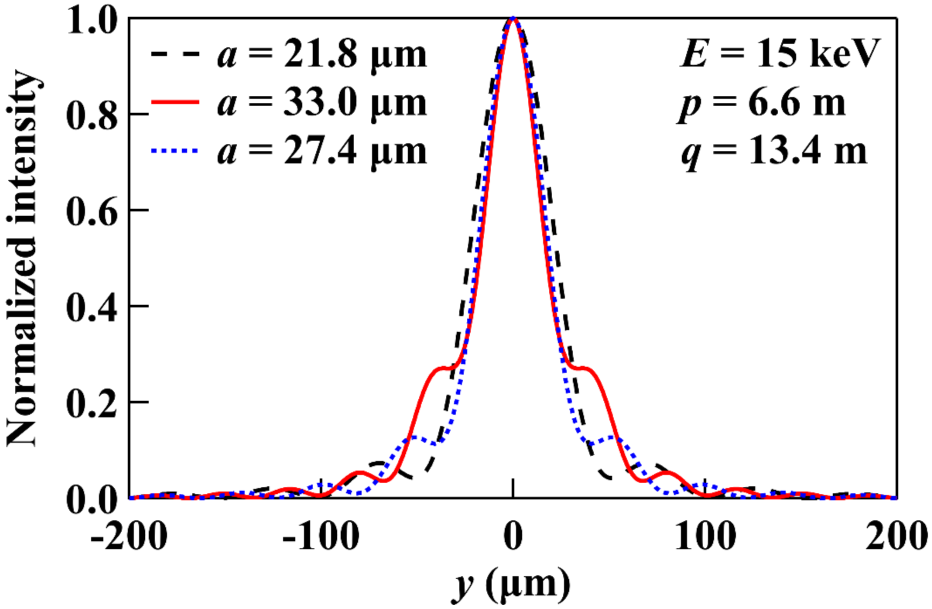

Figure 6- 3 Simulated PSF of 1-D slit sizes, a_0, optimized from (dashed curve) analytical formula Equation (6. 7), (solid curve) minimum profile width from the solid curve in Figure 6- 2a, (dotted curve) minimum Gaussian-fitted width from the dotted curve in Figure 6- 2a.

With a Gaussian distribution source, the intensity profile is given as a convolution of the diffraction pattern with the (de)magnified source profile,

$$I_G = I_s(y) \otimes \left[\exp(-\frac{y^2p^2}{2\sigma_y^2q^2})\right]. \qquad (6.\ 11)$$

where the ⊗ symbol represents the convolution operation.

Examples of simulated diffraction profiles from a 1-D slit are shown in Figure 6- 2 with the parameters in the figure caption. To compare the analytical solution and the numerical calculation, Figure 6- 2 also shows the $\pm\sigma_{pinhole}$ values extracted with different methods: (i) (dashed curves) from analytical formula Equation (6. 8), (ii) (solid curves) from the FWHM/2.355 values of the Fresnel diffraction profiles calculated with Equations (6. 9 - 6. 11), and (iii) (dotted curves) from the Gaussian fitted σ values of the diffraction profiles. Results from analytical approach provide correct trends but tend to overestimate the minimum $\sigma_{pinhole}$.

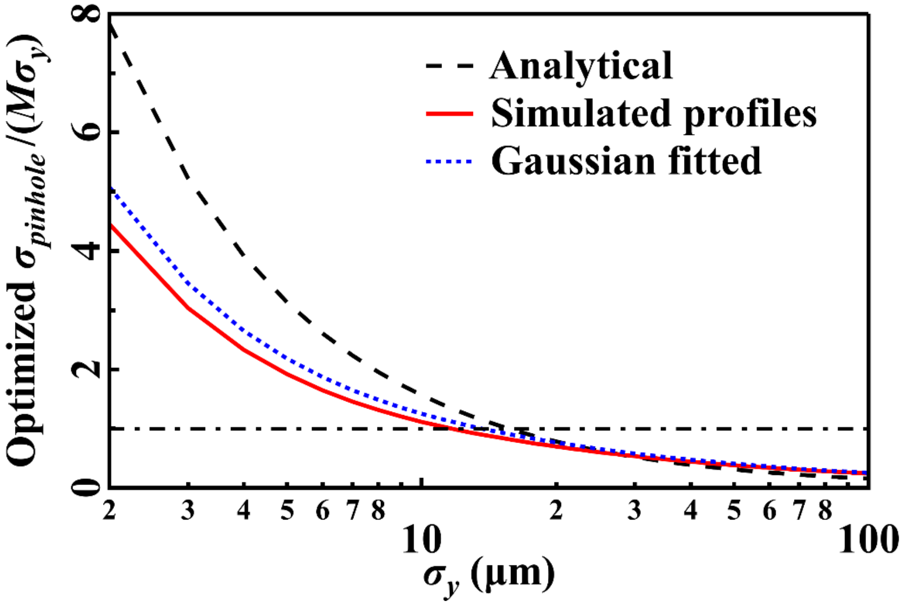

Figure 6- 4 Minimum $\sigma_{pinhole}/(M\sigma_y)$ for different source sizes σ_y obtained from three methods, see text for details. The dot-dash line indicates $\sigma_{pinhole}/(M\sigma_y)$ = 1

Figure 6- 3 shows PSF simulated with Equations (6. 9 - 6. 11) with the optimized slit size determined from the three methods above. The near-field diffraction methods give smaller $\sigma_{pinhole}$ compared to the analytical approach. The minimum $\sigma_{pinhole}$ is achieved when the diffraction profile (solid curve in Figure 6- 3) has two obvious shoulder peaks. However, the profile is far away from a Gaussian shape, which means an accurate PSF simulation and deconvolution is required in the data analysis process for extracting source sizes. The minimum Gaussian fitted $\sigma_{pinhole}$ value is a better choice for fast data-analysis and especially for real-time monitor systems.

The minimum $\sigma_{pinhole}/(M\sigma_y)$ ratios for different source sizes are shown in Figure 6- 4. Optimized pinhole sizes, a, to achieve minimum $\sigma_{pinhole}/(M\sigma_y)$ and simulated image sizes Σ are summarized in Table 6- 1 for different source sizes. When the source size is small, the PSF of the pinhole $\sigma_{pinhole}$ is much larger than the magnified source image size $M\sigma_y$. Therefore, the pinhole imaging technique is normally considered not appropriate for small source size (<10 µm) measurements. Table 6- 1 also shows that the optimized pinhole size a does not vary much for different source sizes.

Table 6- 1 Optimized pinhole sizes, a, to achieve minimum $\sigma_{pinhole}/(M\sigma_y)$ and simulated image sizes, Σ, from the three methods for different source sizes, σ_y.

σ_y (μm)	$M\sigma_y$ (μm)	a (μm)	Σ (μm)	a (μm)	Σ (μm)	a (μm)	Σ (μm)
		Analytical		Simulated profiles		Gaussian fitted	
0	0	21.8	27.0	32.9	15.1	27.3	17.2
2	4	21.8	27.3	31.3	15.9	27.3	18.0
4.9	9.8	21.8	28.8	28.9	19.3	25.7	21.2
10	20	21.8	33.8	24.9	28.0	23.3	29.7
20	40	21.8	48.8	22.5	47.2	22.5	48.5
50	100	21.8	105.0	24.9	106.8	25.7	107.5

Another main contribution to the instrument sensitivity is the PSF of the detector system, which has been studied previously [6, 7]. The PSF of the detector is normally measured with a sharp edge absorber. In principle, the detector contribution needs to be as low as possible to be comparable or smaller than $M\sigma_y$.

6.4 DOUBLE-SLIT INTERFEROMETRY

6.4.1 System description

The use of double-slit interferometry to measure the beam size in particle accelerators was first developed by Mitsuhashi at KEK in Japan [9]. Since then, this system has been used at many synchrotron facilities as a way to measure the electron beam sizes [10, 11, 16–21]. This system is mostly implemented in the visible light regime (wavelength of 400-600 nm) at third generation light sources because of (i) the availability of high-quality visible light optics and (ii) a relatively large coherence length of the visible light. Figure 6- 5 shows the basic elements of a double-slit

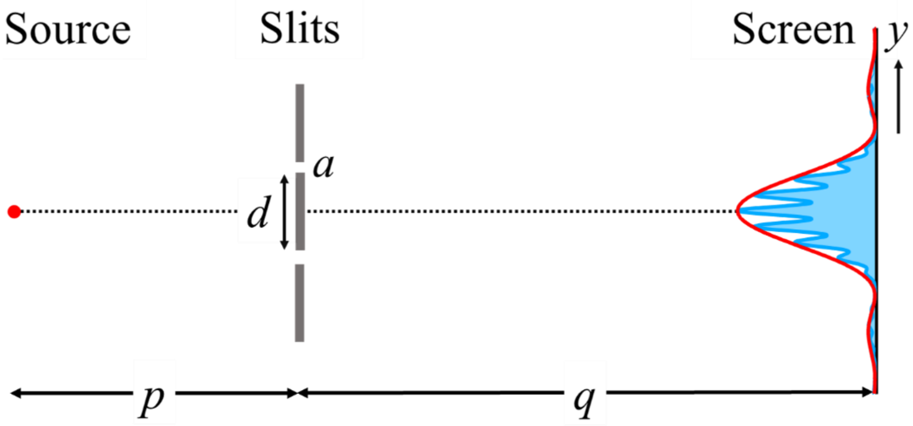

Figure 6- 5 Schematic of a double-slit interferometry system.

interferometer which consists of two narrow slits located at a distance of p downstream of the source and a detector system to measure the interference pattern at a distance q downstream of the double-slits.

A practical visible light interferometer may contain more elements including beam extraction mirrors, focusing optics to reach the far-field condition, a polarizer to select one polarization, and a band-pass filter to obtain quasi-monochromatic radiation. The resolution of such a system highly relies on the quality of the optical components and the noise in the system. The main concern of the interferometer is the distortion of the wavefront due to aberration caused by the optics. Another limitation of the system is the distortion due to mechanical vibration and air fluctuations. The electron beam oscillation can also distort the interferogram, and therefore fast detection is needed for accurate measurements.

Recently, for use in new generation facilities with ultra-small source sizes, new systems have been proposed and tested in x-ray regime (~0.1 nm wavelengths) [22]. For x-ray interferometers, the expected resolution is much higher (~ sub-micron). The setup is relatively simple and doesn't require as many optical components. At the shorter wavelength, smaller slit size and slit separation are needed. For a typical hard x-ray fourth-generation synchrotron source, the electron beam size can be as low as a few microns.

The double-slit interference, for an extended source, can be described with an analytical intensity formula within the far-field (Fraunhofer) approximation at a wavelength λ as [15],

$$I = 2I_0 \mathrm{sinc}^2\left(\frac{\pi a}{\lambda q} y\right)\left[1 + V\cos\left(\frac{2\pi d}{\lambda q} y\right)\right], \tag{6. 12}$$

where a is the slit width, d is the separation between the two slits, and V is the complex degree of coherence. Equation (6. 12) assumes the amplitudes of the wavefield passing through the two slits are equal.

The van Cittert-Zernike theorem [23] states that, for an incoherent source, the complex degree of coherence at a distance from the source, can be expressed as a Fourier transform of the spatial intensity distribution of the source. For a source with a spatially Gaussian distribution, the degree of coherence is also a Gaussian function given by,

$$V = \exp\left(-\frac{2\pi^2 d^2 \sigma_y^2}{\lambda^2 p^2}\right). \tag{6. 13}$$

Experimentally, V is visibility of the double-slit interference pattern and can be measured as,

$$V = \frac{I_{\max} - I_{\min}}{I_{\max} + I_{\min}}, \tag{6. 14}$$

where $I_{\min}$ and $I_{\max}$ are the minimum and maximum intensities of the interference pattern in the vicinity of the interferogram center. It should be noted that $0 \leq V \leq 1$.

Based on Equation (6. 13). the source size can be extracted from a single-point measurement of V (one V value at a fixed slit separation d),

$$\sigma_y = \frac{\lambda p}{\pi d}\sqrt{\frac{1}{2}\ln\frac{1}{V}}. \tag{6. 15}$$

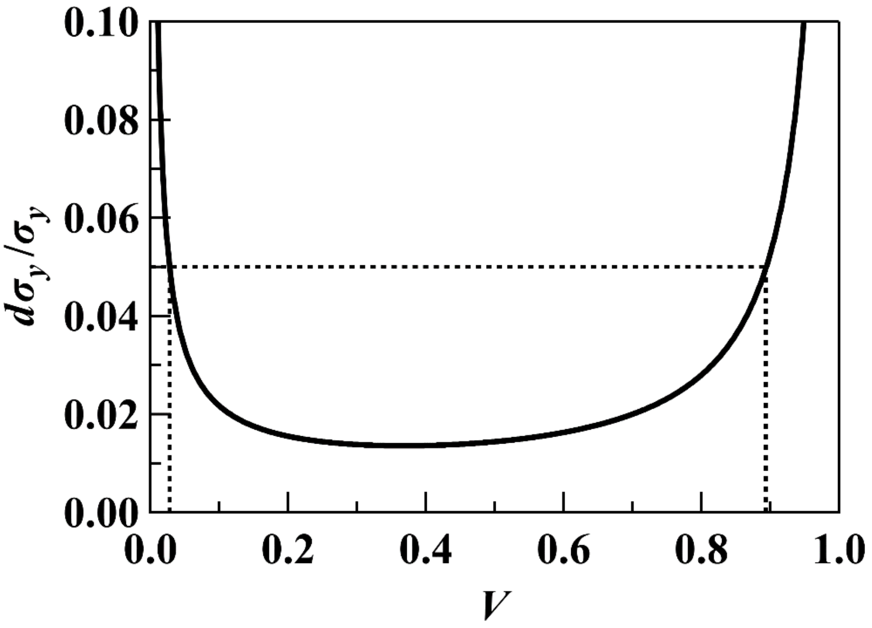

Figure 6- 6 Relative size measurement error as a function of fringe visibility V for a 0.01 visibility uncertainty. The region between the vertical dotted lines is the visibility range that gives $d\sigma_y/\sigma_y$<0.05.

6.4.2 Design optimization

The sensitivity of the double-slit interferometer relies on the statistical error dV in measuring fringe visibility. The relative size error, $d\sigma_y/\sigma_y$, can be derived from Equation (6. 15) as,

$$\frac{d\sigma_y}{\sigma_y} = \frac{dV}{12\ln\frac{1}{V}}\,. \tag{6. 16}$$

Note that the relative size error is only a function of visibility. For a visibility error of dV = 0.01, the V dependent size error is plotted in Figure 6- 6.

To have a 5% or better sensitivity of source size measurement, or $d\sigma_y/\sigma_y$<0.05, the visibility range of the system needs to be in the range of 0.028<V<0.894 (see Figure 6- 6) with the minimum $d\sigma_y/\sigma_y$ at V= 0.368. Then the detectable size range is $0.0753(\frac{\lambda p}{d})<\sigma_y<0.426(\frac{\lambda p}{d})$ based on Equation (6. 15). To have a 2% or better sensitivity of source size measurement, the visibility

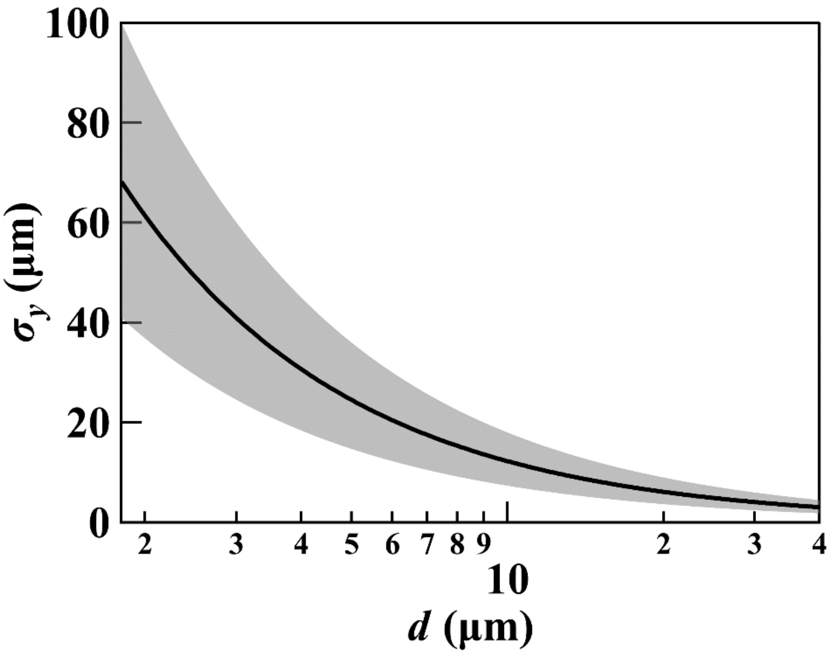

Figure 6- 7 Detectable source size range (gray area) as a function of slit separation d for a 0.01 visibility uncertainty. The solid curve shows the optimized detectable source size given by Equation (6. 17) with λ = 0.827 Å (E = 15 keV) and p = 6.6 m.

and detectable range becomes 0.12<V<0.70 and 0.13($\frac{\lambda p}{d}$)<σ_y<0.33($\frac{\lambda p}{d}$), respectively. The optimized detectable source size is obtained from Equation (6. 15) with V = 0.368 to be

$$\sigma_y = 0.225\frac{\lambda p}{d}\,. \tag{6. 17}$$

Figure 6- 7 shows the detectable source size range with 2% sensitivity as a function of slit separation d. It also provides a guideline for choosing the slit separation for the desired source size range. For a vertical source size of 4.9 μm (M3 bend magnet for the Advanced Photon Source upgrade source), a slit separation of 25 μm is optimum for λ = 0.827 Å (E = 15 keV) and p = 6.6 m.

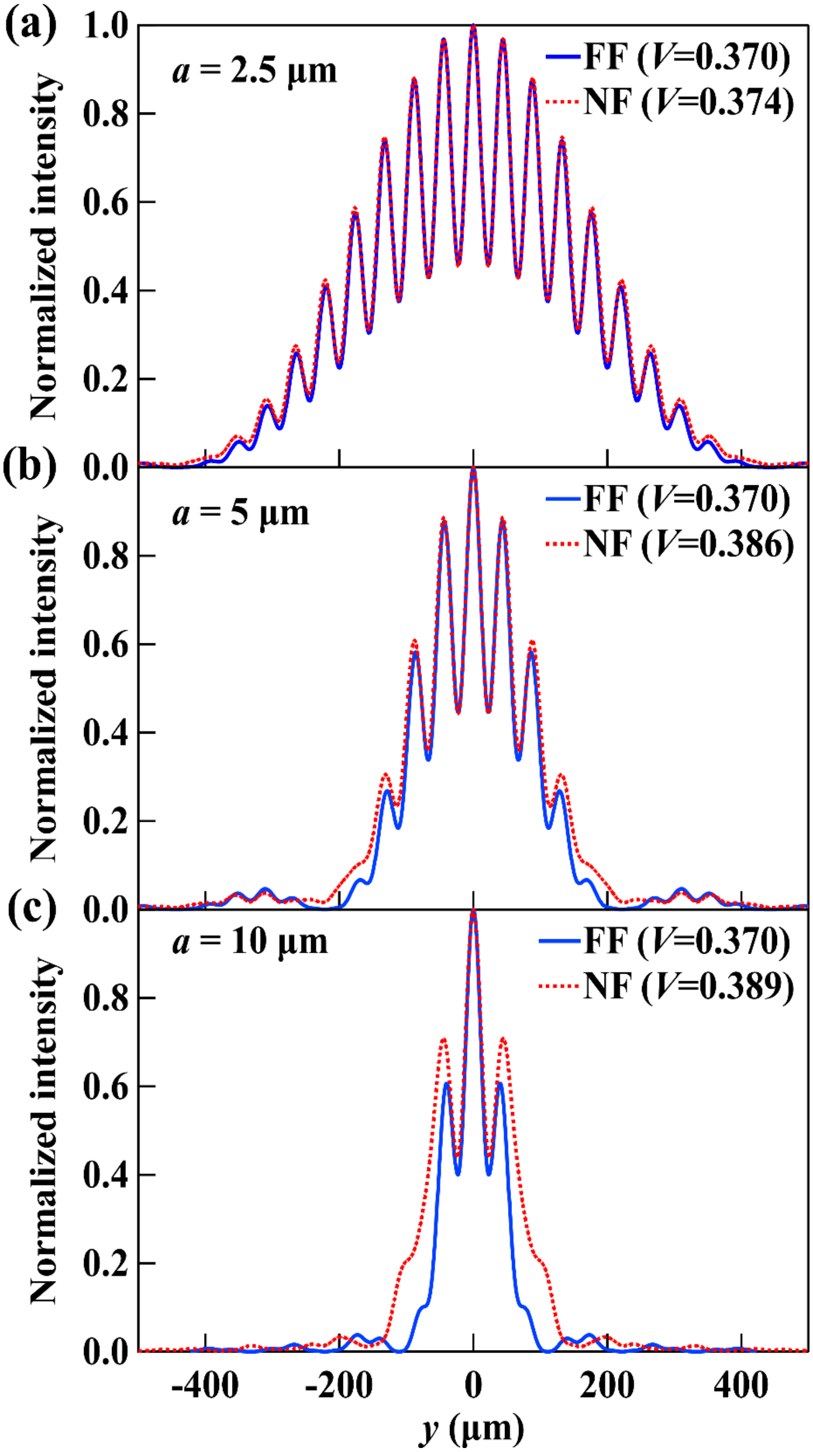

Figure 6- 8 Simulated double-slit interference profiles using (solid curves) far-field formula Equation (6. 12) and (dotted) near-field (Fresnel) calculation with different slit widths a = (a) 2.5 µm, (b) 5.0 µm, and (c) 10 µm. The other calculation parameters are: λ = 0.827 Å (E = 15 keV), p = 6.6 m, q = 13.4 m, σ_y = 4.9 µm and d = 25 µm. Figure shows the failure of the far-field approximation for large slit width, a.

The choice of the slit width can be estimated from the far-field interference profile in Equation (6. 12). The peak width of the envelope function is given by the sinc function while the period of the interference pattern is defined by the cos function in Equation (6. 12). The size of each single slit needs to be small enough so that there are enough double-slit interference peaks within the central envelope peak. When the slit width is large (a>d/5), the far-field approximation starts to fail which causes further complications. Figure 6- 8 compares simulated double-slit interference profiles by Equation (6. 12) and by near-field (Fresnel) with different slit widths. A slit width of a = d/5 is adequate for most cases.

Double-slit interferometry methods require a monochromatic photon beam. The choice of photon energy is flux driven. For a desired source size measurement, the optimized condition based on Equation (6. 17) requires that $(\lambda p/d)$ or (p/Ed) is a constant. Since slit width, a, is proportional to d, then p/Ea is a constant. The total transmitted flux through a fixed size double-slit is proportional to slit width, a, and inversely proportional to p^2. Therefore, the total flux is proportional to a/p^2 or $1/Ep$. Considering that most of the scintillator detectors have linear response in energy, the overall response on the detector is proportional to $1/p$. Thus, the energy choice only depends on the flux spectrum of the BM radiation. Also, the source-to-slit distance p needs to be minimized to maximize the flux. On the other hand, smaller p and λ implies smaller d and a, which makes slit manufacturing difficult.

In summary, an energy should be chosen to optimize the flux, from there an optimized slit separation and size are chosen based on the source size, then p needs to be as small as practically possible.

Detector resolution is also important for the double-slit interference method. Effects of detector resolution (σ_{det} of a Gaussian PSF) on the interference pattern is shown in Figure 6- 9.

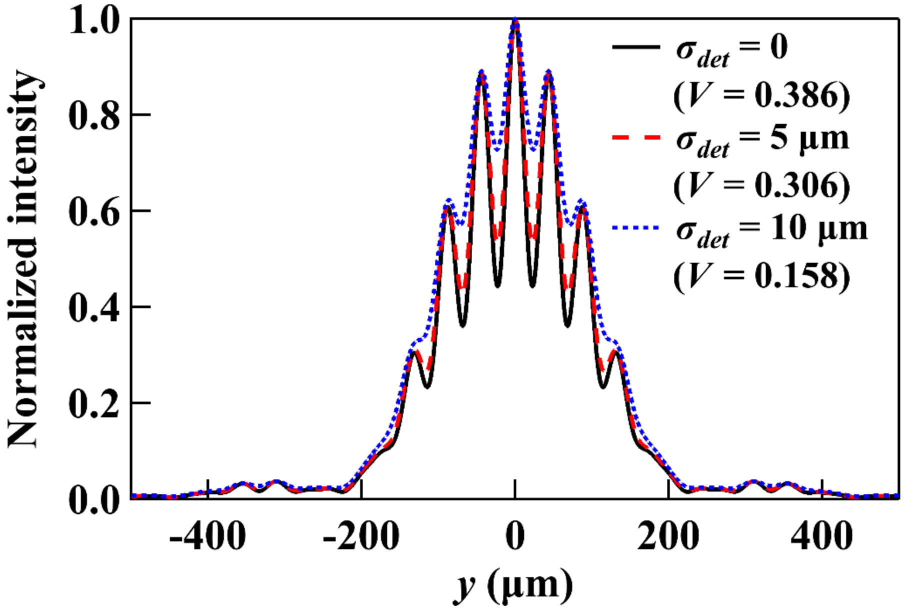

Figure 6- 9 Simulated double-slit interference profiles using near-field (Fresnel) calculation with different detector resolutions, σ_{det} of a Gaussian PSF of 0 µm (solid curve), 5.0 µm (dashed curve), and 10 µm (dotted curve). Other parameters are: λ = 0.827 Å (E = 15 keV), p = 6.6 m, q = 13.4 m, σ_y = 4.9 µm, d = 25 µm.

The detector resolution needs to be high enough to maintain the high visibility, and the detector PSF needs to be measured accurately to extract correct source sizes. The blurring effect of a detector is also determined by the peak separation in the interference pattern. Peak separation is the period of the cos function in Equation (6. 12), given by $\lambda q/d$. Since λ/d is predetermined from the desired source size by Equation (6. 17), the only way to reduce the detector blurring is to increase the slit-to-detector distance q. However, increasing q will reduce the flux density on the detector.

6.4.3 π-polarization with diffraction obstacle

The original π-polarization method is based on measuring the image of the π-polarized UV-vis light [24, 25]. The filament-beam-spread-function (FBSF) of the π-polarized UV-vis light has an on-axis zero intensity minimum. The recorded image at the detector is a convolution of the

FBSF and the electron source distribution, and thus has a blurred non-zero on-axis minimum. The electron source size can be extracted from the measured on-axis minimum when compared to pre-calculated values. The electron source profile can be obtained by deconvoluting the FBSF from the measured beam image. The π-polarization method relies heavily on the accuracy of the FBSF model. All existing systems use the Synchrotron Radiation Workshop (SRW) [26] as the backbone simulation software.

To improve the sensitivity of the π-polarization method, diffraction obstacles with different sizes can be introduced to block the central part of the photon beam [27, 28]. This so-called “obstacle diffractometer” is a variation of the double-slit interferometer. The method expects to have advantages over the traditional double-slit interferometry because of the higher acceptance angle and higher flux on the detector. The smallest electron beam size measured by the obstacle diffractometer was reported to be 3 μm with less than 10% RMS error [27].

6.5 PS-BPM SYSTEM

6.5.1 System description

The ps-BPM system was recently developed at the Canadian Light Source [12, 13]. The unique feature of the system is its ability to measure simultaneously four properties of the electron source: position, angle, size and divergence in the vertical direction. Apart from its main application as a beam position monitor, the ps-BPM system was predicted to be able to measure source sizes of a few microns [14].

The ps-BPM system contains a crystal monochromator, a K-edge filter and a detector. The monochromator is tuned to the K-edge energy of a filter and provides an energy dispersed photon beam across the vertical opening angle of the bend magnet radiation. This energy dispersion is spatially mapped on the detector. The measured K-edge width, σ_{edge}, on the detector contains contributions from the natural energy width of the K-edge [29, 30] projected to an angular width, $\sigma_{y'_{K-edge}}$, the angular bandwidth of the monochromator crystal [31], $\sigma_{y'_{mono}}$, and the electron source size, σ_y. Assuming all contributions are Gaussian shape functions, the electron source size can be obtained by

$$\sigma_y = \sqrt{\sigma_{edge}^2 - (D\sigma_{y'_{K-edge}})^2 - (D\sigma_{y'_{mono}})^2}, \qquad (6.\ 18)$$

where D is the source-to-detector distance. The electron source divergence, $\sigma_{y'}$, can be extracted from the measured full vertical beam width, σ_{beam}, without the filter by,

$$\sigma_{y'} = \frac{1}{D}\sqrt{\sigma_{beam}^2 - \sigma_y^2 - (D\sigma_{y'_{Ph}})^2}, \qquad (6.\ 19)$$

where $\sigma_{y'_{ph}}$ is the natural opening angle of the photon beam [32].

6.5.2 Design optimization

The optimization of the ps-BPM system for measuring source size was studied previously [14] by investigating different monochromator crystal reflections and monochromator geometries, K-edge filter energies and concentrations, source-to-detector distances, and detector parameters. The key results are summarized here to provide a full picture, followed by detailed studies on anticipated signal-to-noise ratio (SNR) to help guide choices for a practical system.

For the monochromator, the Bragg case geometry (reflection) was selected due to its higher reflectivity and thus higher flux over the Laue case geometry (transmission), although more effort must be done on thermal mechanical design and stability of the monochromator. Also, the scatter from the monochromator will depend on the geometry which should be considered as it may affect the system SNR.

The choice of low-indices crystal reflections (i.e. Si (1,1,1)) and elements with higher K-edge energy (e.g., barium K-edge at 37.441 keV) as filter will improve the sensitivity of the system by reducing the total contribution of the crystal bandwidth, $D\sigma_{y'_{mono}}$, and filter edge width, $D\sigma_{y'_{K-edge}}$, in Equation (6. 18). This will define the Gaussian width, σ_{IRF}, of the instrument resolution function (IRF), $f_{IRF}(y)$, of the system as the combination of the spatial width associated with the monochromator dispersion and the K-edge width,

$$\sigma_{IRF} = \sqrt{\left(D\sigma_{y'_{mono}}\right)^2 + \left(D\sigma_{y'_{K-edge}}\right)^2}. \tag{6. 20}$$

Based on Equations (6. 20), the sensitivity of the system to measure the source size will improve as a function of $1/D^2$, thus, a small source-to-detector distance is preferred. A distance of D = 10 m is a practical choice given the limitations of storage ring design and a beamline for ps-BPM measurements.

With the prior considerations regarding choices of layout and optics, ultimately the sensitivity of the ps-BPM system will rely on photon flux and noise level (SNR) which will now be considered.

A simplified model is described below to study the SNR requirement for measuring different source sizes. A Gaussian function is generated to represent the normalized beam profile with

$$I_{beam}(y) = e^{-\frac{y^2}{2\sigma_{beam}^2}}, \tag{6. 21}$$

where y is the vertical position in the detector plane with σ_{beam} being the Gaussian width of the beam profile on the detector. The filtered beam profile is obtained from multiplying I_{beam} by the transmission function of the filter

$$I_{filtered}(y) = I_{beam}(y)e^{-\frac{\mu}{\rho}(E)\rho t}, \tag{6. 22}$$

where $\mu/\rho\ (E)$ is the mass attenuation coefficient as a function photon energy E around the K-edge energy E_k of the filter, ρ is the concentration and t is the thickness of the filter. Because of the dispersion effects of the crystal, $\mu/\rho\ (E)$ can be projected into a function of y through

$$E = \frac{E_k}{D \tan \theta_B} y, \tag{6. 23}$$

where θ_B is the Bragg angle of the monochromator crystal. The $\mu/\rho\ (y)$ function is related to the measured edge profile function $f_{edge}(y)$ through

$$f_{edge}(y) = \frac{d\{-\ln[I_{filtered}(y)/I_{beam}(y)]\}}{dy} = \frac{d\frac{\mu}{\rho}(y)}{dy}\rho t. \tag{6. 24}$$

The edge profile $f_{edge}(y)$ is a convolution of the IRF, $f_{IRF}(y)$, and the electron source profile. The widths of these profiles follow the relationship described by Equation (6. 18) assuming all are Gaussian functions, or

$$f_{edge}(y) = Ae^{-\frac{y^2}{2\sigma_{edge}^2}} = Ae^{-\frac{y^2}{2\left(\sigma_y^2+\sigma_{IRF}^2\right)}}, \tag{6. 25}$$

where A is a scaling parameter to match the edge jump of $\mu/\rho\ (E)$ above and below the K-edge energy for a selected filter element and filter thickness.

The sensitivity of the source size measurement is then carried out by adding noise to the calculated beam profiles (see Figure 6- 10a). The ideal beam profile $I_{beam}(y)$ (see solid line in Figure 6- 10a) is generated with Equation (6. 21) directly. The Gaussian edge profile is first generated with Equation (6. 25), integrated to give the $\mu/\rho\ (y)$ function using Equation (6. 24), and then substituted into Equation (6. 22) to form the ideal filtered profile $I_{filtered}(y)$ (see dotted line in Figure 6- 10a). Note that the step size in y for all these profiles is chosen to represent the pixel size of the detector, σ_D.

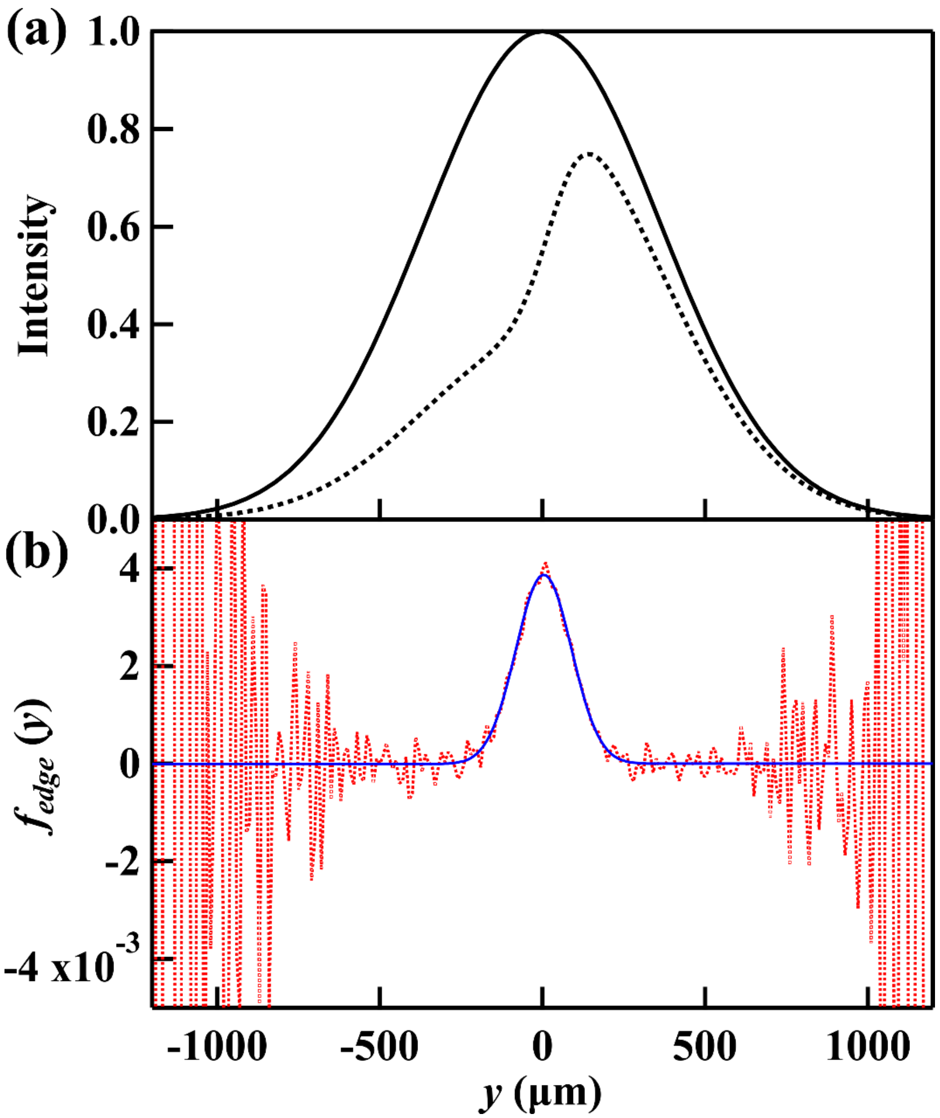

Figure 6- 10 (a) Calculated beam profiles $I_{beam}(y)$ (solid curve) and $I_{filtered}(y)$ (dotted curve) using Equations. (6. 21) and (6. 24), respectively, with σ_y = 4.9 µm, σ_y' = 2.8 µrad, $\sigma_{y'_{Ph}}$=36.1 µrad, σ_D = 10 µm, and σ_{IRF} = 85 µm. (b) Extracted edge profiles $f_{edge}(y)$ with (dotted curves) and without (solid curves) added noise to the beam profiles in (a) following Equation (6. 24).

Taking the M3 bend magnet source planned for the Advanced Photon Source upgrade [4] as an example, the nominal source parameters are σ_y = 4.9 µm, σ_y' = 2.8 µrad, and $\sigma_{y'_{Ph}}$ = 36.1 µrad. The width of the IRF for a Si (1,1,1) Bragg single-crystal monochromator at the barium K-edge (E_k = 37.441 keV) is σ_{IRF} = 85 µm at a source-to-detector distance D = 10 m [14].

If there is no noise added to the data, the edge profile can be extracted based on Equation (6. 24) and shown as solid curve in Figure 6- 10b. When a Gaussian random noise with a sigma size of 1/SNR is added to both filtered and unfiltered beam profiles, the extracted edge profile is shown as dotted curve in Figure 6- 10b. The fitted Gaussian width, σ_{edge}, of the extracted edge profile from data with added noise is then used to extract the electron source size, σ_y, using Equation (6.18).

The extracted σ_y values are evaluated with different input σ_y values, detector pixel sizes σ_D and SNR values. The goal is to find the minimum required SNR to ensure a source size measurement sensitivity <5% of the source size. The standard deviation of 1000 independently extracted σ_y values is used as a measure of the sensitivity.

Figure 6- 11a shows the required SNR to measure different source sizes (1.25 μm, 2.5 μm, 5 μm, 10 μm, 20 μm, 40 μm and 80 μm) with 5% sensitivity. To be able to measure a source size of 5 μm, a SNR of 4×10^4 is needed. The required SNR is proportional to $1/\sigma_y^2$ and almost independent of detector pixel size.

On the other hand, Figure 6- 11b shows that the extracted source size tends to be larger than the real value and increases as the detector pixel size increases. A pixel size comparable to source size σ_y is enough to provide adequate accuracy for source sizes as low as 5 μm. In practice, the pixel size can be even larger considering that the IRF can be calibrated to include effects of the detector pixel size. The IRF can be obtained either from a single measurement with a known source size, or from a series of measurements by varying relative source sizes in a known ratio as shown in [13]. Also, the IRF can be obtained by comparing with other measurement methods (e.g., pinhole imaging and double-slit interferometry).

The measurement noise of the ps-BPM system is determined by three main factors: dark noise of the detector, Compton scattering [33, 34] from the monochromator crystals and fluorescence from the K-edge filter.

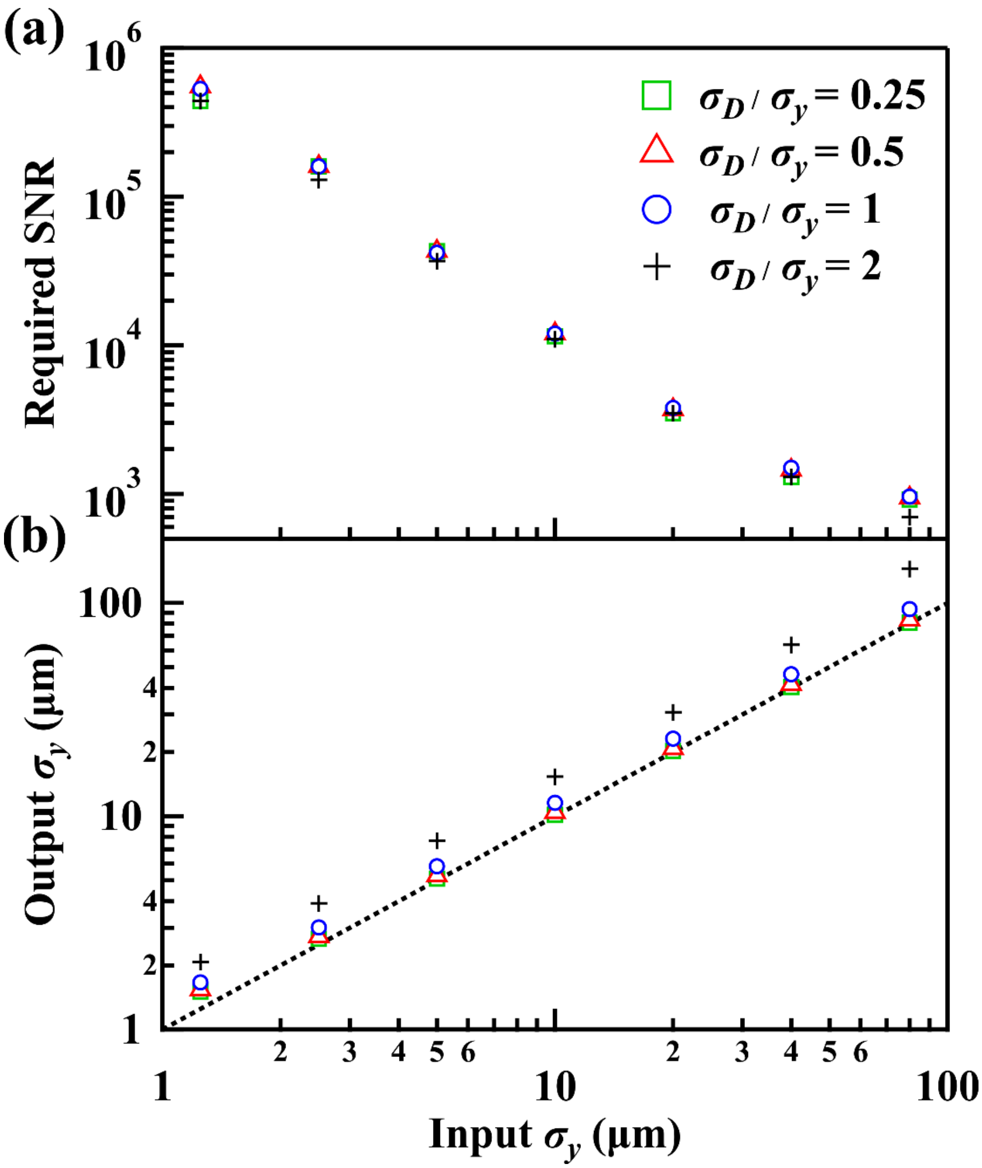

Figure 6- 11 (a) Required SNR to measure different source sizes with 5% precision, and (b) the extracted electron source sizes for different input size values, σ_y, and detector pixel sizes, σ_D.

Dark noise of the detector determines the highest SNR of a single image in the absence of other noise sources. A good scientific Complementary Metal–Oxide–Semiconductor (sCMOS) camera can have a maximum dynamical range of a few tens of thousands [35].

The Compton scattering from the monochromator crystal depends on the crystal geometry, energy, angle, distances and the spectral content of the incident synchrotron photon beam.

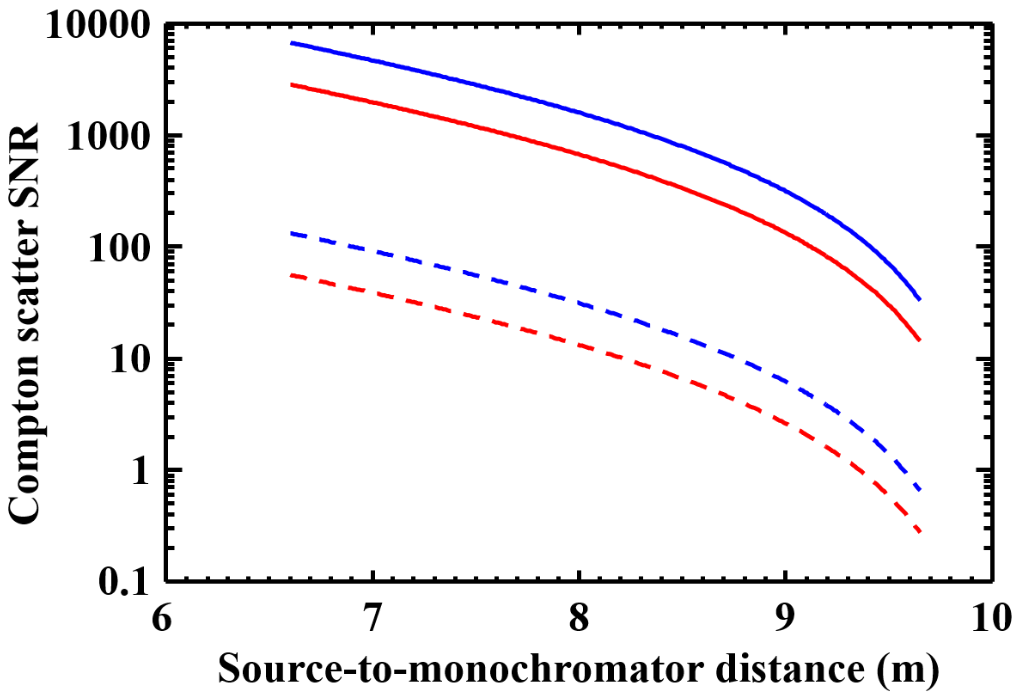

Figure 6- 12 Calculated Compton scatter SNR as a function of source-to-monochromator distance with a fixed source-to-detector distance for a single Bragg (solid curves) and a single Laue Si (1,1,1) monochromator (dashed curves). The blue curves are for the unfiltered beam and the red curves are for the filtered beam. Calculations are performed with storage ring energy, E_{ring} = 6.0 GeV, storage ring current I_{ring} = 0.2 A, and the bend magnet field B_0 = 0.657 T.

Calculations of the Compton scattering will be compared against the signal which will be either the monochromatic beam or filtered beam values. Figure 6- 12 shows the ratio of the signal to the Compton background noise (SNR) with either a single Bragg or a single Laue monochromator geometry with different source-to-crystal distances at a fixed source to the detector distance (10 m). The Bragg geometry shows much higher SNR comparing to the Laue geometry at the minimum source to monochromator possible distance for APS-U (6.6 m) with the Bragg SNR ~6700 and Laue SNR ~130. Clearly the Bragg geometry is preferred for a single crystal monochromator. This ratio of SNR is preserved for the edge side (Bragg SNR ~2800, Laue SNR ~50), but is reduced due to the filter absorption. The fluorescence from K-edge filter is another potential source of background noise, however the estimation of its contribution was found to be insignificant.

In order to further reduce the Compton scatter background, a double-Bragg or a Laue-Bragg crystal type monochromator may be used as it removes the line of sight between the detector and the first crystal which intercepts the entire photon beam and is the major source of scattering. The first crystal in a double-crystal monochromator being a Laue case has the advantage of simpler heat load management, which can reduce measurement errors caused by thermal deformation and drift.

The ps-BPM measures the vertical beam profile over a large horizontal BM fan. By summing up profiles over N_h pixels in the horizontal direction, the SNR of the vertical profile measurement can be improved by a factor of $\sqrt{N_h}$ assuming the horizontal beam is uniform. By averaging over N_i images, the SNR can be further improved to a factor of $\sqrt{N_h N_i}$. For example, from Figure 6- 11 the required SNR for measuring a 1.25 μm source size is approximately 6×10^5. The Compton SNR will need to be improved by a factor of $\sqrt{N_h N_i}$=90 for a single Bragg monochromator (SNR ~6700). Assuming N_h is 1000 horizontal pixels, then N_i ~8 measurements are needed to achieve the required SNR of 6×10^5.

6.6 Conclusion

Three radiation-based methods of measuring electron source size were studied in this work. The optimization of each method was discussed in detail for measuring small source sizes at low-emittance synchrotron light sources.

A direct comparison of these methods is difficult since each of them has its specific advantages and limitations and can provide complementary information about the source.

The pinhole imaging technique has the simplest setup and is free from optical aberration. The size measurement sensitivity relies heavily on the accurate modeling of the shape of the pinhole PSF and requires a high-resolution detector system. The pinhole imaging technique is compatible with white beam and thus can provide relatively fast measurements.

The double-slit interferometry technique has the highest sensitivity using x-rays. However, the detectable size range for a fixed slit separation is highly limited, especially for measuring smaller source sizes. A system with multiple or tuneable slit separations will be needed to cover a large measurable range.

Both pinhole imaging and double-slit interferometry methods require the accurate near-field modeling of the PSF of the system. Also, the detector PSF plays very important role in both methods.

The ps-BPM system is unique in terms of providing source information on position, angle, size and divergence simultaneously. Its source size measurement sensitivity is determined by the signal-to-noise ratio which requires careful system optimization to reduce scattering background. The ps-BPM system doesn’t require a high-resolution detector and the knowledge of the detector PSF is not required. A Gaussian IRF model for the monochromator and K-edge contributions is adequate for data analysis.

At planned low-emittance storage rings, at least a dedicated BM beamline for beam diagnostic is a must. A combination of all three techniques will be ideal to provide full characterization of the source. The pinhole imaging technique gives real-time monitoring of source profile in both transverse directions. The double-slit interferometry can be used in either direction and can provide accurate source size measurement and calibration for pinhole imaging and the ps-BPM system. The ps-BPM system monitors all four parameters of the source in the vertical direction. A separate horizontal deflecting monochromator can be used to measure the horizontal source position and size.

6.7 ACKNOWLEDGEMENTS

The authors acknowledge the financial support of Natural Sciences and Engineering Research Council of Canada (NSERC) Discovery Grant, Canadian Institutes of Health Research (CIHR) Team Grant – Synchrotron Medical Imaging, CIHR Training Grant - Training in Health Research Using Synchrotron Techniques, Canada Research Chair Program, Saskatchewan Health Research Foundation Team Grant and the University of Saskatchewan. The research described in this paper was performed at the Canadian Light Source, which is funded by the Canada Foundation for Innovation, NSERC, the National Research Council Canada, CIHR, the Government of Saskatchewan, Western Economic Diversification Canada, and the University of Saskatchewan. This work was also supported by the U.S. Department of Energy, Office of Basic Energy Sciences, under Contract No. DE-AC02-06CH11357.

6.8 REFERENCES

1. J. Buon, “Beam phase space and emittance,” CAS - Cern Accel. Sch. 5th Gen. Accel. Phys. Course, 1992.
2. D. Einfeld, M. Plesko, and J. Schaper, “First multi-bend achromat lattice consideration,” J. Synchrotron Radiat., vol. 21, no. 5, pp. 856–861, 2014.
3. P. F. Tavares, S. C. Leemann, M. Sjöström, and A. Andersson, “The MAX IV storage ring project.,” J. Synchrotron Radiat., vol. 21, no. Pt 5, pp. 862–77, 2014.
4. M. Borland et al., “The upgrade of the Advanced Photon Source,” Proc. 9th Int. Part. Accel. Conf., pp. 2872–2877, 2018.
5. G. Kube, “Review of synchrotron radiation based diagnostics for transverse profile measurements,” 8th Eur. Work. Beam Diagnostics Instrum. Part. Accel. DIPAC 2007, pp. 6–10, 2007.

6. C. Thomas, G. Rehm, I. Martin, and R. Bartolini, “X-ray pinhole camera resolution and emittance measurement,” Phys. Rev. Spec. Top. - Accel. Beams, vol. 13, no. 2, pp. 1–11, 2010.

7. C. A. Thomas and G. Rehm, “Pinhole camera resolution and emittance measurement,” EPAC 2008 - Contrib. to Proc., pp. 1254–1256, 2008.

8. P. Elleaume, C. Fortgang, C. Penel, and E. Tarazona, “Measuring Beam Sizes and Ultra-Small Electron Emittances Using an X-ray Pinhole Camera,” J. Synchrotron Radiat., vol. 2, no. 5, pp. 209–214, 1995.

9. T. Mitsuhashi, “Beam Measurement: Proceedings Of The Joint US-CERN-Japan-Russia School On Particle Accelerators,” in Beam measurement: Proceedings, Joint US-CERN-Japan-Russia School on Particle Accelerators, Montreux and Geneva: World Scientific Publishing Company, 1999, pp. 399–427.

10. T. Naito and T. Mitsuhashi, “Very small beam-size measurement by a reflective synchrotron radiation interferometer,” Phys. Rev. Spec. Top. - Accel. Beams, vol. 9, no. 12, pp. 1–7, 2006.

11. J. Corbett et al., “Transverse beam profiling and vertical emittance control with a double-slit stellar interferometer,” Proc. IBIC2016, pp. 236–239, 2017.

12. N. Samadi et al., “A phase-space beam position monitor for synchrotron radiation,” J. Synchrotron Radiat., vol. 22, pp. 946–955, 2015.

13. N. Samadi, X. Shi, L. Dallin, and D. Chapman, “A real-time phase-space beam emittance monitoring system,” J. Synchrotron Radiat., vol. 26, no. 4, pp. 1213–1219, Jul. 2019.

14. N. Samadi, X. Shi, and D. Chapman, “Optimization of a phase-space beam position and size monitor for low-emittance light sources,” J. Synchrotron Rad., vol. accepted, 2019.

15. J. W. Goodman, Introduction to Fourier optics. New York: McGraw-Hill, 1996.

16. M. Masaki and S. Takano, “Two-dimensional visible synchrotron light interferometry for transverse beam-profile measurement at the SPring-8 storage ring,” J. Synchrotron Radiat., vol. 10, no. 4, pp. 295–302, Jul. 2003.

17. S. T. Wang et al., “Visible-light beam size monitors using synchrotron radiation at CESR,” Nucl. Instruments Methods Phys. Res. Sect. A Accel. Spectrometers, Detect. Assoc. Equip., vol. 703, pp. 80–90, Mar. 2013.

18. M. Koopmans et al., “Applications of the Interferometric Beam Size Monitor at BESSY II; Applications of the Interferometric Beam Size Monitor at BESSY II,” Proc. 9th Int. Part. Accel. Conf., pp. 2103–2106, 2018.

19. L. Torino and U. Iriso, “Transverse beam profile reconstruction using synchrotron radiation interferometry,” Phys. Rev. Accel. Beams, vol. 19, no. 12, p. 122801, Dec. 2016.

20. G. Trad, E. Bravin, A. Goldblatt, S. Mazzoni, F. Roncarolo, and T. Mitsuhashi, “Beam size measurements using interferometry at LHC,” Proc. IBIC2016, pp. 583–588, 2017.

21. M. L. Chen et al., “Recent beam size measurement result using synchrotron radiation inteferometer in TPS,” Proc. IBIC2016, pp. 217–220, 2017.

22. W. Leitenberger, H. Wendrock, L. Bischoff, and T. Weitkamp, “Pinhole interferometry with coherent hard X-rays.,” J. Synchrotron Radiat., vol. 11, no. Pt 2, pp. 190–7, Mar. 2004.

23. M. Born and E. Wolf, Principles of Optics, 7th ed. Cambridge University Press, 1999.

24. A. Hansson, E. Wallén, and Å. Andersson, “Transverse electron beam imaging system using visible synchrotron radiation at MAX III,” Nucl. Instruments Methods Phys. Res. Sect. A Accel. Spectrometers, Detect. Assoc. Equip., vol. 671, pp. 94–102, 2012.

25. Å. Andersson, M. Böge, A. Lüdeke, V. Schlott, and A. Streun, “Determination of a small vertical electron beam profile and emittance at the Swiss Light Source,” Nucl. Instrum. Methods Phys. Res. A, vol. 591, no. 3, pp. 437–446, 2008.

26. O. Chubar and P. Elleaume, “Accurate and efficient computation of synchrotron radiation in the near field region,” in proc. of the EPAC98 Conference, 1998, pp. 1177–1179.

27. J. Breunlin, Andersson, N. Milas, Saá Hernández, and V. Schlott, “Methods for measuring sub-pm rad vertical emittance at the Swiss Light Source,” Nucl. Instrum. Methods Phys. Res. A, vol. 803, pp. 55–64, 2015.

28. J. Breunlin and Å. Andersson, “Emittance diagnostics at the MAX IV 3 GeV storage ring,” Proc. 7th Int. Part. Accel. Conf., pp. 2908–2910, 2016.

29. Y. A. Babanov, A. V. Ryazhkin, A. F. Sidorenko, and L. A. Blaginina, “Correcting an experimental absorption spectrum for the core level width,” J. Struct. Chem., vol. 39, no. 6, pp. 833–838, Nov. 1998.

30. O. Keski-Rahkonen and M. O. Krause, “Total and partial atomic-level widths,” At. Data Nucl. Data Tables, vol. 14, no. 2, pp. 139–146, 1974.

31. W. H. W. Zachariasen, Theory of X-Ray Diffraction in Crystals. New York: John Wiley, 1945.

32. J. Schwinger, “On the classical radiation of accelerated electrons,” Phys. Rev., vol. 75, no. 12, pp. 1912–1925, 1949.

33. A. H. Compton, “A Quantum Theory of the Scattering of X-rays by Light Elements,” Phys. Rev., vol. 21, no. 5, pp. 483–502, 1923.

34. A. H. Compton, “The Spectrum of Scattered X-Rays,” Phys. Rev., vol. 22, no. 5, pp. 409–413, Nov. 1923.

35. Andor, “EMCCD vs sCMOS Cameras | A Comparison.” [Online]. Available: https://www.oxinst.com/learning/view/article/comparing-scmos.

CHAPTER 7

CONCLUSION AND FUTURE WORK

7.1 CONCLUSION

This thesis detailed a phase-space beam position and angle monitor system and further explored its ability to measure electron source size and divergence. The applications, optimizations, and design considerations of the ps-BPM system were studied.

A theoretical model and data analysis protocol were developed to extract electron source size and divergence from measured widths of unfiltered beam and K-edge filtered beam. The electron source size can be obtained by subtracting the monochromator bandwidth and natural K-edge width from the measured K-edge width in quadrature. The source divergence can be extracted consequently from the measured unfiltered beam width, the calculated natural opening angle of the photon beam, and the electron source size, by quadrature subtraction. Experimental results of the ps-BPM measurements were carried out at the CLS BMIT-BM beamline and compared with pinhole-based measurements. The physical model of the ps-BPM system was also validated by ray-tracing simulation (objectives 1 & 2).

Up to this point, a full physical model has been developed for the ps-BPM system, which has the unique feature of characterizing electron source properties (position, angle, size and divergence) in one set of measurements. Succeeding studies showed real applications of the ps-BPM system in monitoring beam motions and size variations during normal operations and other machine conditions. The combination of analysis in both time and frequency domain can provide even more information about the source and beamline optics (objective 3).

The optimization of the ps-BPM system was carried out aiming to measure ultra-small source sizes (a few microns) at the planned and built low-emittance light sources. Factors considered include the choice of monochromator geometry, crystal reflection, K-edge filter energy, filter concentration, and geometry of the system layout. An optimized system validated by simulations showed that the ps-BPM system is able to detect the APS-U source size with a few percent sensitivity, thus it is suitable for next-generation light sources (objective 4).

Finally, detailed overviews were given on three techniques for measuring small electron source sizes. The optimization of the pinhole imaging technique, double-slit interferometry method and ps-BPM system were discussed along with their advantages and limitations. The sensitivity of the ps-BPM system was shown to be driven by the signal-to-noise ratio. The effects of detector dark noise and Compton scattering background were studied to provide guidelines for practical design of the system. A combination of multiple techniques was suggested for planned low-emittance light sources towards the full characterization of the electron source (objective 5).

Over the course of this work, it has become increasingly clear that this system can play a major role in assessing the performance of the new generation synchrotron sources such as those employing the MBA high brightness lattices. This is reinforced by the strong collaboration with APS-U (Dr. Xianbo Shi) and interest from other facilities.

7.2 FUTURE WORK

The ability of the ps-BPM system to measure small source sizes (less than 10 micron) needs to be verified experimentally at a synchrotron BM beamline. The sensitivity of the system needs to be studied and optimized to ensure less than 5% measurement uncertainty.

For absolute measurements the instrument resolution function of the ps-BPM system needs to be calibrated experimentally either by comparing to other known methods or by measurements with known source sizes or source size changes.

The tolerance of the system needs to be studied experimentally or modeled in terms of optical mechanical and thermal stabilities. The temperature effects on the monochromator will alter the d-spacing and move the K-edge energy and thus will create a false positive beam motion effect of the electron source.

The dynamic range of the system needs to be considered in the modeling process to define the useful range of position, angle, source size and divergence changes. The limits for measuring the source position and angle has to be considered in a phase space sense to account for combinations of the beam motion (position and angle).

Other ways of monitoring beam position should be considered. Because of the step-function nature of the edge, it may be possible to measure the beam position by measuring just the entire intensity of the beam on the K-edge side of the data. Similarly, the position and angle on the beam side could be determined by looking at the intensity variations from top and bottom halves of the beam. Between these three measurements it should be possible to simply calculate the beam position and angle independently and in real-time.

The use of a crystal monochromator to select the energy around the K-edge will also suffer from the possible selection of harmonic energies which are multiples of the fundamental energy. This energy contamination of the beam will affect the sensitivity and accuracy of the system also needs to be considered in the modeling process. This was considered in this work which led to the choice of energies that were well above the critical energy of the bend magnet to avoid harmonic contamination in the data. However, no calculation or modeling has been done to include the effects of harmonics thus far.

One of the original potential applications of the ps-BPM was to look at the possibility of using the beam position and angle information to correct experimental data at the beamline if beam motions exist. This hasn’t been done, but the data has been acquired but not processed yet.

APPENDIX A

This paper was published in the Journal of Synchrotron Radiation in April 2015 (Samadi, N., et al., A phase-space beam position monitor for synchrotron radiation. J Synchrotron Radiat, 2015. 22(4): p. 946-55). The author took all of the data and did all of the data analysis. The author arranged for the beamtime and coordinated data acquisition with the beam motion studies. Others were involved in the experimental setup (Martinson, Belev), literature search (Bassey), storage ring properties and predicted beam motions (Dallin, de Jong) and algorithm development (Chapman). The author and Prof. Chapman prepared the manuscript draft which was reviewed by the other co-others.

A PHASE SPACE BEAM POSITION MONITOR FOR SYNCHROTRON RADIATION

Nazanin Samadi[a]*, Bassey Bassey[b], Mercedes Martinson[b], George Belev[c], Les Dallin[c], Mark de Jong[c], Dean Chapman[d]

[a]Biomedical Engineering, University of Saskatchewan, 107 Wiggins Rd, Saskatoon, SK, S7N 5E5 Canada
[b]Physics and Engineering physics, University of Saskatchewan, 116 Science Place, Saskatoon, SK, S7N 5E2 Canada
[c]Canadian Light Source, 44 Innovation Boulevard, Saskatoon, SK, S7N 2V3, Canada
[d]Anatomy and Cell Biology, University of Saskatchewan, 107 Wiggins Rd, Saskatoon, SK, S7N 5E5, Canada
Correspondence email: nazanin.samadi@usask.ca

Keywords: beam position monitor, x-ray diffraction, k-edge absorption, phase space

Synopsis A system has been developed to measure the vertical position and angle of the electron beam at a single location from a synchrotron source. The system uses a monochromator tuned to the absorption edge of a contrast material and has a sensitivity comparable to other beam position monitors

A.1 ABSTRACT

The stability of the photon beam position on synchrotron beamlines is critical for most if not all synchrotron radiation experiments. The position of the beam at the experiment or optical element location is set by the position and angle of the electron beam source as it traverses the magnetic field of the bend magnet or insertion device. Thus an ideal photon beam monitor would be able to simultaneously measure the photon beam's position and angle, and thus infer the electron beam's position in phase space.

X-ray diffraction is commonly used to prepare monochromatic beams on x-ray beamlines usually in the form of a double crystal monochromator. Diffraction couples the photon wavelength or energy to the incident angle on the lattice planes within the crystal. The beam from such a monochromator will contain a spread of energies due to the vertical divergence of the photon beam from the source. This range of energies can easily cover the absorption edge of a filter element such as iodine at 33.17 keV. A vertical profile measurement with and without the filter can be used to determine the vertical angle and position of the photon beam. In these measurements an imaging detector measures these vertical profiles with an iodine filter that horizontally covers part of the monochromatic beam.

The goal was to investigate the use of this combined monochromator, filter and detector as a phase space beam position monitor. The system was tested for sensitivity to position and angle under a number of synchrotron operating conditions, such as normal operations and special operating modes where the beam is intentionally altered in position and angle. The results are comparable to other methods of beam position measurements and indicate that such a system is

feasible in situations where part of the white synchrotron beam can be used for the phase space measurement.

A.2 INTRODUCTION

The trajectory of a photon beam can be determined if both the position and angle can be found at some point along the propagation direction. From knowledge of this beam's position and angle or its position in phase space, it is possible to transform back to the source and determine the source coordinates in phase space if the optics in the intervening locations and their effects are known.

This paper describes a method to simultaneously measure the photon beam position and angle at one location. This system was developed at the Canadian Light Source (CLS) on the Biomedical Imaging and Therapy (BMIT) bend magnet beamline 05B1-1 (BM).

The CLS is a third generation synchrotron facility with a low electron beam emittance (ε_x = 18 nm-rad, ε_y = 0.10 nm-rad). Beam instability, be it electron or photon beam, can be a concern especially to the third generation facilities. It has adverse effects on the required low electron beam emittance, effective brilliance of the synchrotron radiation, and experiments performed at the experimental stations [1-4]. The causes of beam instability and the methods of reduction have been widely studied [5-8], and the drive to ensure and maintain a steady beam has led to the development of different types of beam monitors [9-23].

Photon beam position and angle instabilities at experimental stations are attributed to fluctuations of stored electron beam orbit and vibrational and thermal distortion of beamline optical components. The usual target for stability in the vertical plane is 10 % of the beam size in position and angle [8]. Most of the available photon beam monitors are sensitive to the beam position only, and hence the name photon beam-position monitors (PBPM). However, the measured beam position is determined by both the source position and angle. A single PBPM does not provide independent information about the photon beam source position and angle [18, 24]. The photon beam angle needs to be monitored to account for the negative effects of beam angle instability [18, 25-27]. The use of two photon PBPMs is common, when the position and angle of a photon beam is to be measured [18, 22, 23].

At the CLS, beam instabilities are monitored by two diagnostic beamlines - the Optical Synchrotron Radiation (OSR) and the X-ray Synchrotron Radiation (XSR) beamlines [28]. Most beamlines at the CLS have provision for some type of PBPMs, but few are actually implemented or used. These monitors are of the type that measure only the photon beam position at some location in the beamline.

As with almost all synchrotron experiments imaging is affected by photon beam motion. One of the imaging methods used at BMIT beamline is K-edge subtraction using an iodine contrast element with a beam prepared by a bent Laue monochromator. Measurements made with this system during a period of electron beam instability gave the idea that we can measure the photon beam position and angle or from it infer the electron beam's position in phase space.

We present a method for measuring the position and angle of a photon beam simultaneously – a phase space – Beam Position Monitor (ps-BPM). The method relies on the energy dispersive properties of flat crystals and makes use of the absorption edge of a filter in the photon beam path to determine a specific energy or angle of the photon beam. This, coupled with a measurement of the beam in the absence of the filter, allows beam position and angle to be determined.

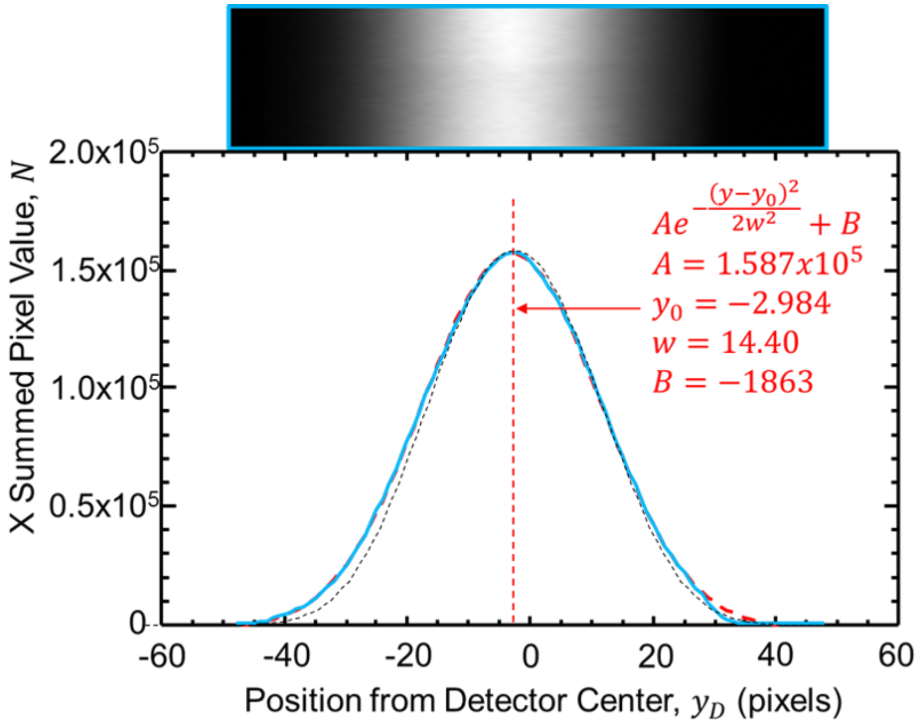

Figure A- 1 Nearly Gaussian vertical beam profile as measured on the CLS BMIT bend magnet beamline. The picture at the top is an image of the beam. The plot at the bottom shows the measured beam profile from that image (blue) and a Gaussian fit (red dash). The red dotted line identifies the center. The red text gives the least squares Gaussian fitting parameters. The vertical scale is in pixel units (100 micron pixel size). The calculated beam profile is shown as the black dashed line.

A.2.1 Synchrotron Radiation

The single electron vertical photon emission distribution is properly described by a modified Bessel function of the second kind [29]; however, this distribution is well modelled as a Gaussian function. This vertical angular distribution mostly falls within a $1/\gamma$ range in the X-ray where γ is the electron beam energy divided by the electron rest mass (γ=5675 for the CLS). The electron beam size and vertical angle distribution can also be described as a Gaussian function. Therefore, the bend magnet synchrotron beam has a vertical distribution that is nearly Gaussian. A measured comparison of the vertical distribution of the beam on the CLS BMIT bend magnet beamline is shown in Figure A- 1 at 33.17 keV. As measured some distance from the source, the vertical angle or position motion of the electron source will move this distribution vertically. Because the measurement distance from source can be tens of meters, the angle affects are amplified. For example, the profile measured in Figure A- 1 is at 26 m from the electron beam source. In this figure the blue line is the measured profile from the image at the top of the figure. The red dashed line is a Gaussian fit to that profile.

The fact that the red dashed line is hard to see indicates how closely the Gaussian fit is to the actual beam profile. The black dashed line is a calculated profile from the modified Bessel function [29] for the actual conditions of the measurement [CLS Bend Magnet (2.9 GeV & 1.354 T) at 26 m from the source with 100 μm pixels and 33.17 keV photon energy].

A.2.2 Double Crystal Monochromator at an Absorption Edge

Diffraction of x-rays in crystals can be thought of as arising from constructive interference from reflections at lattice planes as described by Bragg's law,

$$\lambda = 2d_{hkl}sin\theta, \tag{A. 1}$$

where λ is the wavelength of the diffracted beam, θ is the angle between the incident beam and lattice planes, d_{hkl} (called the d-spacing) is the spacing between the (h,k,l) lattice planes.

For an x-ray synchrotron beamline, usually a pair of parallel crystals is used – one to monochromatize the incident beam and one to diffract that beam back parallel to the incident beam. With a coordinated motion of the two crystals, a range of energies can be chosen while keeping the monochromatic beam from the second crystal in the same location which is very useful for much of the research being done. Additionally, the near unit reflectivity of the perfect crystals often used means there is little intensity loss from the pair. This arrangement is commonly called a double crystal monochromator (DCM) [30].

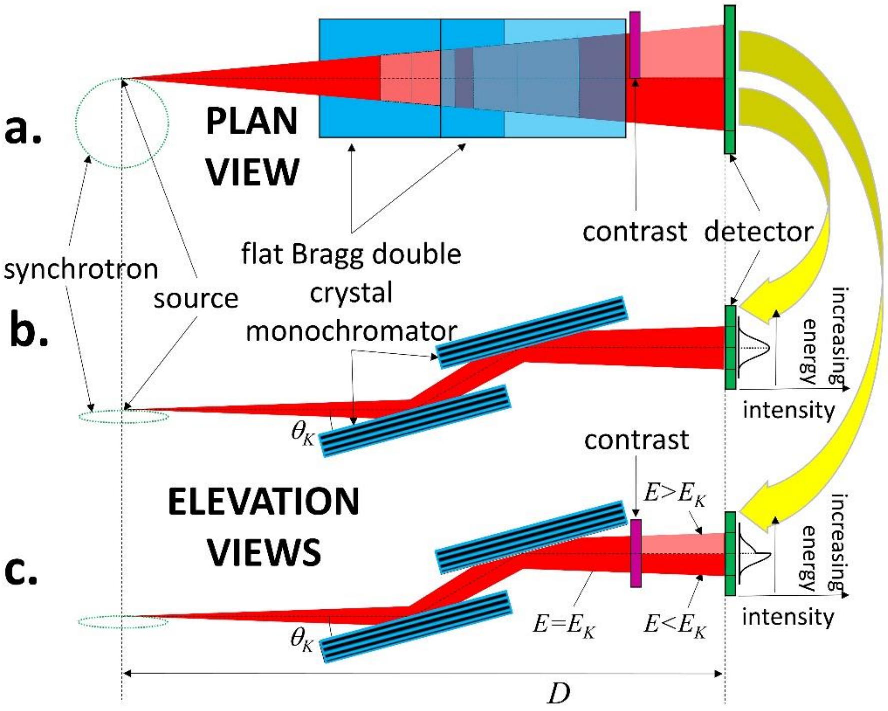

Figure A- 2 Schematic of the system used at BMIT bend magnet beamline. (a) Plan view of the double crystal monochromator (DCM), contrast material and detector. (b) Elevation view of the non-contrast or beam side; (c) elevation view with contrast material whose K-edge is at the vertical middle beam prepared by the DCM. Example plots at the right show the profile for the unfiltered beam (b) and contrast filtered beam (c).

When a DCM is tuned to an energy some of the beam will be above and some below the mean energy , for example, the K- edge energy of an element, some of the transmitted beam will be above and some below the mean energy due to the dispersion properties of the crystals. This range of energies arises from the range of incident photon beam angles onto the lattice planes of the crystal and/or the energy bandwidth of the crystal and the reflection used. The range of energies due to angular divergence onto the planes is easily calculated using Bragg's law based on the monochromator reflection used and the angular size of the beam passed through the system. A schematic of a DCM arrangement is shown in Figure A- 2.

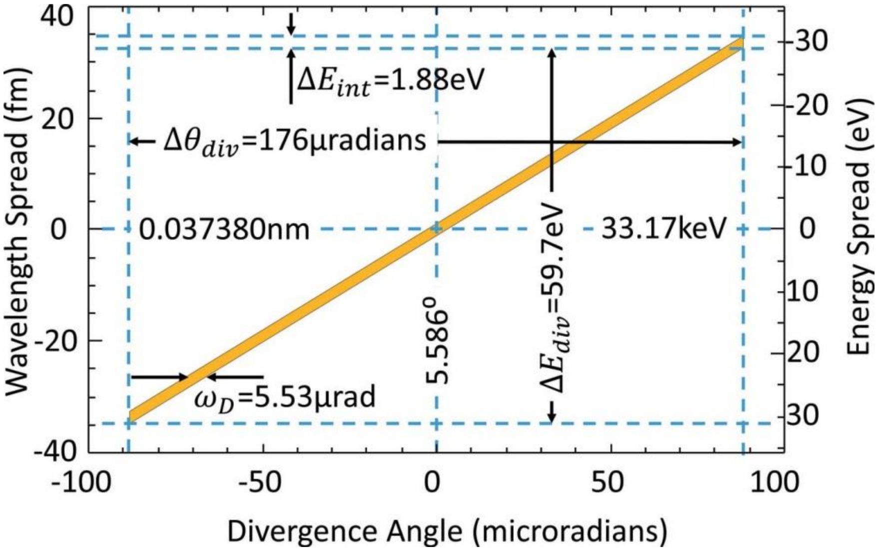

Figure A- 3 DuMond Diagram for Si (2,2,0) at 33.17 keV for 1/γ vertical divergence. The energy and angular ranges are shown for both vertical divergence and intrinsic widths. The relatively large vertical divergence results in an energy range that easily covers the K-edge of iodine.

As an example, assume a vertical angle range for the CLS of 1/γ = 176 μrad. At 33.17 keV, the absorption edge of iodine, the Bragg angle is 5.586^0 for the silicon (2, 2, 0). We can estimate the range of wavelengths using the derivative of Bragg's law with respect to angle,

$$d\lambda = 2d_{hkl}cos\theta d\theta. \tag{A. 2}$$

For the conditions stated the wavelength spread is 6.73×10^{-5} nm centered at 0.03738 nm. The matching energy spread is 59.7 eV. Figure A- 3 is a graphical representation, a DuMond diagram [31], of Bragg's law in the vicinity of the iodine K-edge.

There is also an energy or wavelength spread due to the finite reflectivity width of the dispersion curve. For diffraction, the energy or wavelength bandwidth is a fixed quantity away from absorption edges of the crystal. For silicon (2,2,0) the bandwidth is 56.6×10^{-6}. Thus the intrinsic wavelength spread is 2.12×10^{-6} nm and the intrinsic energy spread is 1.88 eV. This

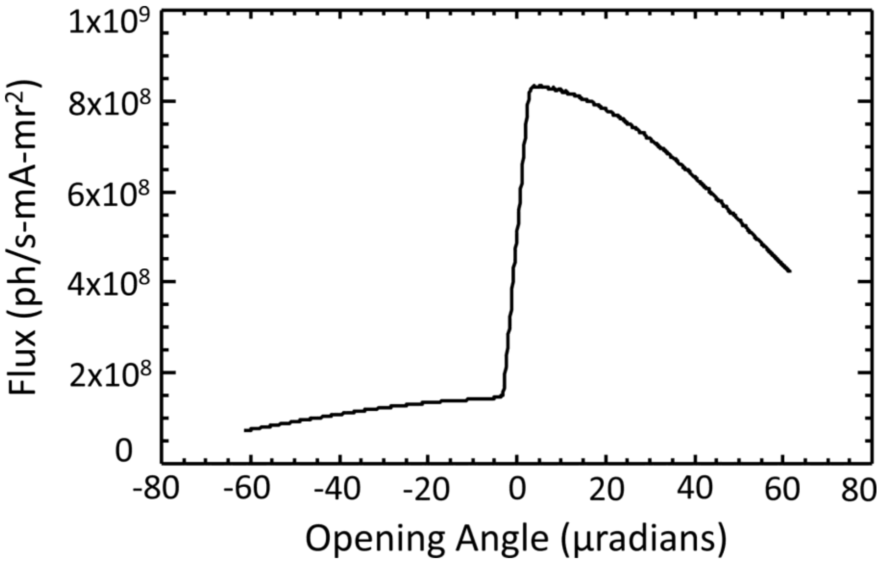

Figure A- 4 Calculated flux through a 60 mg cm^2 iodine filter from a Si (2, 2, 0) DCM at 33.17 keV on a CLS bend-magnet beamline.

wavelength and energy spread is also shown in Figure A- 3. The energy spread due to divergence is almost 32 times that of the intrinsic energy spread.

Schematically, the effect of an iodine filter on the transmitted beam of a DCM set at 33.17 keV is shown in Figure A- 2(c). Note that the spectral content of the beam vertically increases in energy from the bottom of the beam to the top. When the middle energy of that beam is placed at the iodine K-edge then the top of the beam will be absorbed more than the bottom creating an asymmetric beam profile shown on the right side of the figure. A calculation of the beam shape including the DuMond dispersion effects is shown in Figure A- 4.

A.3 WHAT HAPPENS WHEN THE BEAM MOVES?

A.3.1 Unfiltered side of the beam

When the photon beam moves at the source location the monochromatic beam after the DCM is sensitive to the motion. If the source point moves up then the beam measured at the detector location will also move up by the same amount. If the beam moves in vertical angle then the beam at the detector position will move by the product of the angle times the distance from the source to the detector. This effect is shown schematically in Figure A- 5(a) - Figure A- 5(d) in the 'Beam' column. The combination of vertical beam motion and angle is shown below in Equation (A. 3);

$$y_d = y + Dy', \tag{A. 3}$$

where y_d is the measured vertical beam position at the imaging detector, y is the vertical position of the electron beam source, y' is the vertical angle of the electron beam source and D is the distance from the source to the detector.

A.3.2 K-edge filtered side of the beam

The K-edge of an element is a fixed energy and can be used to locate of that energy in the photon beam; energies above the edge will be heavily absorbed and energies below the edge will not. If the source moves vertically the location of the K-edge will move the same amount at the detector. This is because the vertical energy distribution of the photon beam is not altered by this motion. If instead the beam at the source moves in vertical angle the location of the edge will not move. In this case the vertical photon beam distribution is changed by the DCM but the vertical location of the K-edge at the detector will not move because the angle is set by the monochromator. Therefore the location of the K-edge is a direct measure of the location of the source vertically. This effect is shown schematically in Figure A- 5(a) - Figure A- 5(d) in the "Edge" column. The location of the edge measured at the detector is then simply

$$y_c = y, \tag{A. 4}$$

where y_c is the measured vertical K-edge location and y is the vertical position of the electron beam source. Changes in the vertical source angle do not change the location of the K-edge at the detector.

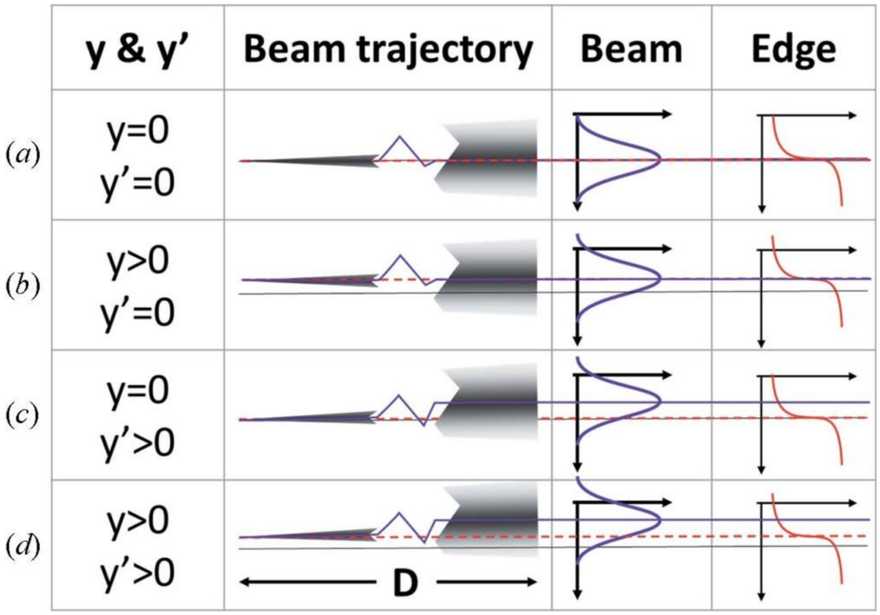

Figure A- 5 Schematic showing the effects of the electron beam position and angle displacements. The first column gives the position and angle, the second column is a schematic of the beam where the monochromator has been removed for clarity, the third and fourth columns show the beam and edge profile, respectively. The black line in each row represents the electron beam position and angle zeros, the purple line shows the centroid of the beam, the red dashed line shows the location of the same angle to the monochromator crystal or the edge location. (a, c) At $y = 0$. (a, b) At $y' = 0$. (b, d) At $y > 0$. (c, d) At $y' > 0$.

A.4 DETERMINING THE ELECTRON SOURCE VERTICAL POSITION AND ANGLE

We are now in a situation to be able to independently determine the vertical electron beam position and angle by measuring the beam location through a DCM without a filter (beam side) and the edge location with a K-edge filter in place (edge side). Using the Equations (A. 3) and (B. 1),

$$y = y_c \;\;\&\;\; \mathrm{y}' = \frac{y_d - y_c}{D} \tag{A. 5}$$

It should be noted that changing the monochromator energy has the effect of changing the source position, y_c. Also changing the detector's vertical position will alter the y_d value. Both have a direct impact on the calculated electron beam position and angle, y and y'. Thus the system measures relative values of position and angle and must be calibrated to obtain absolute values.

The ability to determine the location of the beam centroid, y_d, and the K-edge, $\mathrm{y_c}$, are integral to the success of this method. A fitting procedure will be used to determine the location of each. To be properly fit there needs to be sufficient intensity, detector resolution and vertical size to encompass the profile along with any vertical motion that may occur. The vertical beam size at the detector is a relatively weak function of the energy selected by the monochromator. However, the reflection chosen in the monochromator may have a strong effect on the intensity since the reflection sets the monochromator bandwidth.

In addition, the ability to determine y_c will also depend on the width of the K-edge and the thickness and density of the contrast filter. A rough estimate of the optimal projected iodine filter density was found to be ~70 mg/cm^2 by numerical simulation. This estimate was based on a contrast to noise model using Poisson statistics.

The width of the transmitted K-edge with the DCM will depend on the intrinsic K-edge width for the contrast element (~15 eV for iodine [32]). The K-edge will also be blurred by the intrinsic energy width of the monochromator (1.88 eV as discussed above for the Si (2,2,0) at 33.17 keV), and will also be dispersed vertically, z, across the detector approximately as,

$$\frac{dz}{dE} = \frac{tan\theta}{E} D, \tag{A. 6}$$

where θ is the Bragg angle and E is the K-edge energy. For the silicon (2,2,0) at the iodine K-edge this spatial dispersion is 74 μm eV^{-1}. Therefore, the 15 eV of energy spread will correspond to a spatial width of 1.1 mm.

When compared with the silicon (4,4,0) under similar conditions the spatial dispersion at 33.17 keV will change to 150 μm eV^{-1} and the 15 eV energy spread will correspond to a width of ~2.2 mm which indicates the increased spatial dispersion sensitivity. But this sensitivity will come with a loss of intensity of over a factor of six due to the decreased (4,4,0) bandwidth (9.1×10^{-6}) compared with the (2,2,0) bandwidth (56.6×10^{-6}) and therefore, for the of the measurements, we chose silicon (2,2,0) .

A.5 IMPLEMENTATION AT BMIT

The experiments for this project where performed at the CLS BMIT bend magnet beamline 05B1-1. A silicon (2,2,0) and (4,4,0) double crystal monochromator was tuned to the iodine K-edge at 33.17 keV. The vertical dispersion of the monochromator allows an energy range that covers the K-edge of iodine. Figure A- 5(a) - Figure A- 5(c) show schematically how the system was implemented in the beamline with a plan view at the top. In this system the beam was split horizontally in two parts: one side with 60 mg cm^{-2} iodine filter and the other side with no filter. A Hamamatsu flat-panel detector with 0.1 mm pixel size was used to collect data. Measurements were made in the POE-2 hutch, which was ~25 m away from the source.

Two types of measurements were performed. One type was made during the normal operational mode to assess the beam stability. A second type was made during special shifts were the synchrotron beam was intentionally moved at the source location with specific vertical, horizontal and angular offsets. This second type was used to assess, in part, the sensitivity of the system and to independently measure the motions made to the electron beam source in the ring.

Data were in the form of images of the split beam with the iodine filter on one side and no filter on the other. Sets of 400 data images were saved into individual directories and a measurement set might range from a few to several hundred directories. It took around 12 s to

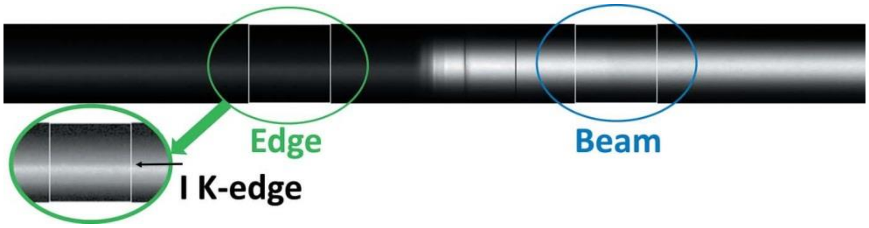

Figure A- 6 Example data image. Regions are chosen from both image types for beam and edge analysis. The edge region is enhanced in the lower left corner to better show the K-edge whose location is indicated by the arrow.

collect 400 images for each directory and roughly 1 min dead-time to save the data to the disk. For each set of measurements, ten dark images (the detector response without beam) and ten flat images (no contrast agent in the beam) were also collected for data normalization. These ten images were averaged to form single ‘dark’ and ‘flat’ images.

A.6 DATA ANALYSIS METHOD

To analyze the data, several procedures were written in IDL [Interactive Data Language, ITT Visual Information Solutions, Boulder, CO, USA]. Regions for the unfiltered beam side and the K-edge side were selected from the data and each side was corrected for dark response. An example of the regions chosen from the images is shown in Figure A- 6.

The beam side from the data was used to determine y_d which was found by fitting the horizontally averaged vertical beam profile using a Gaussian function. An example of this fitting was shown in Figure A- 1. The vertical direction in the detector, z, was measured in terms of detector pixels that can be easily converted into micrometers using the pixel size. The vertical center of the detector was the origin used in this part of the analysis.

The horizontally averaged edge side profile was normalized by the matching region from the flat to form an I/I_0 profile. However, the flat was corrected for vertical beam motion by using the beam side of the data to vertically move the flat prior to normalization. The low-intensity

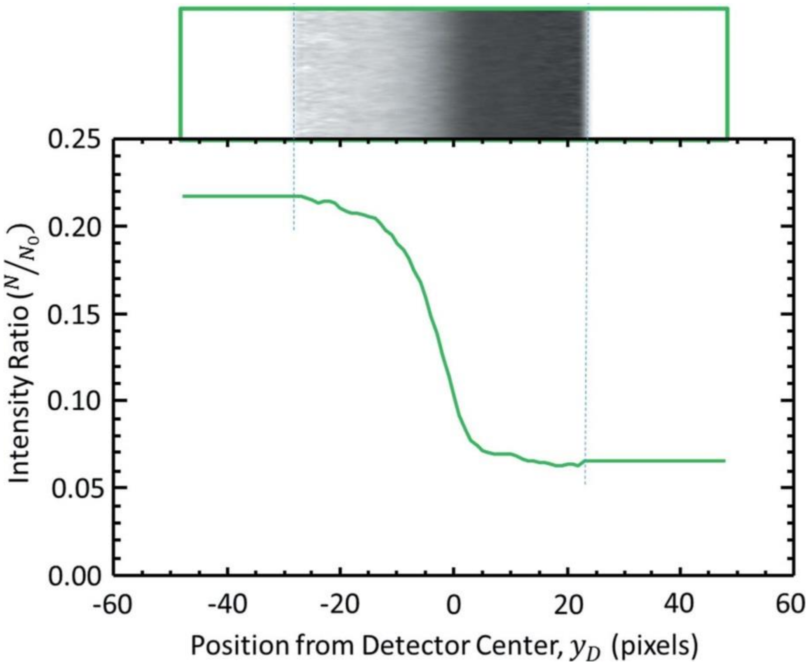

Figure A- 7 Summed normalized K-edge image across the sampling width; 100 pixels in this case. The horizontal axis is in pixels and the origin is referenced to the vertical middle of the detector

regions of this corrected flat were ignored using a threshold value and not used in the analysis. An example of this is shown in Figure A- 7.

A number of fitting algorithms were used to find the location of the K-edge in the filtered beam profile. In general, three types of functions were investigated to fit the edge: Gaussian, Lorentzian and Voigt. These functions were chosen because they are mathematically simple and make physical sense. The functions were used directly to fit the derivative of the K-edge profile, and integrated versions of each were used to fit the measured edge profile directly. Finally the K-edge could be fit to the I/I_0 values or the negative logarithm of the I/I_0 values. Of the 12 fit types the Gaussian fit to the derivative of the negative logarithm of the profile was chosen due to its simplicity and the robustness of the fit. For this analysis the main parameter of interest in the fit

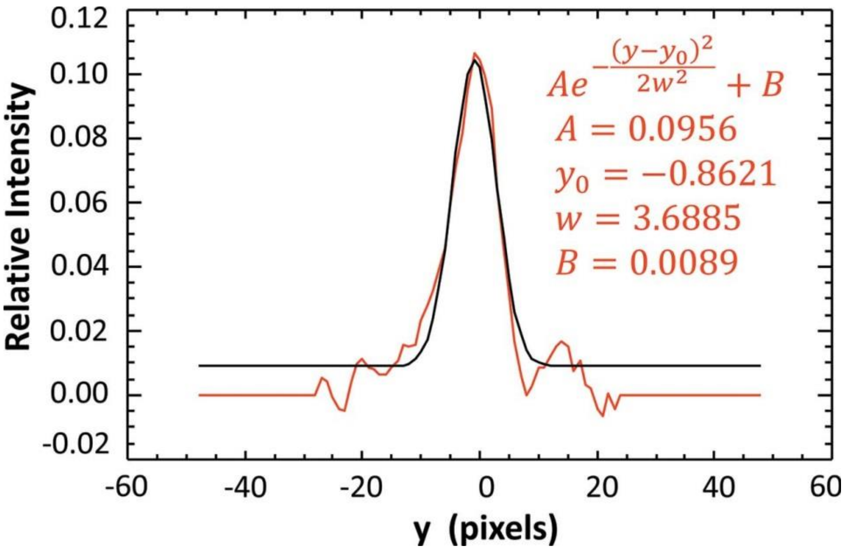

Figure A- 8 Derivative of the negative logarithm of the profile shown in Figure A- 6. The Gaussian fit parameters are shown in the upper right-hand corner. For this analysis only y_0 or the peak center is used.

was the transition center location. Other parameters determined in the fit were the amplitude, width and the background values. Figure A- 8 shows a fit to one of the data points.

A.7 RESULTS AND DISCUSSION

A number of measurements have been taken with the system. In total, eight shifts (1 shift = 8 h) have been used for beam motion measurements. These shifts were during normal operations shifts and by special request shifts when the ring parameters can be altered. During the special machine study shifts the electron beam was moved and measurements were made to assess the response of the system.

A.7.1 System Response to Electron Beam Motions

The electron beam position and angle were varied in the machine study shifts. To move the electron beam in the BMIT sector, electron BPM (eBPM) target values were changed. This change in target value moves the electron beam orbit using dipole steering magnets. The eBPMs

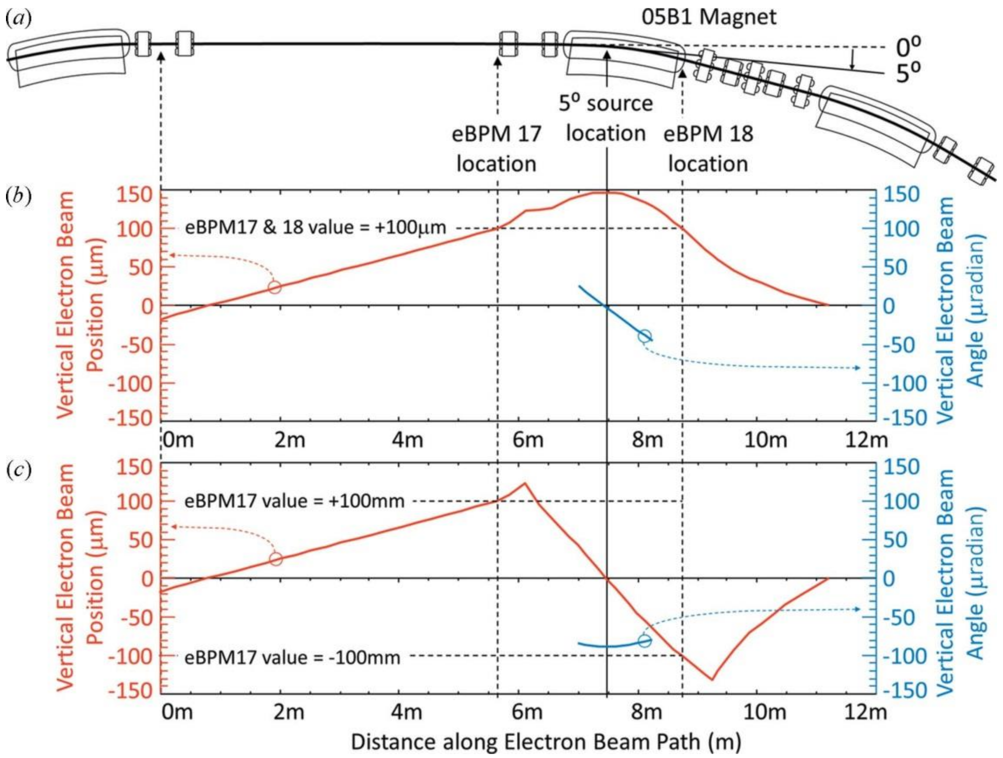

Figure A- 9 Storage ring schematic and calculated electron beam trajectories. (a) Section of the storage ring around the 05B1 magnet from which the measurements were made. The locations for eBPM17, eBPM18 and 5° source are indicated. The calculated trajectory for +100 µm vertical position for eBPM17 and eBPM18 are shown in (b) with the electron vertical position in red and angle in blue. (c) Trajectory for a +100 µm value at eBPM17 and -100 µm at eBPM18 which mostly creates an angle at the source location.

numbered 17 and 18 are located on the upstream and downstream sides of the bend magnet which is our photon beam source (see Figure A- 9). The photon beam source is 5° into 15° bend. Since we observe the photon beam source point at an intermediate location between the two eBPMs, there can be small differences in the electron beam vertical position and angle due to the storage ring magnetic optics.

A.7.1.1 Electron Beam Vertical Position Measurements

For vertical motion the eBPM 17 and eBPM 18 target values were changed by the same amount. The beam was moved vertically between +100 and −100 µm in 0, ±1, ±2, ±5, ±10, ±20, and ±100 μm increments. Examples are shown were the beam is at the zero location (Figure A- 10(a)), +100 μm (Figure A- 10(b)), and −100 μm (Figure A- 10(c)). In those plots 12 s of beam motion is shown. It should be noted that the measured beam position and angles are relative to the middle of the detector. Three data lines are shown, red, which is the measured electron beam position, y; blue, the electron beam angle multiplied by the distance from the source to the detector, Dy' (this allows it to be plotted on the same scale as the position); and purple, the overall beam position, $y+Dy'$.

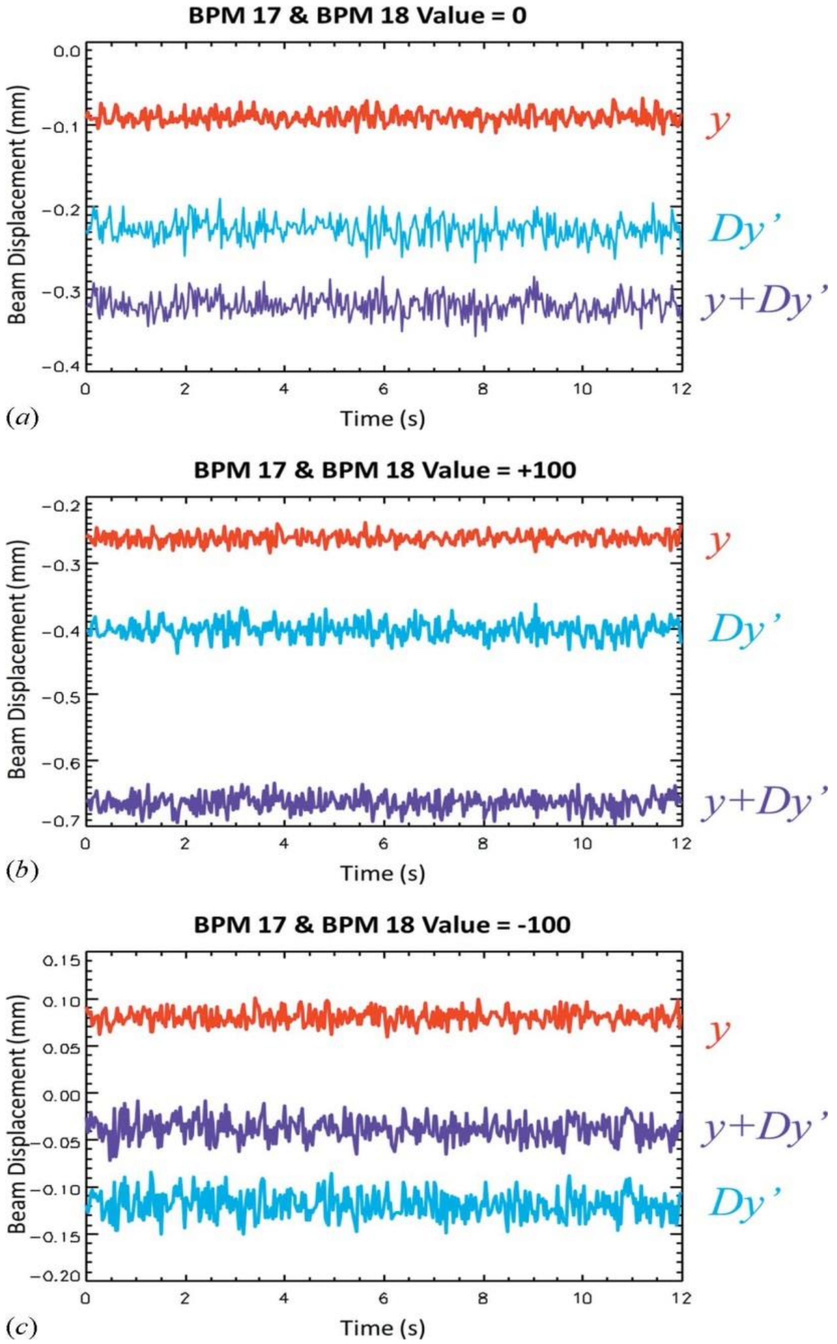

Figure A- 10 Measurements of the beam vertical position, *y*, the effect of vertical angle, *Dy'*, and combined motion as a function of time for eBPM17/18 values of 0 (a), +100 (b) and -100 (c). The vertical motions have been translated into millimeters using the 100 μm pixel size. The vertical zero is the vertical detector center.

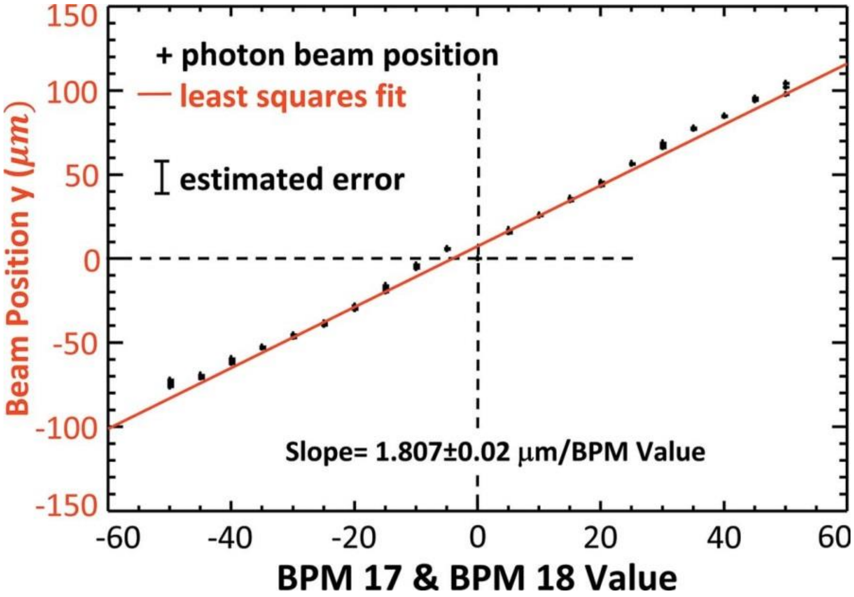

Figure A- 11 Electron vertical beam position in micrometers measured as the eBPM17 and 18 are changed from -50 to +50 μm.

Trends plots of the electron beam position and angle measurements as a function of eBPM offset values are shown in Figure A- 11 and Figure A- 12, respectively. Some selected values are also given in Table A- 1. The dashed horizontal line in the figures identifies the measured ‘zero’ location where the electron beam is at the zero location in eBPM units. Clearly, there is good correlation between the eBPM values and the beam position and angle. The red line in Figure A- 11 and the blue line in Figure A- 12 are least-squares fits to the measured data. For these data, 150 twelve second measurements (called a “slice”) were made as the beam was moved. For each beam location between four and five slices were taken. In reviewing Table A- 1, the measured standard deviations are in the 10 micron range for y, *Dy’* and *y+Dy’*.

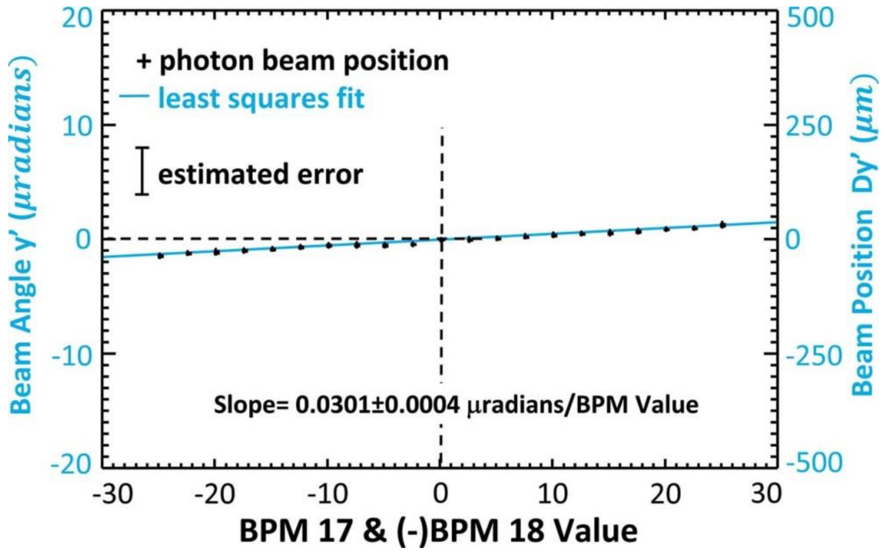

Figure A- 12 Electron beam vertical angle in microradians measured as the eBPM17 and 18 are changed from -50 to +50 μm. The measured angle in microradians is shown on the left axis and the vertical displacement that angle creates at the detector position, *Dy'*, is shown on the right.

Table A- 1 Selected measured electron vertical beam position, *y*, and angle, *y'*, as a function of vertical electron beam motion defined by equal eBPM 17 and 18 values.
The slice number identifies the measurement. Columns showing the effect of the electron beam angle on beam position, *Dy'*, and the overall vertical beam motion, *y+Dy'* at the detector, are given along with calculated standard deviations. Each slice corresponds to 12 seconds of acquisition time.

Slice #	BPM 17/18 (μm)	$\overline{y}$ (μm)	$\overline{y'}$ (μrad)	$D\overline{y'}$ (μm)	$\overline{y} + D\overline{y'}$ (μm)
2	0	-401 ± 8	5.89 ± 0.54	146 ± 13	-255 ± 12
82	5	-385 ± 8	6.01 ± 0.56	150 ± 14	-235 ± 12
95	10	-375 ± 8	6.07 ± 0.52	152 ± 13	-223 ± 13
92	20	-356 ± 8	6.34 ± 0.53	158 ± 13	-198 ± 12
99	30	-334 ± 8	6.64 ± 0.55	165 ± 14	-168 ± 13
105	40	-316 ± 8	7.02 ± 0.54	175 ± 14	-141 ± 13
113	50	-297 ± 8	7.34 ± 0.53	190 ± 13	-107 ± 12
121	-5	-396 ± 8	5.45 ± 0.51	136 ± 13	-259 ± 13
125	-10	-406 ± 8	5.34 ± 0.52	133 ± 13	-272 ± 12
133	-20	-430 ± 8	5.24 ± 0.55	131 ± 14	-299 ± 12
139	-30	-448 ± 8	4.97 ± 0.53	124 ± 13	-324 ± 12
146	-40	-461 ± 8	4.52 ± 0.52	113 ± 13	-348 ± 12
153	-50	-467 ± 8	4.16 ± 0.53	103 ± 13	-372 ± 11

From Figure A- 11, the vertical beam position rate of change was determined to be 1.807 ± 0.02 µm per µm eBPM value from the least-squares fit. From Figure A- 12, the vertical beam angle rate of change was similarly determine to be 0.0301 ± 0.0004 µrad per µm eBPM value. Based on electron beam optics calculations for an ideal machine, the predicted values should be 1.47 µm per µm eBPM value and -0.034 µrad per µm eBPM value, respectively. The good agreement between the experimentally determined and calculated values is shown in the top row of Table A- 2.

Table A- 2 Measured and calculated detector response to vertical electron beam position and angle. Vertical electron beam positions where eBPM17 and 18 are equal are shown in the upper two rows (upper row – measured and lower row – calculated). Vertical beam angle where eBPM17 is equal to, but opposite sign to eBPM18 is shown in the bottom two rows. At the measurement location there is a mixture of position and angle for both types of electron beam motion.

		Position ($\mu rad/\mu m$ offset)	**Angle ($\mu rad/\mu m$ offset)**
Position Motion	Measured	1.807±0.02	0.0301±0.0004
(eBPM17=eBMP18)	Calculated	1.47	-0.034
Angle Motion	Measured	-0.101± 0.039	-0.842±0.005
(eBPM17= - eBPM18)	Calculated	-0.06	-0.88

A.7.1.2 Electron Beam Vertical Angle Measurements

Similar measurements were made when the eBPM values were changed asymmetrically to create electron beam angle at the beamline. Tests were made with eBPM offsets between +20 and −20 µm in 0, ±5, ±10, ±15, and ±20 increments.

Plots of the electron beam position and angle as a function of eBPM values are shown in Figure A- 13 and Figure A- 14, respectively. Some selected values are also given in Table A- 3 and, as before, the measured standard deviations are in the 10 µm range for *y*, *Dy'* and *y* + *Dy'*. The dashed horizontal line in the figures identifies the measured zero location where the electron

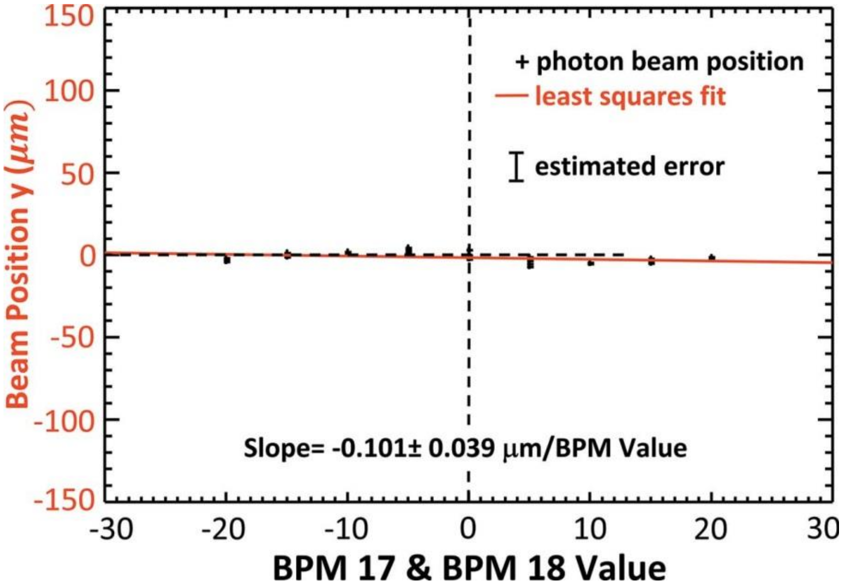

Figure A- 13 Electron vertical beam position in micrometers measured as the eBPM17 and -18 are changed from -20 to +20 μm.

beam is at the zero location in eBPM units. The red line in Figure A- 13 Electron vertical beam position in micrometers measured as the eBPM17 and -18 are changed from -20 to +20 μm. Figure A- 13 and the blue line in Figure A- 14 are least-squares fits to the measured data.

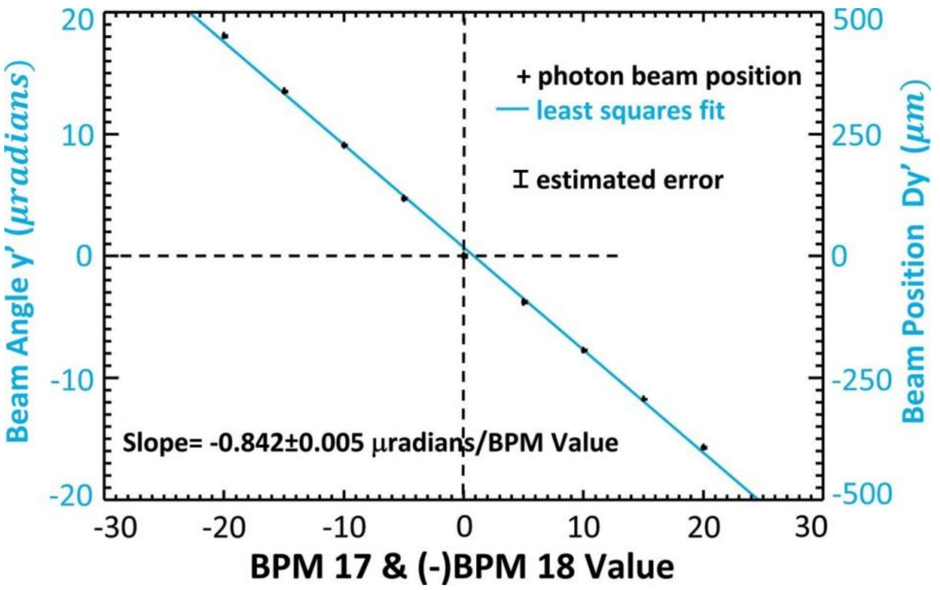

Figure A- 14 Electron beam vertical angle in microradians measured as the eBPM17 and -18 are changed from -20 to +20 µm. The measured angle in microradians is shown on the left axis and the vertical displacement that angle creates at the detector position, *Dy'*, is shown on the right.

The measured and calculated beam responses are summarized in the lower half of table A-2. Again, there is a good agreement between the measured and ideal machine values.

Table A- 3 Selected measured electron vertical beam position, *y*, and angle, *y'*, as a function of electron beam angle defined by equal and opposite sign eBPM 17 and 18 values; the remainder of the table is for *Dy'* and *y+Dy'* as defined in Table A- 1 and in the text.

Slice #	**BPM 17/18 (µm)**	$\bar{y}$ **(µm)**	$\bar{y}'$ **(µrad)**	$D\bar{y}'$ **(µm)**	$\bar{y} + D\bar{y}'$ **(µm)**
9	5	-428 ± 8	2.30 ± 0.55	57± 14	-371 ± 14
13	10	-430 ± 8	-1.64 ± 0.51	-41 ± 13	-471 ± 13
20	20	-427 ± 8	-9.63 ± 0.51	-241 ± 13	-667 ± 12
47	-5	-421 ± 8	10.70 ± 0.57	267 ± 14	-154 ± 13
51	-10	-423 ± 8	15.09 ± 0.51	377 ± 13	-46 ± 13
58	-20	-428 ± 8	24.16 ± 0.58	604 ± 15	176 ± 13

A.7.2 Normal Operations Measurements

Measurements with ps-BPM system were made during a number of normal operation shifts between December 2013 and August 2014. During the December 2013 to early 2014 period the CLS storage ring was experiencing beam instabilities from a storage ring dipole magnet power supply.

Figure A- 15 shows 12 s measurements made during three operational periods in December 2013, March 2014 and August 2014. The top line is the measured electron beam position, *y*, the bottom line is the vertical displacement due to angle, *Dy'*, and the middle line is the sum of two, *y*+*Dy'*. Each of the three measurement periods are show side by side in the figure. The offsets for the three position types have been removed so that their average is zero to make the comparison easier.

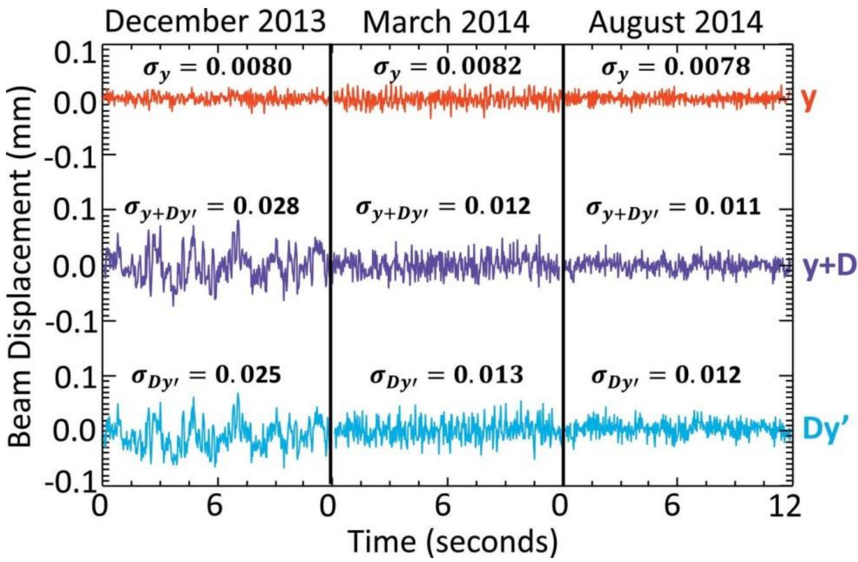

Figure A- 15 Beam phase-space measurements over a 12 s interval during normal operations for three dates: December 2013, March 2014 and August 2014. The top line is the zero referenced electron beam position, *y*, the bottom line is the vertical displacement due to angle, *Dy'*, and the middle line is the sum of the two, *y* + *Dy'*. Note the improvement in beam stability over the nine-month period. The standard deviation values are shown above each period.

It is clear that the ring stability improved dramatically during that time period and that the instability measured arose primarily from the angle displacements. The Figure A- 15 also shows measured standard deviations of the positions, σy, σDy', and σy+Dy'. The standard deviation of the electron beam position, σy, varied little over the three periods. However, the standard deviation of the vertical displacement due to angle, σDy', dropped by a factor of two in the same time. The standard deviation of the overall beam displacement due to electron beam positon and angle, σy+Dy', is determined mostly by the electron beam angle.

The DCM could be responsible for some of the measured beam motion due to vibrations and thermal motion. Internal vibrations within the monochromator are somewhat minimized as we used a gravity flow water system for cooling both crystals in the DCM. Also the use of a copper and aluminum filter dropped the incident power on the first crystal to below 2 W for the size of the beam and ring current used for the experiments. Finally, based on our measurements, as the beam is moved in the machine the error bar on the beam displacement was typically less than 10 μm and the angle less than 0.5 μrad, indicating that the combination of the monochromator and electron beam motions must be less than these values.

A.8 PRACTICAL IMPLEMENTATION OF A PS-BPM

All of the proof-of-principle measurements required the use of the entire beamline and as such would be completely impractical as a monitor. Probably the most challenging aspect of implementing such a monitor would be the dedicated use of the DCM. The complexity of the DCM in which the two crystals must be maintained in sub-microradian alignment in the Bragg geometry could be mitigated by the use of a single-crystal Laue or transmission-type monochromator. The Laue-type monochromator is not so susceptible to crystal heating effects as there is no thermal bump on the crystal's surface. Much of the power can be transmitted through where it can be absorbed elsewhere. The width of the beam being used need not be very wide as two line detectors can be used for the beam and K-edge side measurements. A prototype Laue-type system is being designed.

A.9 CONCLUSIONS

A unique method for simultaneously measuring the vertical position and angle (phase space) of synchrotron photon beams using the combination of x-ray diffraction and absorption edges has been developed and tested at the BMIT beamline at the Canadian Light Source. This system allows the measurement of the photon beam centroid in phase space, and thus the electron beam position and angle, at a single location along the beamline. Temporal stability and beam motion system response measurements have been performed with good results.

The sensitivity of this system is comparable to other photon beam position monitors with detectable position errors on the scale of 10 μm and angle errors of 0.5 μrad. These errors are based on the noise level in the 12 s time measurements of 400 time points.

We are optimistic that a compact dedicated system employing a single transmission or Laue monochromator coupled with a K-edge filter and two line detectors can be built and implemented to make a practical device that uses a small piece of the horizontal width of a bend-magnet or wiggler white beam.

Such a system provides more complete view of beam motion in a synchrotron source and may be used to improve the synchrotron source position and angle stability. The ps-BPM also provides a better diagnostic should instabilities or beam drift occur, and could be used to correct experimental data for beam motion and to actively control the trajectory of the photon beam in the beamline.

A.10 ACKNOWLEDGEMENT

The authors acknowledge the financial support of Canadian Institutes of Health Research (CIHR) Training Grant - Training in Health Research Using Synchrotron Techniques (NS, MM, BB), Saskatchewan Health Research Foundation Team Grant (NS, DC), Natural Sciences and Engineering Research Council of Canada (NSERC) Discovery Grant (DC), the University of Saskatchewan (NS, MM), and Canada Research Chair Program (DC). Research described in this paper was performed at the Canadian Light Source, which is funded by the Canada Foundation for Innovation, NSERC, the National Research Council Canada, CIHR, the Government of Saskatchewan, Western Economic Diversification Canada, and the University of Saskatchewan.

A.11 REFERENCES

1. Brefeld, W., Stabilization of synchrotron radiation beam at HASYLAB (invited). Review of Scientific Instruments, 1989. **60**(7): p. 1513-1516.
2. K. Haga, et al. The Vibration Measurements at the Photon Factory Storage Ring Building. in European Particle Accelerator Conference. 2000. Vienna, Austria.
3. Galimberti, A. and R. Borghes, Operational Experience with the Photon Beam Position Monitor for Undulator Beamlines of Elettra. AIP Conference Proceedings, 2004. **705**(1): p. 584-587.
4. Rehm, G., Achieving and Measuring Sub-Micrometer Beam Stability at 3rd Generation Light Sources. Journal of Physics: Conference Series, 2013. **425**: p. 042001.
5. Hettel, R., Review of synchrotron beam stability and stabilizing systems (invited). Review of Scientific Instruments, 1989. **60**(7): p. 1501-1506.
6. Bocchetta, C.J. Lifetime and beam quality. in CAS - CERN Accelerator School 1996. Grenoble, France.
7. Farvacque, L. Beam Stability. in CAS - CERN Accelerator School. 1996. Grenoble, France.
8. Hettel, R.O., Beam stability at light sources (invited). Review of Scientific Instruments, 2002. **73**(3): p. 1396-1401.
9. Billing, M.G., Beam position monitors for storage rings. Nuclear Instruments and Methods in Physics Research Section A: Accelerators, Spectrometers, Detectors and Associated Equipment, 1988. **266**(1–3): p. 144-154.
10. Izumi, T., T. Nakajima, and T. Kurihama, Photon beam position monitor. Review of Scientific Instruments, 1989. **60**(7): p. 1951-1952.
11. Johnson, E.D. and T. Oversluizen, Compact high flux photon beam position monitor. Review of Scientific Instruments, 1989. **60**(7): p. 1947-1950.
12. van, R., A high-precision X-ray beam-position and profile monitor for synchrotron beamlines. Journal of Synchrotron Radiation, 1999. **6**(6): p. 1071-1075.
13. Alkire, R.W., G. Rosenbaum, and G. Evans, Design of a vacuum-compatible high-precision monochromatic beam-position monitor for use with synchrotron radiation from 5 to 25 keV. Journal of Synchrotron Radiation, 2000. **7**(2): p. 61-68.
14. Kyele, N.R., K. Decanniere, and R.G. van Silfhout, A transparent two-dimensional in situ beam-position and profile monitor for synchrotron X-ray beamlines. Journal of Synchrotron Radiation, 2005. **12**(6): p. 800-806.
15. Bunk, O., et al., X-ray beam-position monitoring in the sub-micrometre and sub-second regime. Journal of Synchrotron Radiation, 2005. **12**(6): p. 795-799.

16. Bergonzo, P., D. Tromson, and C. Mer, CVD diamond-based semi-transparent beam-position monitors for synchrotron beamlines: preliminary studies and device developments at CEA/Saclay. Journal of Synchrotron Radiation, 2006. **13**(2): p. 151-158.

17. Ilinski, P., et al., Residual Gas X-ray Beam Position Monitor Development for PETRA III. AIP Conference Proceedings, 2007. **879**(1): p. 782-785.

18. Tucoulou, R., et al., High-resolution angular beam stability monitoring at a nanofocusing beamline. Journal of Synchrotron Radiation, 2008. **15**(4): p. 392-398.

19. Leban, P., D. Tinta, and C. Pradervand. Photon Beam Position Measurements using CVD Diamond based Beam Position Sensor and Libera Photon at Swiss Light Source. in International Particle Accelerator Conference. 2010. Kyoto, Japan.

20. Revesz, P., A.B. Temnykh, and A.K. Pauling, New X-ray beam position monitors with submicron resolution utilizing imaging of scattered X-rays at CHESS. Nuclear Instruments and Methods in Physics Research Section A: Accelerators, Spectrometers, Detectors and Associated Equipment, 2011. **649**(1): p. 94-96.

21. Xiao, Y., et al., Development of a PSD-based photon beam position measurement system. Nuclear Science and Techniques, 2012. **23**: p. 70-74.

22. Muller, E.M., et al., Transmission-mode diamond white-beam position monitor at NSLS. Journal of Synchrotron Radiation, 2012. **19**(3): p. 381-387.

23. Cheng, X.C., et al., V-coupling-blades beam position monitor for NSRL undulator source. Journal of Physics: Conference Series, 2013. **425**.

24. Kachatkou, A. and R. van Silfhout, On the resolution and linearity of lensless in situ X-ray beam diagnostics using pixelated sensors. Opt Express, 2013. **21**(4): p. 4291-302.

25. Hahn, U., et al., Beam-position monitors in the X-ray undulator beamline at PETRA. Journal of Synchrotron Radiation, 1998. **5**(3): p. 627-629.

26. Kyele, N.R., et al., In situ synchrotron x-ray photon beam characterization. Journal of Applied Physics, 2007. **101**(6): p. 064901.

27. Morse, J., B. Solar, and H. Graafsma, Diamond X-ray beam-position monitoring using signal readout at the synchrotron radiofrequency. Journal of Synchrotron Radiation, 2010. **17**(4): p. 456-464.

28. Bergstrom, J.C. and J.M. Vogt, The optical diagnostic beamline at the Canadian Light Source. Nuclear Instruments and Methods in Physics Research Section A: Accelerators, Spectrometers, Detectors and Associated Equipment, 2006. **562**(1): p. 495-512.

29. Thompson, A., X-Ray Data Booklet, D.o. Energy, Editor. 2009, Lawrence Berkely Laboratory: Berkeley, CA USA.

30. Golovchenko, J.A., R.A. Levesque, and P.L. Cowan, X-ray monochromator system for use with synchrotron radiation sources. Review of Scientific Instruments, 1981. **52**(4): p. 509-16.

31. DuMond, J.W.M., Successive x-ray crystal reflections to obtain increased resolving power. Physical Review, 1937. **52**: p. 872-883.

32. Feiters, M.C., F.C. Kupper, and W. Meyer-Klaucke, X-ray absorption spectroscopic studies on model compounds for biological iodine and bromine. Journal of Synchrotron Radiation, 2005. **12**(1): p. 85-93.

APPENDIX B

This paper was published in the JACoW publishing as the proceedings of the 7th International Beam Instrumentation Conference held in Shanghai, China in September 2018. (doi:10.18429/JACoW-IBIC2018-TUOB04).

The author took all the data and did all of the data analysis. The author arranged for the beamtime and coordinated data acquisition with the beam motion studies. Others were involved in the storage ring properties and predicted beam motions (Dallin) and algorithm development (Chapman). The author and Prof. Chapman prepared the manuscript draft which was reviewed by the other co-other.

A VERTICAL PHASE SPACE BEAM POSITION AND EMITTANCE MONITOR FOR SYNCHROTRON RADIATION

Nazanin Samadi[a]*, Les Dallin[b], Dean Chapman[b,c]
[a]Physics and Engineering physics, University of Saskatchewan, 116 Science Place, Saskatoon, SK, S7N 5E2 Canada
[b]Canadian Light Source, 44 Innovation Boulevard, Saskatoon, SK, S7N 2V3, Canada
[c]Anatomy and Cell Biology, University of Saskatchewan, 107 Wiggins Rd, Saskatoon, SK, S7N 5E5, Canada
Correspondence email: nazanin.samadi@usask.ca

B.1 ABSTRACT

We report on a system (ps-BPM) that can measure the electron source position and angular motion at a single location in a synchrotron bend magnet beamline using a combination of a monochromator and an absorber with a K-edge to which the monochromator was tuned in energy. The vertical distribution of the beam was visualized with an imaging detector where horizontally

one part of the beam was with the absorber and the other part with no absorber. The small range of angles from the source onto the monochromator crystals creates an energy range that allows part of the beam to be below the K-edge and the other part above. Measurement of the beam vertical location without the absorber and edge vertical location with the absorber gives the source position and angle.

Measurements were made to investigate the possibility of using the ps-BPM to correct experimental imaging data. We have introduced periodic electron beam motion using a correction coil in the storage ring lattice. The measured and predicted motions compared well for two different frequencies.

We then show that measurement of the beam width and edge width gives information about the vertical electron source size and angular distribution.

B.2 INTRODUCTION

The stability of the photon beam which is dependent on the stability of the electron source in a synchrotron is critical and essential to the performance of the machine and the beamlines. It is becoming a more important issue as fourth generation storage rings are planned and coming alive and as many other facilities are upgrading their existing rings. The fourth-generation light sources are pushing to very low emittance, so the stability of the electron beam becomes increasingly important as it has a direct effect on the emittance of the machine.

The vertical position of the photon beam at some distance from the source is determined by the vertical position and angle of the electron beam.

We have developed a method to measure the vertical position and angle of the synchrotron electron beam at a single location in a bend magnet beamline at the Canadian Light Source (CLS). The discovery of this system came during an imaging experiment at the Biomedical Imaging and

Therapy (BMIT) beamline [3-5] at CLS [1]. Normally to measure the beam angle, two measurements of the beam position at two separated distances from the source are required. This is a difficult task in a beamline due to both lack of space and presence of many beam-line optics and components that will interfere with the location and operation of beam position monitors.

The system we have developed relies on measurements of the photon beam profile with and without an absorption edge filter and at the same location in the beamline. In the initial experiments a Bragg type (re-flection geometry) Double Crystal Monochromator (DCM) [2] was used to prepare the photon beam at an energy of the filter's absorption edge.

In this paper we present the implementation and results of a system using (1) a single Laue monochromator setup which is compact and is less susceptible to beam power loading and thus energy drift. We have used this system to assess the ability to (2) measure periodic beam motion with the future intent of (3) using these measurements both to show some of the temporal features of the system and to use the beam position and angle measurements to correct experimental imaging data.

B.2.1 Synchrotron

The vertical photon distribution of a bend magnet or wiggler synchrotron beam can be well fitted with a Gaussian function for photon energies what are well above the critical energy of the device (see Figure B- 1c where the Gaussian center and width are shown). In our case, the critical energy of the CLS bend is 7.57keV and the absorption edge of the iodine filter is 33.17keV. Figure B- 1a shows the vertical spatial distribution of an imaging beam prepared by a Si (220) DCM at 25m from the source on the left side while the right side shows the effect of an iodine filter. The part in the red circle has been enhanced to show the edge. The edge is found by normalizing the

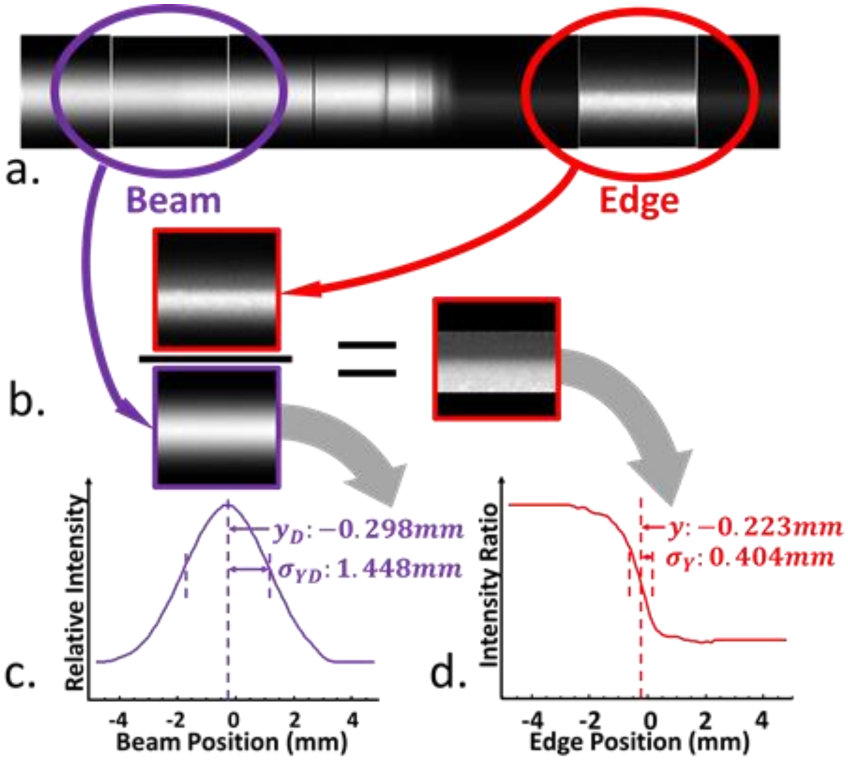

Figure B- 1 Beam and edge data (a) plus schematic representation of the data analysis steps (b,c,d).

filter side by the beam side. The result is shown in Figure B- 1d where the location and Gaussian width is found.

B.2.2 Diffraction, Dispersion and Absorption Edge

The vertical angular distribution of a synchrotron source will present a range of angles onto a crystal monochromator if there are not intervening optics be-tween the source and monochromator as in our case. The small range of angles will prepare a quasi-monochromatic beam that has a range of energies as determined by Bragg’s law. Thus, the beam prepared by the monochromator will have a continuous range of energies across the vertical range of angles (energy dispersion) from the source. At some distance, again 25m in our case, this range of angles corresponds to a spatial distribution. Thus, the distance scale in Figure B- 1 can also be interpreted as an energy scale. As an example, the energy range contained in our beams (reflection or

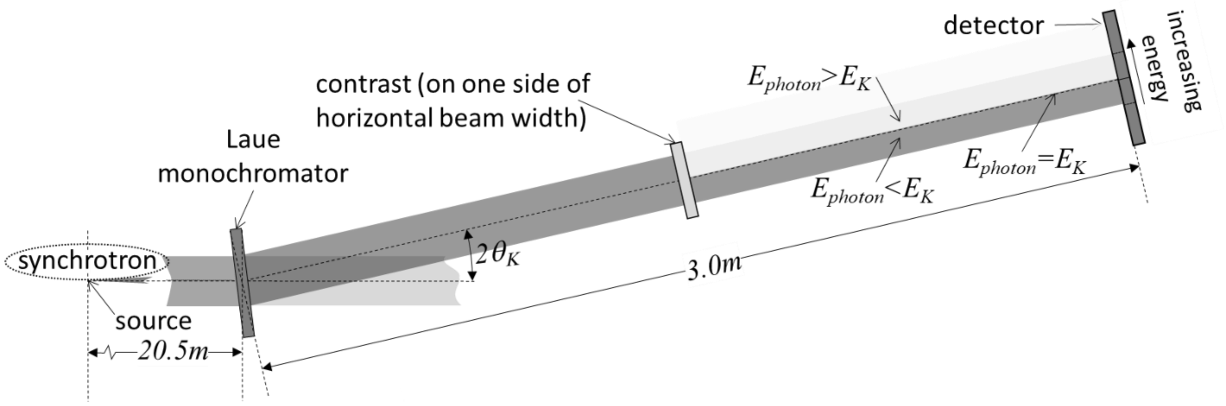

Figure B- 2 Schematic layout of the ps-BPM system for a single crystal Laue monochromator

transmission) is of the order of 50+eV at 33.17keV. This energy range is sufficient to easily cover the energy range of the absorption edge of the iodine filter which was used in these experiments.

B.3 THE SYSTEM

The experiments were done at the bend magnet beamline at the BMIT facility at the CLS [3-5]. The beamline was used in "White Beam" mode.

The Laue system is shown schematically in Figure B- 2. The crystal was located in the bend magnet imaging hutch approximately 20.5m from the source. The distance from the crystal to the detector is 3m and 23.5 m from the source. A (3, 1, 1) type reflection from a commercially available silicon (5, 1, 1) wafer was used for the Laue monochromator which was tuned to 33.169keV at the absorption K-edge of iodine. The Bragg angle for the lattice planes was 6.55 degrees.

A combination monochromator was prepared for this experiment, one side of this monochromator was the bent Laue for Spectral KES and the other side a flat Laue for beam motion measurements. The Spectral KES is an imaging method using for imaging contrast elements such as iodine in biomedical systems [6, 7]. The simultaneous measurement of imaging data and beam

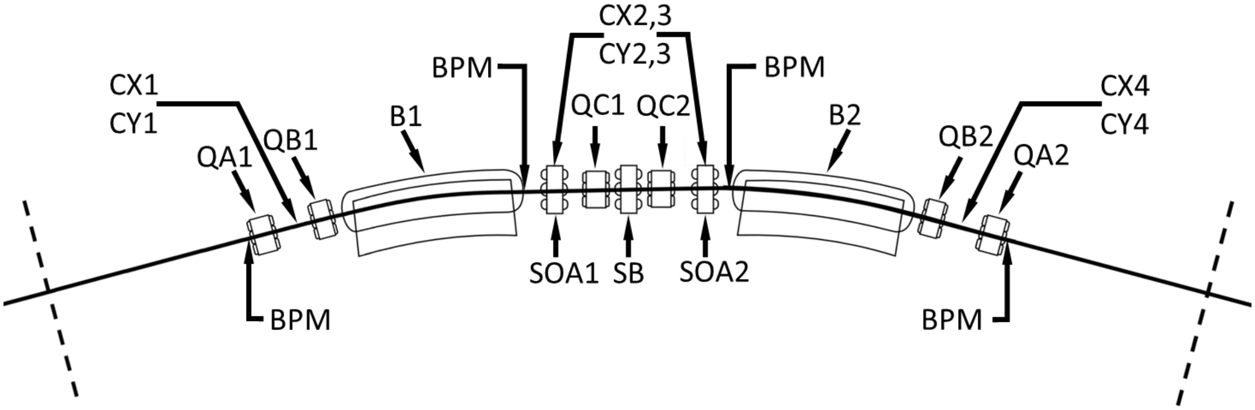

Figure B- 3 Schematic layout of a cell (one of 12) in the CLS storage ring. CX and CY are orbit correctors, QA, QB, QC are quadrupole magnets, BPMs are electron beam position monitors, SOA, SB are sextupole magnets and Bs are dipole magnets. The dashed lines show the extent of a cell.

motion data is for using beam motion information to correct the resulting images. The data correction part will be discussed elsewhere. All the beams were intercepted by the same detector (bent Laue for Spectral and flat Laue with and without a contrast filter for beam motion). The advantage of this approach was that the imaging and the correction data were acquired simultaneously. The detector was a Hamamatsu flat-panel with 100 micron pixel size and 30 frames per second acquisition speed.

Each measurement contained data in the form of tiff images in sets of 400. For each measurement a set of 10 flats (images of the beam with no object in the way) and 10 darks (images of detector response with no beam) were also collected to normalize data.

A combination of 0.05 mm copper and 2.5 mm aluminum were used to filter the white beam and prevent thermal loading on the monochromator.

The incident photon beam at the monochromator was around 6 mm high and 178 mm wide.Two types of data were collected, one during normal operations of the machine and the other one in special request shifts were a known frequency beam motion was introduced in the ring.

While the data was being collected with the ps-BPM system at the beamline, different currents with different frequencies were used in an orbit corrector at location CY1 in Figure B- 3 to introduce a perturbation in the electron ring. This corrector is the first vertical orbit corrector in cell 3.

The measurements where made using the first bend magnet in cell 5 (B1). The center of the bend magnet beam is 5 degrees into the 15 degree bend provided by the magnet.

These perturbations had frequencies of 5Hz and 10Hz each with currents of 0, 0.12, 0.24 and 0.6A in the orbit corrector.

Both the orbit correction and the transverse feedback system were on during all the measurements and the ring was operating at 250mA current in decay mode.

B.4 RESULTS AND DISCUSSION

Measurements where made while the beam was sinusoidally modulated using an orbit corrector while the motion was monitored with the ps-BPM system at the BMIT beamline.

From the design specification the vertical kick for a corrector is given by

$$kick[\mu rad] \approx 7.637 \times I[A], \tag{B. 1}$$

where I[A] is the current driving the corrector. So, for a 0.12A excitation the kick is 0.916 microradians. The effect of a vertical kick was simulated with DIMAD [8] at the nominal tunes of the CLS lattice. The closed orbit was calculated with a kick of 1.018 microradians at the position of the orbit corrector 1 in cell 3. With this kick the closed orbit at the position of the BMIT bend mag-net (B1 in cell 5) beamline is: y = -6.83 micron and y’ = -1.089 microradians for the peak values. For larger kicks the position and angle are assumed to scale with the input current.

The temporal measured and predicted beam motions are shown in Figure B- 4. The measured values are y (red) and y+Dy' (violet). The derived angular motion Dy' is shown in blue. Modulation currents of 0, 0.12, 0.24 and 0.6A where used as shown for frequencies of 5Hz (Figure B- 4a) and 10Hz (Figure B- 4b). The expected amplitude of Dy' appears as black dashed lines. The expected values of y were too small to mark on the plots.

The measured and expected peak to peak values for the beam motions in Figure B- 4 are given in Table B- 1.

There is a good agreement between the predicted and measured values for all currents and frequencies.

Table B- 1 Measured and predicted values (in parentheses) of beam motion for corrector currents and frequencies given in the text and Figure B- 4.

f (Hz)	**I (A)**	y**(μm)**	Dy'**(μm)**	y'**(μrad)**	$y + Dy'$**(μm)**
0	0.0	7.7 ± 2	13.6 ± 2	0.5 ± 0.1	16.2 ± 3
5	0.12	15.6 ± 2 (13.7)	42.5 ± 3 (51.7)	1.6 ± 0.1 (2.2)	57.9 ± 3
10	0.12	9.9 ± 4 (13.7)	51.1 ± 3 (51.7)	2.0 ± 0.1 (2.2)	51.4 ± 3
5	0.24	27.3 ± 2 (27.4)	92.7 ± 3 (103.4)	3.6 ± 0.1 (4.4)	119.9 ± 4
10	0.24	21.3 ± 3 (27.4)	82.9 ± 3 (103.4)	3.2 ± 0.1 (4.4)	104.0 ± 4
5	0.60	43.7 ± 8 (68.3)	255.8 ± 9 (256.2)	9.8 ± 0.3 (10.9)	299.5 ± 5
10	0.60	28.3 ± 6 (68.3)	227.2 ± 7 (256.2)	8.7 ± 0.3 (10.9)	255.1 ± 10

With the similar setup described at the original paper [1] measurements were done while the electron beam size and angular distribution were adjusted using skew quads. The vertical source size and angular size were measured by the system and compared against measurements of the source size made by a pinhole camera at the X-ray Synchrotron Radiation (XSR) diagnostic beamline [9]. The ps-BPM measurements correlate well with beam size measurements at the XSR beamline. Figure B- 5 shows the measured direct beam width (Figure B- 5b) and the edge width (Figure B- 5a) from which we can estimate the vertical emittance of the source. The parabolic-type behavior of the measurements indicate that other terms contribute in quadrature to the widths. The results correlate with each other but require further interpretation.

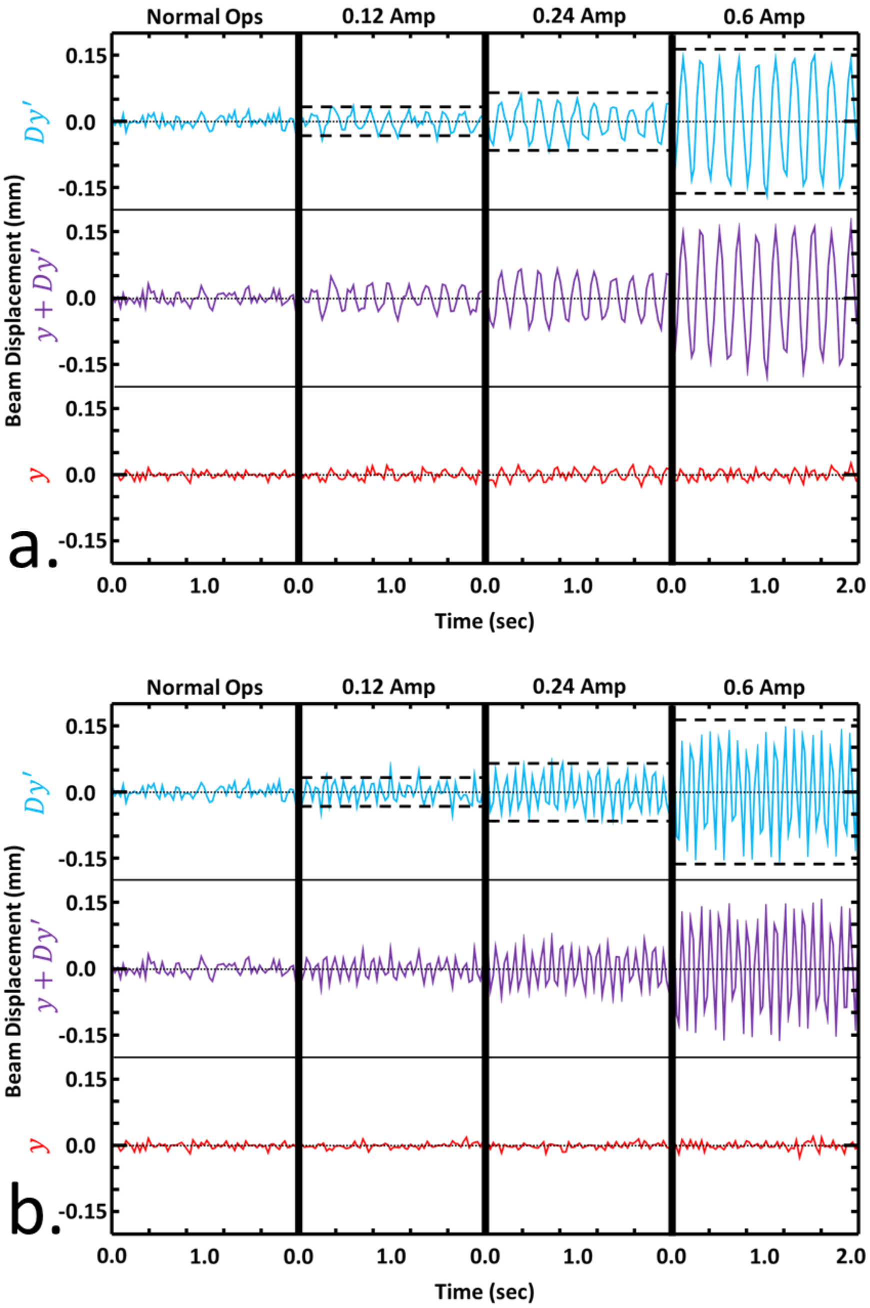

Figure B- 4 ps-BPM measurements as the orbit corrector current is increased (0, 0.12, 0.24, 0.6A) for 5Hz (Figure a) and 10Hz (Figure b). The dashed black lines indicate the expected peak to peak amplitude of the electron beam motion.

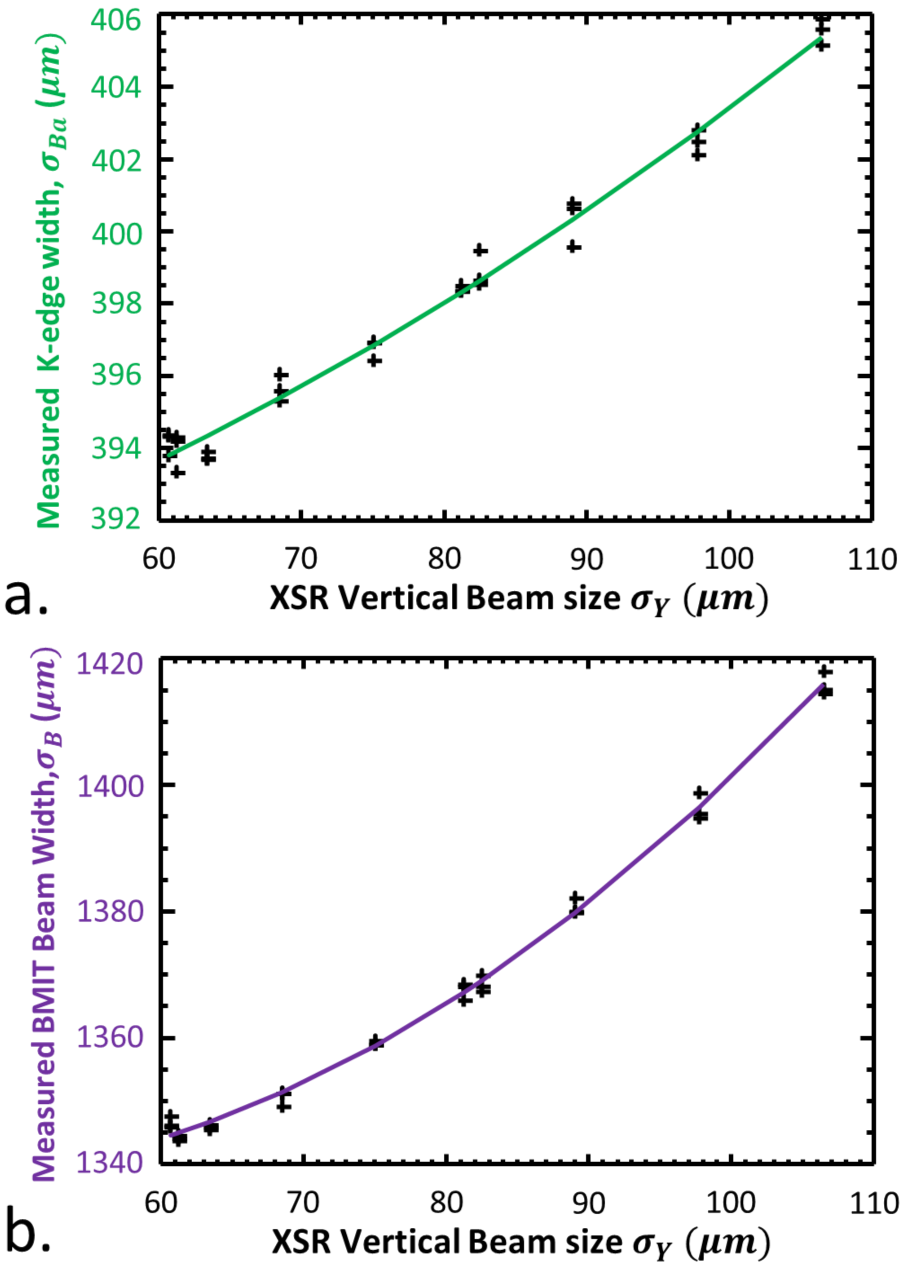

Figure B- 5 Measured widths of the beam (Figure b) and the K-edge (Figure a) as skew quads are used to increase the vertical beam size. The horizontal axis is the vertical size as measured by XSR beamline

B.5 CONCLUSIONS

A newly developed phase space beam position monitor has been used to measure induced beam motions in a synchrotron source. There is good agreement between the expected motion and those measured by this monitor. The results presented here are the first aspect of using this monitor to correct experimental data for an imaging method, Spectral KES, which is susceptible to the vertical position and angle motion. The fact that these measurements accurately show this motion, gives a good indication that we will be successful in correcting this data.

Also measurements have been made of the widths of the beam and K-edge as skew quads were used to in-crease the vertical size and angular size of the electron beam. Both size and angular size were shown to in-crease indication that the vertical emittance can be measured. At this point the sensitivity of these measurements is being assessed as well as other contributors to the measured widths.

Both the data correction and measurements of emittance will be the topics of future papers.

B.6 ACKNOWLEDGEMENT

The authors acknowledge the financial support of Canadian Institutes of Health Research (CIHR) Training Grant - Training in Health Research Using Synchrotron Techniques, Saskatchewan Health Research Foundation Team Grant, Natural Sciences and Engineering Research Council of Canada (NSERC) Discovery Grant, the University of Saskatchewan, and Canada Research Chair Program. Research described in this paper was performed at the Canadian Light Source, which is fund-ed by the Canada Foundation for Innovation, NSERC, the National Research Council Canada, CIHR, the Government of Saskatchewan, Western Economic Diversification Canada, and the University of Saskatchewan.

B.7 REFERENCES

1. N. Samadi, B. Bassey, M. Martinson, G. Belev, L. Dallin, M. de Jong, et al., "A phase-space beam position monitor for synchrotron radiation," J Synchrotron Radiat, vol. 22, pp. 946-55, Jul 2015.
2. J. A. Golovchenko, R. A. Levesque, and P. L. Cowan, "X-ray monochromator system for use with synchrotron radiation sources," Review of Scientific Instruments, vol. 52, pp. 509-16, 04/ 1981.
3. T. W. Wysokinski, D. Chapman, G. Adams, M. Renier, P. Suortti, and W. Thomlinson, "Beamlines of the biomedical imaging and therapy facility at the Canadian light source - Part I," Nuclear Instruments & Methods in Physics Research Section a-Accelerators Spectrometers Detectors and Associated Equipment, vol. 582, pp. 73-76, Nov 11 2007.
4. T. W. Wysokinski, D. Chapman, G. Adams, M. Renier, P. Suortti, and W. Thomlinson, "Beamlines of the Biomedical Imaging and Therapy Facility at the Canadian Light Source - Part 2.," 11th International Conference on Synchrotron Radiation Instrumentation (Sri 2012), vol. 425, 2013.
5. T. W. Wysokinski, D. Chapman, G. Adams, M. Renier, P. Suortti, and W. Thomlinson, "Beamlines of the biomedical imaging and therapy facility at the Canadian light source - part 3," Nuclear Instruments & Methods in Physics Research Section a-Accelerators Spectrometers Detectors and Associated Equipment, vol. 775, pp. 1-4, Mar 1 2015.
6. Y. Zhu, N. Samadi, M. Martinson, B. Bassey, Z. Wei, G. Belev, et al., "Spectral K-edge subtraction imaging," Physics in Medicine and Biology, vol. 59, pp. 2485-2503, 2014.
7. N. Samadi, M. Martinson, B. Bassey, A. Gomez, G. Belev, and D. Chapman, "An energy dispersive bent Laue monochromator for K-edge subtraction imaging," AIP Conference Proceedings, vol. 1741, p. 040004, 2016.
8. R. V. Servranckx, K. L. Brown, L. Schachinger and D. Douglas, "Users Guide to the Program DIMAD," Stanford Linear Accelarator Laboratory, Stanford Linear Accelarator Laboratory, 1990.
9. J. C. Bergstrom and J. M. Vogt, "The optical diagnostic beamline at the Canadian Light Source," Nuclear Instruments and Methods in Physics Research Section A: Accelerators, Spectrometers, Detectors and Associated Equipment, vol. 562, pp. 495-512, 6/15/ 2006.